FEDERAL UNIVERSITY OF SÃO CARLOS
CENTER FOR EXACT SCIENCES AND TECHNOLOGY
GRADUATE PROGRAM IN MATERIALS SCIENCE AND ENGINEERING

STRUCTURAL RELAXATION OF GLASS AND ITS INFLUENCE ON OTHER DYNAMIC PROCESSES

Ricardo Felipe Lancelotti

São Carlos-SP
2025

FEDERAL UNIVERSITY OF SÃO CARLOS
CENTER FOR EXACT SCIENCES AND TECHNOLOGY
GRADUATE PROGRAM IN MATERIALS SCIENCE AND ENGINEERING

STRUCTURAL RELAXATION OF GLASS AND ITS INFLUENCE ON OTHER DYNAMIC PROCESSES

Ricardo Felipe Lancelotti

Thesis submitted to the Graduate Program in Materials Science and Engineering in partial fulfillment of the requirements for the degree of Ph.D. in Materials Science and Engineering

Supervisor: Prof. Dr. Edgar Dutra Zanotto
Funding agencies: CAPES/PROEX (04/01/2021 to 11/30/2021, grant 88887.612841/2021-00), FAPESP (12/01/2021 to 11/30/2022 and 12/01/2023 to 01/31/2025, grant 2021/03374-5), and FAPESP/BEPE (12/01/2022 to 11/30/2023, grant 2022/07679-8)

São Carlos-SP
2025

DEDICATION

To my family, for their support that enabled me to fully dedicate myself to the demanding work involved in this thesis.

VITAE

Master degree in Materials Science and Engineering from the Federal University of São Carlos (2021), Bachelor degree in Materials Engineering from the Federal University of São Calos (2018).

UNIVERSIDADE FEDERAL DE SÃO CARLOS

Centro de Ciências Exatas e de Tecnologia
Programa de Pós-Graduação em Ciência e Engenharia de Materiais

Folha de Aprovação

Defesa de Tese de Doutorado do candidato Ricardo Felipe Lancelotti, realizada em 30/01/2025.

Comissão Julgadora:

Prof. Dr. Edgar Dutra Zanotto (UFSCar)

Profa. Dra. Ana Candida Martins Rodrigues (UFSCar)

Prof. Dr. Eduardo Bellini Ferreira (USP)

Prof. Dr. John C. Mauro (PennState)

Prof. Dr. Sabyasachi Sen (UCDavis)

O Relatório de Defesa assinado pelos membros da Comissão Julgadora encontra-se arquivado junto ao Programa de Pós-Graduação em Ciência e Engenharia de Materiais.

ACKNOWLEDGMENTS

Completing this thesis represents the end of my four-year Ph.D. period. I would like to express my gratitude to all the people and institutions that supported and guided me along the way.

First, I am deeply thankful to my supervisor, Prof. Edgar D. Zanotto, for his unwavering support and guidance since my undergraduate years. His mentorship has been very important, combining his extensive scientific knowledge with his international influence, which has opened many doors for me.

At my home institution, the Federal University of São Carlos, I wish to thank Prof. Ana Candida Rodrigues, Prof. Oscar Peitl, lab technician José Rodrigues, and secretary Laurie Rodrigues, as well as my colleagues Marcelo Kurtovic, Rafael Rosante, William Sato, Vinicius Zallocco, Alberth Costa, João Campos, and Isabela Lavagnini, along with all the other members of our research group, whose support has been essential throughout this period.

I am profoundly grateful to Prof. Sabyasachi Sen from the University of California at Davis, for welcoming me during my year-long internship in 2022–2023. His insights and expertise greatly enriched the quality of this thesis. I would also like to thank my colleagues at UC Davis, Jacob Lovi, Ido Chuang, and Mario Morales, as well as my housemates Andrea Garman, Isabella Duarte, Wiliam Oliveira, and Marcos Junqueira, who made my time in California truly unforgettable.

I am also thankful to my collaborators and hosts at the University of Munich, Luiz Pereira, Prof. Kai Hess and Prof. Donald Dingwell, for the opportunity to work in their lab during my short visits in 2022 and 2024, where I was able to utilize the powerful Flash-DSC technique.

A huge thank you to my Mom & Dad, Silvana F. G. Lancelotti and Carlos R. Lancelotti (Minão), as well as to my sister Carla T. Lancelotti and my brother-in-law Daniel Rienzo, who have always been there for me, supporting and believing in me. *Muito obrigado, amo vocês!*

A special thanks to Jessica C. Silva, who during this time became Jessica C. S. Lancelotti, my beloved wife. Getting married during my Ph.D. has made this period even more meaningful. Words cannot express how grateful I am for the constant support received. I love you so much!

Lastly, I would like to thank the Coordenação de Aperfeiçoamento de Pessoal de Nível Superior (CAPES) for the research grant 88887.612841/2021-00 (PROEX) and the São Paulo Research Foundation (FAPESP) for research grants 2013/07793-6 (CEPID), 2021/03374-5, and 2022/07679-8 (BEPE), which made this research possible. This study was financed in part by the Coordenação de Aperfeiçoamento de Pessoal de Nível Superior—Brasil (CAPES)—Finance Code 001.

ABSTRACT

The physics of the glassy state is governed by two fundamental phenomena. The first is the liquid-to-glass transition, characterized by a kinetic constraint that restricts molecular rearrangement at a low enough temperature (or high enough viscosity), leading to the formation of a glass (unstable). The second is the spontaneous structural relaxation of glass back towards the metastable supercooled liquid state, wherein this constraint is overcome. This thesis investigates the mechanisms and effects of the spontaneous structural relaxation on the atomic configurations and macroscopic properties of single- and mixed-modifier oxide glasses. The research is organized into chapters that focus on: (i) the interplay between cooling rates and structural relaxation, studied using the flash-DSC technique; (ii) the kinetics of structural relaxation induced by physical aging, analyzed through changes in refractive index and ionic conductivity at various temperatures; (iii) the response of enthalpy recovery and refractive index of glasses to up- and down-jumps in fictive temperature, evaluated through the Kohlrausch–Williams–Watts function and the Tool–Narayanaswamy–Moynihan model; (iv) the network connectivity speciation and atomic rearrangements during structural relaxation in silicate glasses, analyzed using Raman and Nuclear Magnetic Resonance spectroscopy; and (v) the impact of slow structural changes due to the phenomenon of structural relaxation on ionic diffusion, which significantly influences the faster process of ionic conductivity in different glasses. The findings highlight the importance of understanding and controlling structural relaxation to design new glasses with optimized properties and ensure the long-term stability of these properties.

Keywords: Glass; Structural Relaxation; Aging; Fictive Temperature; Enthalpy Recovery; Density; Ionic Conductivity; Refractive Index; NMR; Raman.

RESUMO

RELAXAÇÃO ESTRUTURAL DE VIDROS E SUA INFLUÊNCIA EM OUTROS PROCESSOS DINÂMICOS

A física do estado vítreo é governada por dois fenômenos fundamentais. O primeiro é a transição de líquido para vidro, caracterizada por uma restrição cinética que limita o rearranjo molecular a uma temperatura suficientemente baixa (ou viscosidade suficientemente alta), levando a formação de um vidro (instável). O segundo é a relaxação estrutural espontânea do vidro de volta para o estado metastável de líquido super resfriado, onde essa restrição é superada. Esta tese investiga os mecanismos e os efeitos da relaxação estrutural espontânea nas configurações atômicas e nas propriedades macroscópicas de vidros óxidos com modificadores simples e mistos. A pesquisa está organizada em capítulos que abordam: (i) a relação entre taxas de resfriamento e relaxação estrutural, estudada utilizando a técnica de flash-DSC; (ii) a cinética de relaxação estrutural induzida por envelhecimento físico, analisada por meio de mudanças no índice de refração e na condutividade iônica em diferentes temperaturas; (iii) a resposta da entalpia e do índice de refração de vidros ao aumento e diminuição da temperatura fictícia, avaliada por meio da função de Kohlrausch–Williams–Watts e do modelo de Tool–Narayanaswamy–Moynihan; (iv) a conectividade da rede estrutural e os rearranjos atômicos durante a relaxação estrutural em vidros silicatos, analisados por espectroscopia Raman e de Ressonância Magnética Nuclear; e (v) o impacto das mudanças lentas na estrutura devido ao fenômeno de relaxação estrutural na difusão iônica, que influencia significativamente o processo rápido de condutividade iônica em diferentes vidros. Os resultados destacam a importância de entender e controlar a relaxação estrutural para projetar novos vidros com propriedades otimizadas e garantir a estabilidade dessas propriedades a longo prazo.

Palavras-chave: Vidro; Relaxação Estrutural; Envelhecimento; Temperatura Fictícia; Entalpia; Densidade; Condutividade Iônica; Índice de Refração; RMN; Raman.

PUBLICATIONS

Peer-reviewed papers

- T.R. Cunha, D. V. Sampaio, R.B. Pena, B.J.A. Moulton, **R.F. Lancelotti**, F.G. Alabarse, A.D. Rodrigues, P.S. Pizani, Thermal expansion and compressibility of alamosite ($PbSiO_3$) determined by in-situ synchrotron X-ray diffraction, Ceram. Int. 48 (2022) 34350–34354. https://doi.org/10.1016/j.ceramint.2022.08.012.

- **R.F. Lancelotti**, A.C.M. Rodrigues, E.D. Zanotto, Structural relaxation dynamics of a silicate glass probed by refractive index and ionic conductivity, J. Am. Ceram. Soc. 106 (2023) 5814–5821. https://doi.org/10.1111/jace.19285.

- **R.F. Lancelotti**, T.R. da Cunha, M.A.C. Kurtovic, P.S. Pizani, S. Sen, E.D. Zanotto, Physical aging of lithium disilicate glass, J. Non. Cryst. Solids. 622 (2023) 122661. https://doi.org/10.1016/j.jnoncrysol.2023.122661.

- L. Pereira, S. Schuller, F.B. Wadsworth, J. Vasseur, **R.F. Lancelotti**, K. Hess, S. Gossé, D.B. Dingwell, Rheology of a sodium-molybdenum borosilicate melt undergoing phase separation, Int. J. Appl. Glas. Sci. 15 (2024) 127–38. https://doi.org/10.1111/ijag.16650.

- **R.F. Lancelotti**, E.D. Zanotto, S. Sen, Kinetics of physical aging of a silicate glass following temperature up- and down-jumps, J. Chem. Phys. 160 (2024) 34504. https://doi.org/10.1063/5.0185538.

- S. Sen, **R.F. Lancelotti**, I. Hung, Z. Gan, Characterization of the Pb coordination environment and its connectivity in lead silicate glasses: Results from 2D ^{207}Pb NMR Spectroscopy, J. Phys. Chem. B. 128 (2024) 2811–2820. https://doi.org/10.1021/acs.jpcb.3c08307.

- **R.F. Lancelotti**, E.D. Zanotto, S. Sen, Atomistic origin of structural relaxation in lead metasilicate and lithium disilicate glasses, J. Am. Ceram. Soc. 107 (2024) 7131–41. https://doi.org/10.1111/jace.19918.

- **R.F. Lancelotti**, L. Pereira, K. Hess, D.B. Dingwell, E.D. Zanotto, Flash-DSC provides valuable insights into glass relaxation and crystallization, J. Non. Cryst. Solids. 646 (2024) 123242. https://doi.org/10.1016/j.jnoncrysol.2024.123242.

- **R.F. Lancelotti**, S. Chuang, E.D. Zanotto, S. Sen, Effect of physical aging on ionic conductivity of network oxide glasses. Acta Mater. 285 (2024). 120658. https://doi.org/10.1016/j.actamat.2024.120658.

Conference presentations

- **R.F. Lancelotti**, E.D. Zanotto. Relaxação estrutural abaixo da temperatura fictiva via mudanças na temperatura de transição vítrea. In: 65º – 66º Congresso Brasileiro de Cerâmica. Poster presentation. Águas de Lindóia, Brazil. June, 2022.

- **R.F. Lancelotti**, A.C.M. Rodrigues, E.D. Zanotto. Structural relaxation dynamics of a silicate glass via changes in three properties. In: 26th International Congress on Glass. Oral presentation. Berlin, Germany. July, 2022.

- **R.F. Lancelotti**, A.C.M. Rodrigues, E.D. Zanotto. Unveiling structural relaxation in a silicate glass via different properties. In: 26th International Congress on Glass. Poster presentation. Berlin, Germany. July, 2022.

- **R.F. Lancelotti**, E.D. Zanotto. Structural relaxation dynamics via glass transition temperature. In: XX B-MRS Meeting, symposium M: XIII Brazilian Symposium on Glass and Related Materials. Oral presentation. Foz do Iguaçu, Brazil. September, 2022.

- **R.F. Lancelotti**, E.D. Zanotto, S. Sen. Stretched and compressed exponential relaxation in glass. In: 2023 Glass & Optical Materials Division Annual Meeting. Oral presentation. New Orleans, United States. June, 2023.

- **R.F. Lancelotti**, S. Sen, E.D. Zanotto. Structural rearrangements during relaxation of lithium disilicate glass. In: Materials Science & Technology 23. Poster presentation. Columbus, United States. October, 2023.

- **R.F. Lancelotti**, S. Sen, E.D. Zanotto. Effect of physical aging on the structure of lithium disilicate and lead metasilicate glasses. In: 2024 Glass & Optical Materials Division Annual Meeting. Oral presentation. Las Vegas, United States. May, 2024.
- **R.F. Lancelotti**, M. Kurtovick, O. Peitl, E.D. Zanotto. Structural relaxation of a medieval cathedral glass. In: Materials Science & Technology 24. Oral presentation. Pittsburgh, United States. October, 2024.
- **R.F. Lancelotti**, E.D. Zanotto, S. Sen. Atomistic origin of structural relaxation in lead metasilicate and lithium disilicate glasses. In: Materials Science & Technology 24. Oral presentation. Pittsburgh, United States. October, 2024.

TABLE OF CONTENTS

FOLHA DE APROVAÇÃO i
ACKNOWLEDGMENTS iii
ABSTRACT v
RESUMO vi
PUBLICATIONS vii
TABLE OF CONTENTS xi
CHAPTER 1 – INTRODUCTION 1
CHAPTER 2 – BACKGROUND 3
2.1 Glass 3
2.2 Glass transition and fictive temperatures 6
2.3 Structural relaxation 10
2.4 Strong and fragile liquids 15
CHAPTER 3 – GLASS RELAXATION USING FLASH-DSC 17
3.1 Introduction 17
3.2 Materials and Methods 18
3.3 Results and Discussion 19
3.4 Conclusions 29
CHAPTER 4 – RELAXATION KINETICS VIA REFRACTIVE INDEX AND IONIC CONDUCTIVITY 31
4.1 Introduction 31
4.2 Materials and Methods 32
4.3 Results and Discussion 34
4.4 Conclusions 40
CHAPTER 5 – STRUCTURAL RELAXATION FOLLOWING TEMPERATURE UP- AND DOWN-JUMPS 41
5.1 Introduction 41
5.2 Materials and Methods 42
5.3 Results and Discussion 46
5.4 Conclusions 54
CHAPTER 6 – ATOMISTIC ORIGIN OF STRUCTURAL RELAXATION 55

6.1 Introduction 55
6.2 Materials and Methods 56
6.3 Results and Discussion 59
6.4 Conclusions 71
CHAPTER 7 – EFFECT OF STRUCTURAL RELAXATION ON IONIC CONDUCTIVITY 73
7.1 Introduction 73
7.2 Materials and Methods 74
7.3 Results and Discussion 76
7.4 Conclusions 87
CHAPTER 8 – GENERAL CONCLUSIONS 89
SUGGESTIONS FOR FUTURE WORKS 91
REFERENCES 93

CHAPTER 1 – INTRODUCTION

The glass transition is one of the most interesting and still unsolved problems in condensed matter physics [1]. When a liquid is cooled below its melting point and crystallization is kinetically prevented, it remains as a metastable supercooled liquid (SCL). As this SCL is further cooled towards its glass transition region, its atomic structure freezes on laboratory timescales at the so-called fictive temperature (T_f) and vitrifies [2]. At temperatures $T < T_f$, the resultant glassy state is not in thermodynamic equilibrium [3]. Consequently, glasses spontaneously undergo structural relaxation, a gradual adjustment of their atomic arrangement, in response to changes in the external thermodynamic variables like temperature or pressure [4]. This relaxation, typically referred to as primary α-relaxation, involves cooperative atomic or molecular motion that enables the unstable system to reduce its free energy and reach a metastable equilibrium with the newly imposed conditions [5].

Understanding structural relaxation and its dependence on thermal history is key to designing new glass products or optimizing the long-term performance of functional glasses. This is because temporal changes in the atomic structure impact all their physical properties [6–8]. Various experimental techniques have been employed to measure the kinetics of the relaxation process during physical aging experiments by measuring the time-dependent response of property variations [9–13].

In this thesis, Chapter 2 introduces the fundamental concepts of the glassy state and structural relaxation. Subsequent chapters address specific issues related to the relaxation of glasses:

- Chapter 3 aims to study the thermal behaviors of $Li_2Si_2O_5$ and $PbSiO_3$ glasses using varied cooling and heating rates to demonstrate the applicability of flash-DSC in underscoring the relaxation phenomenon. By combining conventional and flash DSC methods, interesting dynamics related to the glass transition were observed, revealing significant differences in the glass transition temperature values and their correlation with experimental time and the Angell definition of the glass transition.
- Chapter 4 investigates the dependence of the relaxation kinetics on refractive index and ionic conductivity in $Li_2Si_2O_5$ glass. Isothermal treatments involving temperature down-jumps were performed and the Kohlrausch–Williams–Watts

(KWW) function accurately described the experimental data. The non-exponentiality parameter was found to be a function of measurement temperature, fictive temperature, and the analyzed property. The relaxation kinetics measured for the same glass under identical conditions indeed depend on the analyzed property.

- Chapter 5 applies and tests the validity of the KWW function and the Tool–Narayanaswamy–Moynihan (TNM) model by monitoring changes in enthalpy and refractive index following up- and down-jumps for $Li_2Si_2O_5$ glass. The KWW described the data for temperature up- and down-jumps separately, revealing distinct exponential behaviors, while the TNM was able to describe both up- and down-jump datasets simultaneously, although its ability to accurately describe the data decreased with larger temperature jumps.
- Chapter 6 investigates structural rearrangements during relaxation in $Li_2Si_2O_5$ and $PbSiO_3$ glasses using Raman and Nuclear Magnetic Resonance (NMR) spectroscopy. Following significant increase in density, enthalpy, and refractive index after temperature down-jump, the analysis of Raman and NMR spectra revealed that aging-induced structural relaxation involves disproportionation of Q-species and their spatial clustering.
- Chapter 7 elucidates the impact of structural relaxation on the migration enthalpy and entropy of ionic conduction in $Li_2Si_2O_5$, $Na_{0.75}Mg_{0.125}PO_3$, and $LiPO_3$ glasses. Physical aging experiments using temperature down-jump protocols revealed distinct behaviors in the migration enthalpy and entropy of ionic conduction between single-alkali and mixed-modifier glasses. The results provide valuable insights into how the ionic conductivity of glass can be effectively controlled by simply adjusting its fictive temperature.

Overall, this thesis aims to achieve a deep understanding of structural relaxation and its effects on physical properties of oxide glasses. This has been done by experimentally studying the impact of α-relaxation during aging through changes in different properties such as glass transition temperature, density, refractive index, enthalpy, and ionic conductivity, as well as structural changes using Raman and nuclear magnetic resonance spectroscopy.

CHAPTER 2 – BACKGROUND

2.1 Glass

Throughout history, glass has been a material of immense significance, influencing the course of human civilization from ancient artifacts to modern technological innovations. Despite significant progress in recent years, the fundamental question of what exactly defines glass can still generate confusion. So, what is glass?

Traditionally, the word glass has been associated with inorganic products of fusion that have been cooled to a rigid condition without crystallizing [14]. There are numerous definitions of glass in the literature, with most agreeing that glasses are non-crystalline materials that exhibit a glass transition. For instance, Zarzycki defines glass as "a noncrystalline solid that presents the phenomenon of glass transition" [15]. Shelby describes glass as "an amorphous solid completely lacking in long range, periodic atomic structure, and exhibiting a region of glass transformation behavior" [16]. Gutzow and Schmelzer use the plural form, stating that "glasses are thermodynamically non-equilibrium kinetically stabilized amorphous solids, in which the molecular disorder and the thermodynamic properties corresponding to the state of the respective under-cooled melt at a temperature T^* are frozen-in. Hereby T^* differs from the actual temperature T" [17]. Varshneya and Mauro define glass as "a solid having a non-crystalline structure, which continuously converts to a liquid upon heating" [18].

These definitions diverge in some aspects, and more recently, Zanotto and Mauro emphasized that the structure of glass is similar to that of its parent SCL, and that glasses appear solid on a typical human time scale but will flow at any temperature under the action of gravity. Thus, their definition is "Glass is a nonequilibrium, noncrystalline condensed state of matter that exhibits a glass transition. The structure of glasses is similar to that of their parent supercooled liquids (SCL), and they spontaneously relax toward the SCL state. Their ultimate fate is to solidify, i.e., crystallize" [14].

It is important to note that glasses are not limited to inorganic oxide materials. There are also organic, polymeric, and metallic glasses as well as different soft materials systems, such as colloidal, foams, molecular, and elementary glasses [19–22], among others [23–25]. Therefore, glass is not a specific material but rather any material that exists in a particular physical state of matter, the vitreous or glassy state [14,17,18,26].

Several structural models have been developed to describe the arrangement of atoms within a glassy network and their spatial relationships. Most inorganic glasses are composed of a mixture of different oxides, including network formers, intermediates, and modifiers, resulting in a highly diverse structures within these materials.

In 1932, Zachariasen [27] published a landmark paper attempting to explain glass formation, with a focus on oxide glasses. He began by acknowledging that, at that time, there was practically no understanding of the atomic arrangement in glass. Based on X-ray diffraction (XRD) experiments, he provided the first evidence that the glass network is neither periodic nor symmetrical like that of crystals but is instead characterized by an infinitely large unit cell. This led to the concept of glass as a three-dimensional random network, forming the basis for the Continuous Random Network (CRN) model, illustrated in **Figure 2.1**(a) in two dimensions for a hypothetical oxide compound A_2O_3, where A represents network-forming atoms, which is compared to the crystalline structure of the same chemical composition in **Figure 2.1**(b). These triangular polyhedra, as in B_2O_3 glass, or tetrahedral polyhedra, as in SiO_2 glass, are usually corner-linked through bridging oxygens (BO) and form a three-dimensional extended connected network. Therefore, glasses display short-range atomic order but lack long-range order. The short-range structure is well-defined within the first coordination sphere and nearest neighbor. In contrast, the structural disorder in a glass network at long-range order is partly due to the statistical distribution of angles between the coordination polyhedra compared to those in crystals [28].

The structure of glass network is altered by the introduction of network modifier cations, such as alkali, alkaline earth, and transition metals. These additions lead to the formation of a new structure, resulting in distinct chemical and physical properties. The presence of modifier ions disrupts the connectivity of the oxide network, leading to the formation of non-bridging oxygens (NBO) that are linked to a network-forming atom and a network-modifying cation. The Modified Random Network (MRN) model describes how the interaction between network-forming and network-modifying components results in modifier ions forming channels within a depolymerized network structure [29], as shown in **Figure 2.1**(c), also in two-dimensions for the case of triangular polyhedra, in a glass of approximate composition $M_2O_3(A_2O_3)_2$, where M are network-modifying cations and A are network-forming atoms.

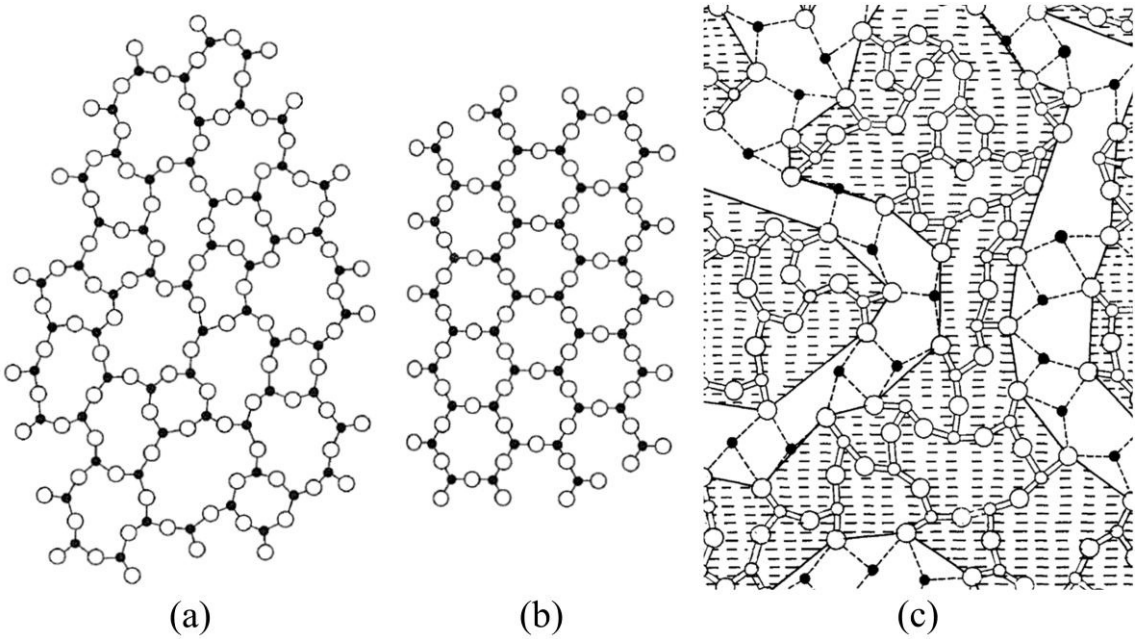

Figure 2.1: Two-dimensional schematic representations of structural models for a hypothetical oxide compound A_2O_3, where A represents network-forming atoms. (a) Continuous random network model, with filled circles representing network-forming atoms and open circles representing BOs. (b) Comparison with the ordered crystalline structure of the same composition. (c) Modified random network model for a composition $M_2O_3(A_2O_3)_2$, where small open circles represent network-forming atoms A, large open circles represent oxygen atoms O, and filled circles represent network-modifying cations M, illustrating the formation of NBOs and channels within the depolymerized structure. Figure (a) is reprinted from Zachariasen, 1932 [27], (b) from Kingery, 1976 [30], and (c) from Greaves, 1985 [29].

Engelhardt et al. [31] introduced a notation that is used in this thesis to describe network connectivity in silicate glasses, based on different types of tetrahedra denoted as Q^n species. In this notation, Q represents a quaternary group with four bonds, and $0 \leq n \leq 4$ indicates the number of BO bonds per tetrahedron. In the CRN model, the structure of a pure silica glass ideally consists of tetrahedra that are fully corner-connected to another tetrahedra, referred to as Q^4 species. However, in the MRN model, the structure of multicomponent silicate glass leads to network depolymerization, resulting in a distribution of Q^n species. Some glasses, such as lead metasilicate, can exhibit all five Q^n species [32].

2.2 Glass transition and fictive temperatures

The liquid state is thermodynamically stable at temperatures above the liquidus temperature (T_L), whereas the crystalline phase is a stable state at lower temperatures. If crystallization can be kinetically avoided during cooling, the melt becomes a metastable SCL, with no discontinuity in the enthalpy–temperature (*H*–*T*) diagram, **Figure 2.2**. As the SCL is cooled further, at a certain region, its viscosity becomes so high that its atomic structure freezes at laboratory timescales, and a glass is obtained. Hence, the glassy state is thermodynamically unstable, with the atoms considered temporarily frozen in a disordered arrangement. The transformation region between the SCL and the glass is not a transition in the thermodynamic sense, but a kinetic process [33] that cannot be characterized by a single temperature. However, only a single temperature is normally used as an indication of the onset of the transformation region where the glass begins to behave as a viscoelastic material upon heating [16]. This single temperature is called the laboratory glass transition temperature (T_g), which is experimentally determined by changes observed in calorimetry or thermal expansion measurements during the heating of a glass sample.

The glass transition refers to a temperature range where the average structural relaxation time of the material, $\langle\tau\rangle$, is of the same order of magnitude as the observation time or time of the experiment, t_{obs} [14,34]. In this region, on the heating path, a glass undergoes a transition from an unstable glassy state to a metastable fluid state (i.e., SCL) [35]. T_g depends on the composition, thermal history, pressure, and heating rate of the glass. In the glass transition range, the Deborah number (De) [36] Eq. (2.1) is approximately unity. Considering a fixed observation time, the physical properties reach equilibrium very fast for $De \ll 1$, whereas they change slowly for $De \gg 1$ [37].

$$De = \frac{\langle\tau\rangle}{t_{obs}}. \tag{2.1}$$

For practical purposes, Angell [38] proposed that T_g is the temperature at which the shear viscosity (η) of the SCL is equal to 10^{12} Pa s. This definition holds for T_g onset measured via differential scanning calorimetry (DSC) at matching cooling/heating rates ($q_{c,h}$) of 10 K/min, that is, the intersection of the extrapolated glass line and the tangent of the inflection point during the glass transition. At this rate, the t_{obs} required

for a 1 K change is 6 s, and the average shear relaxation time at T_g is within the range of 30–200 s, as calculated by the Maxwell relation (Eq. (2.2)) using the shear viscosity of 10^{12} Pa s and the infinite frequency shear modulus (G_∞), which typically varies from 5 to 35 GPa for oxide glass compositions [39],

$$\langle\tau\rangle(T) = \frac{\eta(T)}{G_\infty}. \tag{2.2}$$

Although vitrification occurs over a finite temperature range, the fictive temperature, T_f, proposed by Tool [2,10,40], is a parameter that allows the expression of the difference in thermal history between glasses obtained at different cooling rates. Frequently, T_f is referred to as the limiting fictive temperature to indicate the limit temperature at which the structure of a SCL is frozen-in during the cooling path [41]. Thus, if the glass and SCL lines are extrapolated in **Figure 2.2**, they will intersect at T_f, where both the glass and SCL would have the same structure.

A glass produced at a relatively fast cooling rate will have a higher fictive temperature ($T_{f,1}$), which allows less time for the atoms to rearrange and usually results in a less compact atomic structure than its isochemical relative obtained using a lower cooling rate ($T_{f,2}$) [42].

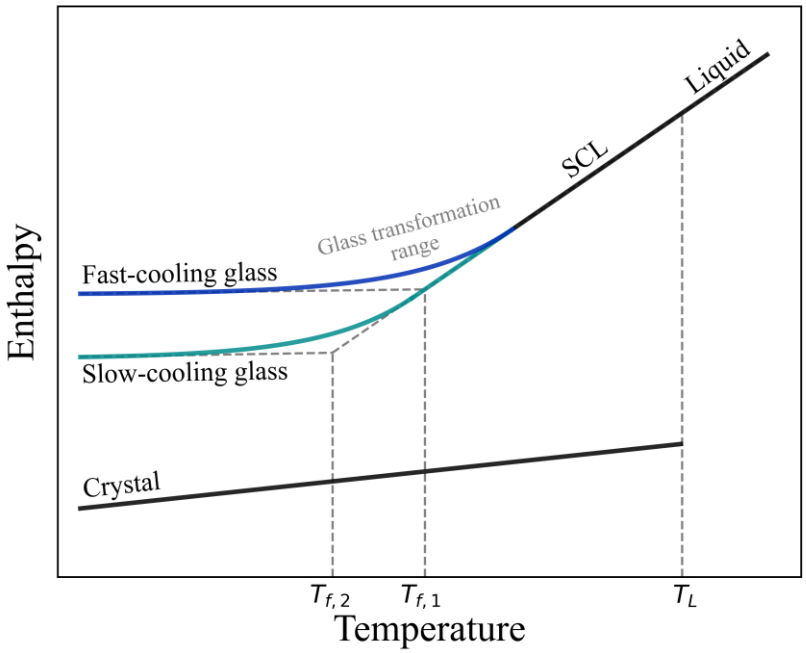

Figure 2.2: Schematic diagram of the effect of temperature on the enthalpy of a glass-forming substance showing the liquid, SCL, glassy and crystalline states.

It is worth noting that interesting phenomena can occur when attempting to measure the T_g of glasses cooled at different rates (q_c). To illustrate this, **Figure 2.3** shows a schematic *H*–*T* diagram of a glass-forming substance along with the corresponding isobaric heat capacity, $C_p \equiv (dH/dT)_p$, similar to literature results for liquids cooled at different rates [43–47]. Despite the glasses having different T_f, the measured T_g can be very similar. When a liquid is fast cooled at $-q_1$ with a high $T_{f,1}$ and then heated at q_2 ($|q_2| \ll |q_1|$), the material in the glassy state begins to relax before reaching the SCL state, resulting in a $T_{g,1}$ that could be very close to $T_{g,2}$ from an isochemical liquid cooled and heated at $|q_2|$ with a lower $T_{f,2}$.

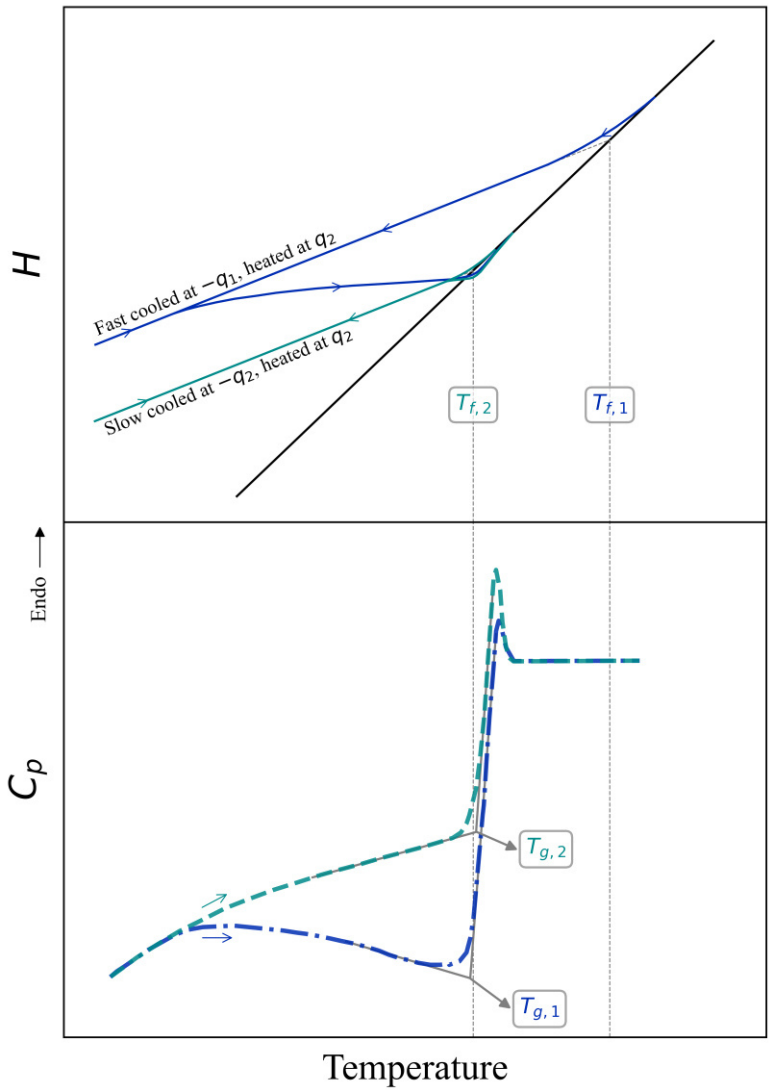

Figure 2.3: Schematic diagram of enthalpy and isobaric heat capacity as functions of temperature for a glass-forming substance cooled at rates $-q_1$ and $-q_2$, and heated a rate q_2. Note that $T_{f,1} > T_{f,2}$, in contrast to $T_{g,1} \sim T_{g,2}$.

The observed peak in the C_p curves on heating represents an overshoot, related to the enthalpy recovery towards the SCL state at the glass transition region, which becomes more pronounced as the cooling rate is lowered [47]. Because of the (temporarily) frozen nature of the glass structure, the atomic mobility is reduced below the glass transition. When a glass is subjected to a slower cooling rate, structural mobility causes an increase in density. Consequently, when the sample is heated, a higher amount of energy is required for the glass transition, resulting in a higher endothermic peak.

The concept of a single T_f has been shown to be inadequate [5,48,49]. An alternative approach is to consider a distribution of fictive temperatures. However, the physical significance of this distribution and its practical applicability remain unclear [49]. On the other hand, the concept of the limiting fictive temperature is helpful to characterize the structural state of the glass. The fictive temperature can be defined not only in the final glassy state but also throughout different states. At temperatures above the glass transition range, the fictive temperature matches the physical temperature, indicating that the system is in metastable equilibrium. As the system is cooled through the glass transition range, the fictive temperature becomes frozen at a certain value, which is higher than the physical temperature, signifying that the system is out of equilibrium.

Moynihan et al. [41] developed a method for measuring the limiting fictive temperature, T_f. However, their calorimetric single-heating method cannot be applied to rapidly quenched glasses at standard DSC heating rates, as these glasses undergo structural relaxation during heating, resulting in a broad exothermic enthalpy relaxation before the glass transition interval, as observed in the case of fibers [50]. To address this limitation, Yue et al. [44] introduced a method based on two calorimetric upscans. Although their method is effective, they did not provide a graphical representation for its application when $T_f < T_{SCL}$, where T_{SCL} is the onset temperature of the SCL. Consequently, several authors have incorrectly applied this method under this condition [45,51]. Guo et al. [51] then proposed a unified area-matching approach, which can be applied by obtaining two consecutive heat capacity curves (C_{p1} and C_{p2}) at the same upscan rate. The fictive temperature of the first upscan, $T_{f,1}$, can be determined as follows:

$$\int_{T_{f,2}}^{T_{f,1}} (C_{p,l} - C_{p,g}) dT = \int_{T_a}^{T_b} (C_{p2} - C_{p1}) dT, \quad (2.3)$$

where $C_{p,l}$ is the heat capacity of the SCL, $C_{p,g}$ is the heat capacity of the glass, $T_{f,2}$ is approximately the T_g onset during the second scan (matching the cooling and reheating rates) [52], and T_a and T_b are temperatures well below and above T_g, respectively.

2.3 Structural relaxation

Structural relaxation occurs in glasses because they are thermodynamically out of equilibrium and involves a spontaneous rearrangement of the atomic structure over time that allows the system to lower its free energy [7,53]. The structural relaxation phenomenon can be studied through physical aging experiments, which typically involve monitoring subtle changes in macroscopic properties such as volume [22,54,55], density [56–58], enthalpy [59–61], refractive index [62–64], viscosity [65–67], resistivity or conductivity [54,68,69], and hardness [70–72], over time, during or after changes in temperature below the fictive temperature (at $T < T_f$).

As the glass evolves during physical aging experiments from its initial to its final equilibrium state, the rate at which the properties evolve depends on the actual temperature, pressure, chemical composition, and thermobaric history of the glass [73]. These experiments are challenging when performed well below T_f because of the long times involved, which can exceed the typical laboratory timescales [74]. Far below T_f (a range that depends on the glass composition), experiments may be continued for months and even years [7]. Therefore, most experimental studies focus on temperature intervals that are not far below the glass transition region.

Relaxation times vary from seconds in the glass transition region to geological times at room temperature [75,76], and are crucial for comprehending the properties of glasses and improving manufacturing processes that impact products of glass industry such as optical fibers, flat panel display substrates, and thermally and chemically strengthened glass articles [77–80].

Physical aging of glass is mainly studied by observing changes in properties related to the primary (α) structural relaxation during a temperature jump at ambient pressure. The α-relaxation involves the cooperative atomic/molecular motion [81]. A

secondary (β) structural relaxation, which is much faster, occurs on the order of 10^{-5} seconds and is observed at lower temperatures, involving the non-collective motion of small groups of atoms [82,83]. β-relaxation is sometimes divided into two types, slow and fast, since there are different sizes of local motion, as shown for metallic glasses [84,85], in which very fast relaxation is initiated and centered in some local sites. In contrast, slow relaxation spreads out to the surroundings, including to less-mobile atoms. All these relaxation types become indistinguishable at high temperatures since all structural rearrangements are accessible in a short period.

Besides the possibility of changing T_f during glass preparation by employing different cooling rates, as shown in the previous section (**Figure 2.2**), it is also possible to change T_f within the glassy state during heat treatments at temperatures below or above the initial T_f, as indicated by the red arrow in **Figure 2.4**, where the initial property p_0 changes to its metastable equilibrium value, p_∞.

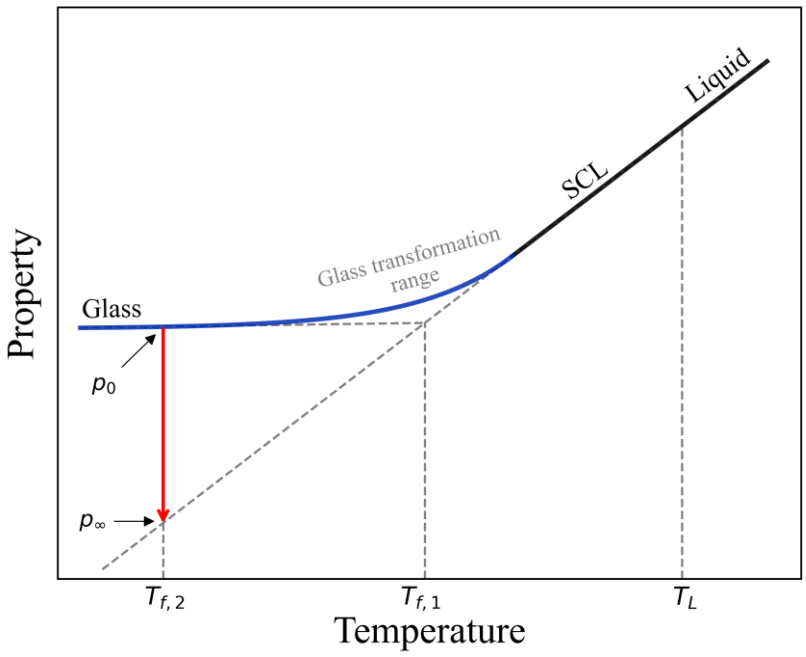

Figure 2.4: Schematic Property–Temperature diagram, where the red arrow indicates isothermal physical aging, illustrating the gradual transition from $T_{f,1}$ to $T_{f,2}$, with properties changing from p_0 to p_∞. The property axis is representative, with properties such as volume, ionic conductivity, and enthalpy typically decreasing as temperature decreases. On the other hand, properties such as refractive index, density, viscosity, and electrical resistivity generally increase as temperature decreases.

A down-jump in T_f is the predominant method used to investigate α-relaxation, where the glass can be readily aged below T_g. An up-jump experiment involves the initial step of lowering the initial T_f long enough at the interest temperature before initiating the actual up-jump procedure [6,12].

When a glass undergoes isothermal aging following a temperature jump, any physical property (p) evolves with aging time (t) from its initial value (p_0) to its final value (p_∞), defining a normalized relaxation function as:

$$\phi(t) = \frac{p(t) - p_\infty}{p_0 - p_\infty}. \tag{2.4}$$

According to this definition, the relaxation parameter, $\phi(t)$, is unity for $t = 0$, i.e., at the onset of the temperature jump, and zero for a fully relaxed system when equilibrium is reached at the new temperature at sufficiently long times. Several models have been proposed to describe the primary or α-relaxation process in glass-forming systems. For instance, the empirical Kohlrausch equation [86,87], which is also known as the Kohlrausch–Williams–Watts (KWW) function [88], describes the temporal decay of $\phi(t)$ as:

$$\phi(t) = \exp\left[-\left(\frac{t}{\tau_K}\right)^\beta\right], \tag{2.5}$$

where τ_K is the characteristic relaxation time of the system and β is the non-exponentiality parameter. This function describes a stretched exponential relaxation kinetics for $0 < \beta < 1$ and a purely exponential relaxation for $\beta = 1$ [89,90]. These parameters are related to $\langle\tau\rangle$ via the expression:

$$\langle\tau\rangle = \int_0^\infty \phi(t)dt = \tau_K \Gamma\left(\frac{1}{\beta} + 1\right), \tag{2.6}$$

where Γ is the gamma function.

A combination of Eqs. (2.4) and (2.5) yields a KWW-type function that describes the temporal evolution of any property $p(t)$ as:

$$p(t) = p_\infty + (p_0 - p_\infty)\exp\left[-\left(\frac{t}{\tau_K}\right)^\beta\right]. \tag{2.7}$$

Phillips [21,91] proposed a relaxation model based on diffusion to traps to obtain limiting values of β of either 3/5 or 3/7 near T_f. However, studies indicate that β decreases with decreasing the temperature rather than remaining constant [8,64,92]. Lower β values imply a wider distribution of relaxation times, i.e., structural units with different relaxation times. **Figure 2.5** illustrates the behavior of ϕ as a function of time for $\beta \leq 1$. The curves intersect at the same point when $t = \tau_k$ (1 s in this example). Thus, $\phi = \exp(-1) \approx 0.368$, i.e., the characteristic relaxation time is defined for a 63.2% relaxed material.

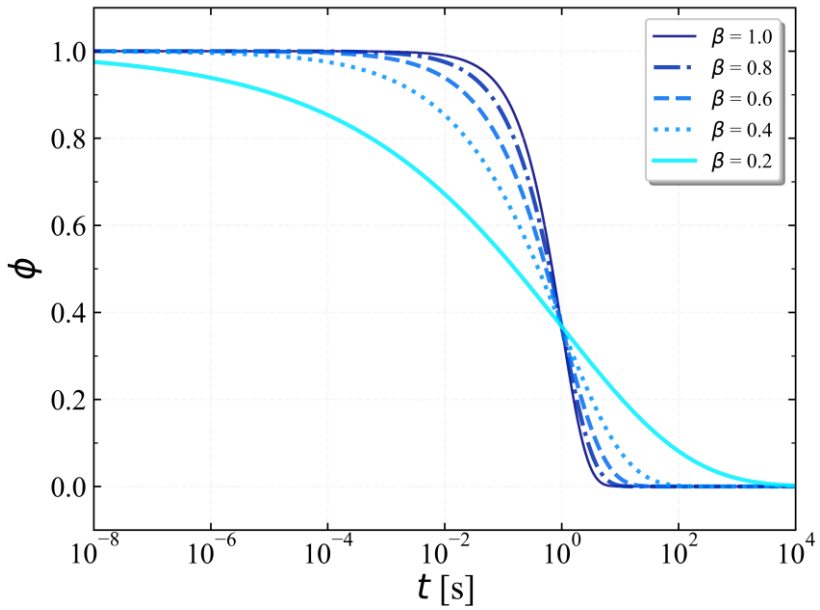

Figure 2.5: Relaxation parameter as a function of time, calculated via Eq. (2.5) for $\tau_k = 1$ s and different β values. It is important to note the extremely wide time scale spanning several orders of magnitude.

Concerning the origin of the stretched exponential relaxation, two potential explanations can be presented [82]. The relaxation process can be stretched as a result of the spatial dynamical heterogeneities arising from fluctuations in density and composition within glass forming systems. This heterogeneous dynamics is characterized by locally exponential relaxation with a spatiotemporally varying time constant, τ. Consequently, the relaxation of the ensemble can be expressed as a sum of exponentials, each with a different τ, giving rise to a global non-exponential decay [28,82]. This scenario is formally equivalent to a distribution of relaxation times, $f(\tau)$, which relates to the relaxation function as:

$$\phi(t) = \int_0^\infty f(\tau) e^{-t/\tau} d\tau. \quad (2.8)$$

The distribution function $f(\tau)$ is subject to the constraint: $\int_0^\infty f(\tau) d\tau = 1$. This equation can be closely approximated by a Prony series,

$$\phi(t) = \sum_{i=1}^{N} w_i \exp\left(-\frac{t}{\tau_i}\right), \quad (2.9)$$

where the weighting factors w_i satisfy $\sum_{i=1}^{N} w_i = 1$. In this case, the non-exponentiality parameter β is a measure of the width of this distribution $f(\tau)$, with lower values of β corresponding to a wider distribution and vice versa.

In contrast, in a homogeneous dynamical scenario, the stretching of the relaxation originates from cooperativity in a hierarchical sequence of events. Here, the relaxation is intrinsically non-exponential, with a lower value of β signifying stronger cooperativity [1].

The relaxation rate in the glassy state depends not only on the actual temperature but also on the T_f of the glass. It results in the non-linear effect of the intrinsic structural changes during physical aging that has been described traditionally in the glass literature by the Tool–Narayanaswamy–Moynihan (TNM) model [5,10,93]. In this model, t/τ is replaced by the reduced time (ξ), resulting in the restoration of linearity [5,94],

$$\xi(t) = \int_0^t \frac{dt'}{\tau(t')}. \quad (2.10)$$

To distinguish an up-jump experiment from a down-jump experiment, one can employ a relaxation function δ instead of using the normalized relaxation function of Eq. (2.4). This function represents a fractional departure of an instantaneous property value $p(t)$ from the equilibrium value p_∞:

$$\delta(t) = \frac{p(t) - p_\infty}{p_\infty}. \quad (2.11)$$

It is easy to see that $\phi(t) = \frac{\delta(t)}{\delta_0}$, where δ_0 is the initial value of the relaxation function ($\delta_0 = \frac{p_0 - p_\infty}{p_\infty}$). Thus, a glass equilibrated at T_0 and then exposed to a temperature T will change its T_f over time according to [22]:

$$\frac{\delta(t)}{\delta_0} = \frac{T_f(t) - T}{T_0 - T}. \tag{2.12}$$

Moreover, the relaxation function introducing the reduced time is given by:

$$\frac{\delta(t)}{\delta_0} = \exp\left[-\left(\int_0^t \frac{dt'}{\tau(t')}\right)^\beta\right]. \tag{2.13}$$

Combining Eqs. (2.12) and (2.13), in the TNM model, T_f can be expressed as:

$$T_f(t) = T + (T_0 - T)\exp\left[-\left(\int_0^t \frac{dt'}{\tau(t')}\right)^\beta\right], \tag{2.14}$$

where the relaxation time, τ, incorporates a non-linearity parameter $0 \leq x \leq 1$ to consider the contributions of both T and T_f [93]:

$$\tau = A \exp\left(\frac{x\Delta h^*}{RT} + \frac{(1-x)\Delta h^*}{RT_f}\right), \tag{2.15}$$

where A is the pre-exponential constant, R is the universal gas constant, and Δh^* is the activation energy for the relaxation process.

2.4 Strong and fragile liquids

When selecting the aging temperature to study α-relaxation, it is important to consider the fragility index (m) of the composition, as the kinetics of relaxation of glasses with different m would be different in response to the same magnitude of jump in temperature below T_f [95]. This difference arises because the shear viscosity, η, or equivalently, the shear relaxation time ($\langle\tau\rangle$, Eq. (2.2)), of SCLs exhibit a temperature-dependent activation energy that deviates from the Arrhenius [96]. This deviation was classified by Angell [97] into strong and fragile types, which are highly dependent on the composition. The fragility can be quantified by the fragility index m, measuring the slope of log (η) vs. T_g/T at T_g:

$$m \equiv \left. \frac{d(\log(\eta))}{d\left(T_g/T\right)} \right|_{T=T_g} \tag{2.16}$$

which reflects the apparent activation energy at T_g. Strong liquids, characterized by small values of m (e.g. ~ 20–40), closely follow Arrhenius behavior with a weakly temperature-dependent activation energy for viscous flow. In contrast, fragile liquids exhibit more pronounced super-Arrhenius behavior, with strongly temperature dependent activation energy and relatively high values of m (> 40). Therefore, at $T < T_g$, the timescale of α-relaxation increases more rapidly for fragile compositions compared to strong ones. Consequently, the experimental time required for a fragile composition to reach metastable equilibrium is longer than that of a strong composition at the same T_g/T. Furthermore, the change in heat capacity during the glass transition is significantly more pronounced in fragile liquids compared to strong liquids [18].

Ideally, m is determined through viscosity or structural relaxation time measurements in the SCL state near the glass transition. However, it has been found that m can be calculated using T_g and the activation energy for enthalpy relaxation (E) [98–100] as follows:

$$m = \frac{E}{RT_g \ln(10)}, \tag{2.17}$$

The E value can be determined by analyzing the dependence of the calorimetric T_f on the reheating rate, q, which is equal to the previous cooling rate. This relationship in given by:

$$\frac{d\ln(q)}{d\left(1/T_f\right)} = -\frac{E}{R}. \tag{2.18}$$

Thus, it is easy to see that m may be directly obtained from the slope of log ($1/q$) vs. T_g/T_f.

CHAPTER 3 – GLASS RELAXATION USING FLASH-DSC

3.1 Introduction

Conventional differential scanning calorimeters are widely used to study thermal responses in glasses, such as crystallization, relaxation, and glass transition. However, their cooling (q_c) and heating (q_h) rates are limited, typically ranging from 0.01 to 2 K/s.

Wang et al. [98] and Chen et al. [99] conducted DSC experiments by varying the cooling rates followed by heating at a fixed rate of 20 K/min. They analyzed the heating heat capacity curves by comparing the overshoot peaks obtained with different cooling rates. These authors found that lower cooling rates resulted in greater overshoots, which they subsequently analyzed in terms of the heat capacity difference between the standard curve (where heating and cooling rates were the same) and the others. This phenomenon is related to the enthalpy release from the nonstandard sample that was further used to determine the fragility index.

These types of experiments have recently become possible using very high quench and heating rates, extending the conventional range by approximately four orders of magnitude, through the development of a chip-based fast scanning calorimeter, Flash-DSC (FDSC) [101]. The FDSC can perform measurements using ultra-fast standard (UFS 1) or ultra-fast heating (UFH 1) chip sensors. These sensors consist of a ceramic substrate with electrical connections and a membrane with two active zones: one for the sample and the other for the reference. The development of high-temperature chip sensors enables measurements of micrometric samples over a wide temperature range (178–1,273 K), employing high heating (up to 5×10^4 K/s) and cooling (4×10^4 K/s) rates [46,102]. This capability allows for the exploration of a wider range of experimental times. Therefore, the FDSC instrument complements conventional DSC by allowing the study of thermal transitions such as crystallization and glass transition under high heating and cooling rates.

In this chapter, the objective is to study the interplay between heating and cooling rates, structural relaxation, and the glass transition temperature by employing the flash-DSC technique with lithium disilicate ($Li_2Si_2O_5$) and lead metasilicate ($PbSiO_3$) glasses, which have distinct fragility indices and glass-forming ability.

3.2 Materials and Methods

The melt-quenching method was employed to produce approximately 50 g of $33.3Li_2O{\cdot}66.7SiO_2$ ($Li_2Si_2O_5$) and $50.0PbO{\cdot}50.0SiO_2$ ($PbSiO_3$) glasses (in mol%). They were synthesized from stoichiometric mixtures of reagent-grade Li_2CO_3 (99.0%, Alfa Aesar), Pb_3O_4 (99.0%, Sigma-Aldrich), and SiO_2 (99.9%, Vitrovita). The chemicals were thoroughly mixed at 1,400 rpm for 5 min in a high-speed mixer (Flacktek speed mixer DAC 1,200-500) and the resulting mixture/batch was placed in platinum crucible. For $Li_2Si_2O_5$ glass synthesis, the batch was decarbonated at 1,073 K for 2 h in an electric furnace and then melted at 1,673 K for 1 h before being poured onto a steel plate and splat-quenched by pressing with a steel block. For $PbSiO_3$ glass synthesis, the batch was melted at 1,323 K for 10 min in an electric furnace to minimize PbO volatilization, poured onto a steel plate, and pressed with a steel block.

A conventional DSC (Mettler Toledo DSC1) was employed to determine the $T_{g,\text{onset}}$ of the $Li_2Si_2O_5$ sample using ~10 mg in a hermetically sealed Al pan, heated at a rate of 10 K/min under a N_2 atmosphere.

A Flash-DSC (Mettler-Toledo Flash-DSC 2+) equipped with a high-temperature, ultra-fast heating UFH 1 chip sensor (**Figure 3.1**) and purged with Ar was employed to determine $T_{g,\text{onset}}$ and T_f of microscopic $Li_2Si_2O_5$ and $PbSiO_3$ glass samples at various rates. The FDSC temperature was calibrated using the melting point of aluminum. The ultra-fast UFH 1 sensor, with an active zone diameter of approximately 100 μm, was utilized to create different fictive temperatures.

For this purpose, larger samples of each glass composition were broken into smaller pieces. Using the microscope integrated with the FDSC, a microscopic piece of each glass was selected using a hair in a pen and placed on the sensor, which was wetted with a thin film of silicone oil that evaporates and decomposes during the first heating. Thus, the glass samples obtained with unknown cooling rates and T_f were rejuvenated above the glass transition (i.e., until the SCL state was reached) to erase their thermal histories and were subsequently cooled at different rates (q_c) of 10,000, 5,000, and 1,000 K/s, followed by reheating at the same rate ($q_{c,h}$). Additionally, the $T_{g,\text{onset}}$ was determined during reheating at a rate of 5,000 K/s after being cooled at rates of 10,000, 5,000, 1,000, 500, 100, and 50 K/s.

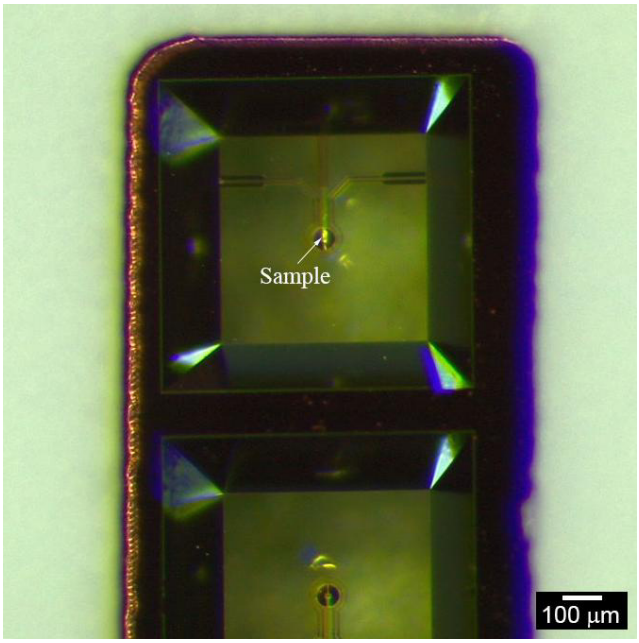

Figure 3.1: UFH 1 chip sensor of the Mettler-Toledo Flash-DSC 2+, consisting of a ceramic substrate with electrical connections and two membranes: one for the sample and one as the reference site. A microscopic glass sample of $Li_2Si_2O_5$ is positioned on the dark circle of the upper membrane.

3.3 Results and Discussion

Figure 3.2 shows the $T_{g,\text{onset}}$ of the $Li_2Si_2O_5$ glass using significantly different heating rates. In **Figure 3.2**(a), a value of (727 ± 2) K was determined using a conventional DSC at a heating rate of 10 K/min, which agrees with literature values [103–105]. The dashed line represents the temperature at which $\langle\tau\rangle$ is 6 s, which is the t_{obs} required for a 1 K change at 10 K/min. This was calculated by the Maxwell relation (Eq. (2.2)) with the average of G_∞ interval (20 GPa) and the Mauro–Yue–Ellison–Gupta–Allan (MYEGA) model [106] for $\eta(T)$, which is given by the following equation:

$$\log\left(\eta(T)\right) = \log\left(\eta_\infty\right) + \left[12 - \log\left(\eta_\infty\right)\right]\frac{T_{g,12}}{T}\exp\left[\left(\frac{m}{12 - \log\left(\eta_\infty\right)} - 1\right)\left(\frac{T_{g,12}}{T} - 1\right)\right], \quad (3.1)$$

where η_∞ is the extrapolated infinite temperature viscosity, $T_{g,12}$ is the temperature where the shear viscosity is 10^{12} Pa s, and m is the fragility index. The fitting parameters employed are presented in **Table 3.1**. A much higher $T_{g,\text{onset}}$ of (849 ± 2) K for the same $Li_2Si_2O_5$ glass is shown in **Figure 3.2**(b), measured using a flash-DSC technique at a

heating rate of 10,000 K/s, which requires only 10^{-4} s to change 1 K. In this scenario, the average relaxation time of the material is 7.0×10^{-4} s. This demonstrates that for both the conventional heating rate and the high heating rate used, the T_g obtained corresponds to a temperature where the average structural relaxation time of the material is of the same order of magnitude as the experimental time, confirming the definition of T_g [34], even for high heating rates. Additionally, because of the significantly higher heating rate of 10,000 K/s, the viscosity at T_g in this case is not 10^{12} Pa s as proposed by Angell [38], but approximately 1.4×10^{7} Pa s.

It should be mentioned that Schawe and Hess observed a thermal lag in the glass transition peak temperature ($T_{g,\text{peak}}$) in a silicate glass for heating rates higher than 5,000 K/s [46]. On the other hand, Al-Mukadam et al. [102] reported a lower thermal lag in the $T_{g,\text{onset}}$ compared to $T_{g,\text{peak}}$. Moreover, the extent of thermal lag varies depending on the sample mass utilized. Here, a microscopic sample (**Figure 3.1**) was used in the FDSC measurement, and therefore a thermal lag of ~10 K could be considered at a heating rate of 10,000 K/s, which decreases the $T_{g,\text{onset}}$ to approximately 840 K.

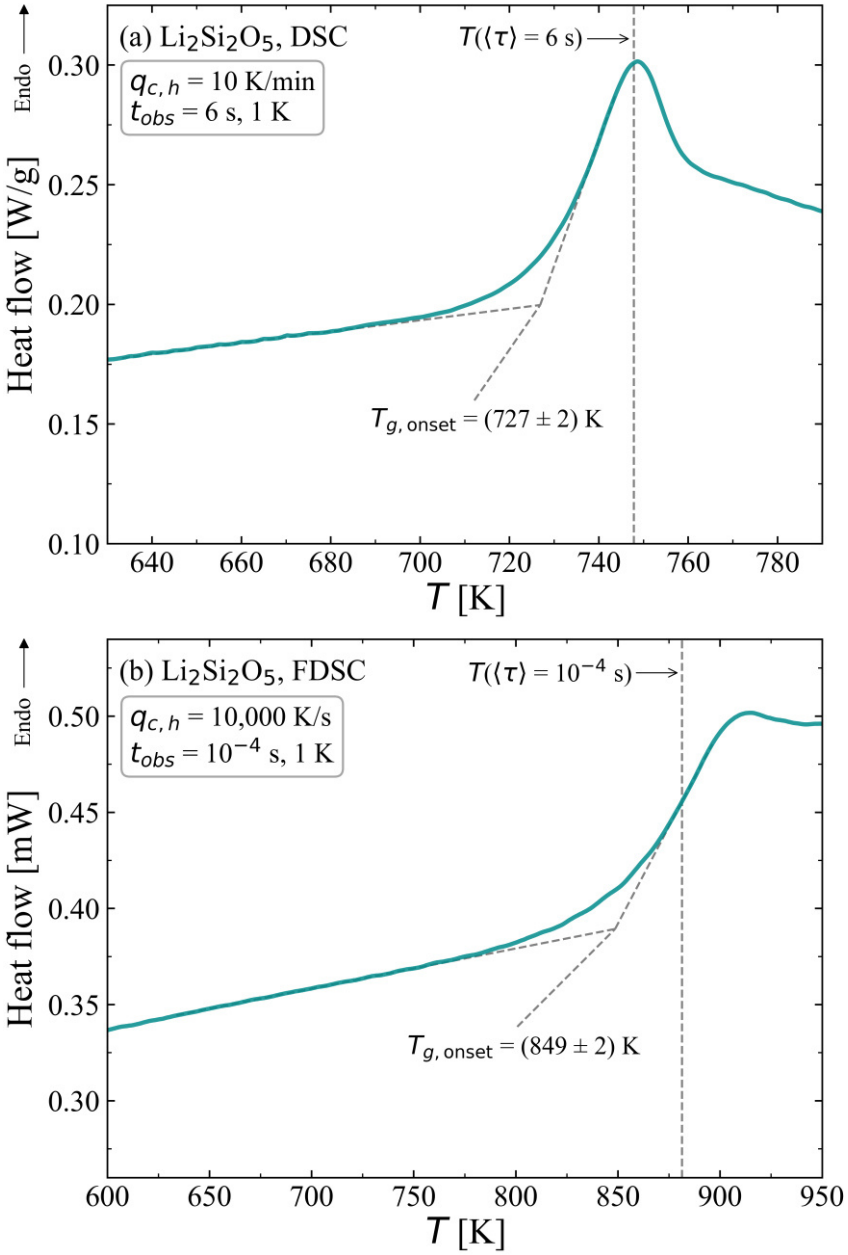

Figure 3.2: Determination of $T_{g,\text{onset}}$ of a $Li_2Si_2O_5$ glass using (a) conventional DSC measurement at a heating rate of 10 K/min (0.17 K/s) and (b) FDSC measurement at a heating rate of 10,000 K/s. Vertical dashed lines show the temperature at which $\langle\tau\rangle$ is 6 s and 10^{-4} s, respectively.

Figure 3.3 shows the fictive temperatures determined from the flash-DSC curves by matching the heating rates to the cooling rates at which the glasses were produced. Employing this strategy, the onset glass transition temperatures are very close to the fictive temperatures [46,52]. Specifically, a downscan at q_c was utilized to establish a T_f, which was then followed by an upscan at the same rate q_h. In this case, $|q_c| = |q_h| =$

$q_{c,h}$; consequently, $T_{g,\text{onset}}$ coincides with T_f in the unified area-matching approach. The overlapping of curves observed during multiple heating and cooling cycles at the same rate provides evidence that T_f is indeed equal to $T_{g,\text{onset}}$ when applying the unified area-matching method.

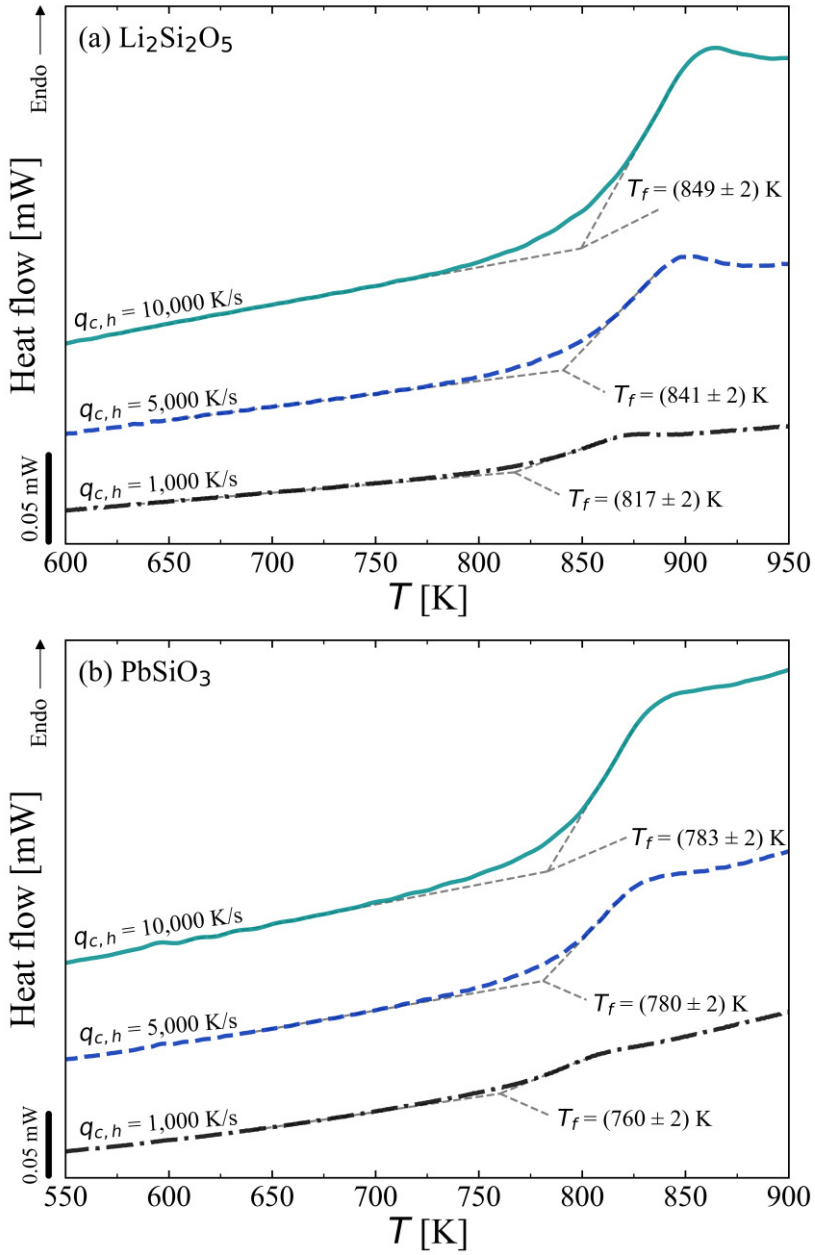

Figure 3.3: Determination of T_f using FDSC scans obtained at $q_{c,h}$ = 1,000 K/s, 5,000 K/s, and 10,000 K/s for (a) $Li_2Si_2O_5$ and (b) $PbSiO_3$ glasses.

The shift factor is an important parameter because it enables the retrieval of viscosity, η(T), without the need for conventional viscosity measurements. This approach is quite useful in gathering data in a region where the SCL rapidly crystallizes or

undergoes liquid phase separation. **Figure 3.4** shows that the curve of log (η) vs. 1/T is shifted from the curve of log ($1/q_{c,h}$) vs. $1/T_f$ by a parallel shift factor (K_{onset}), Eq. (3.2) [62,107]. The MYEGA equation was adjusted to literature data of shear viscosity [64,102,108–112], and the resulting fitting parameters for both glasses are displayed in **Table 3.1**.

$$K_{\mathrm{onset}} = \log\left(q_{c,h}\right) + \log\left(\eta\left(T_f\right)\right). \tag{3.2}$$

Note that the shift factor varies for differently defined glass transition temperatures, such as $T_{g,\mathrm{onset}}$ and $T_{g,\mathrm{peak}}$ [62,107]. The individual shift factors for $T_{g,\mathrm{onset}}$ (K_{onset}) obtained at 1,000 K/s, where the thermal lag does not influence the derived data [46] were 11.1 ± 0.1 for $Li_2Si_2O_5$ and 10.1 ± 0.2 for $PbSiO_3$, clearly indicating that the (logarithmic) shift factor is dependent on the chemical composition of the glass, which is in agreement with the observation reported by Gottsmann et al. [107] and contrasts with assumptions made elsewhere [102,113,114].

Table 3.1: Fitting parameters for the MYEGA equation, Eq. (3.1).

MYEGA equation	log (η_∞ [Pa s])	$T_{g,12}$ [K]	m
$Li_2Si_2O_5$	−1.41 ± 0.07	731.0 ± 0.3	42.2 ± 0.4
$PbSiO_3$	−1.26 ± 0.04	682.8 ± 0.2	59.8 ± 0.4

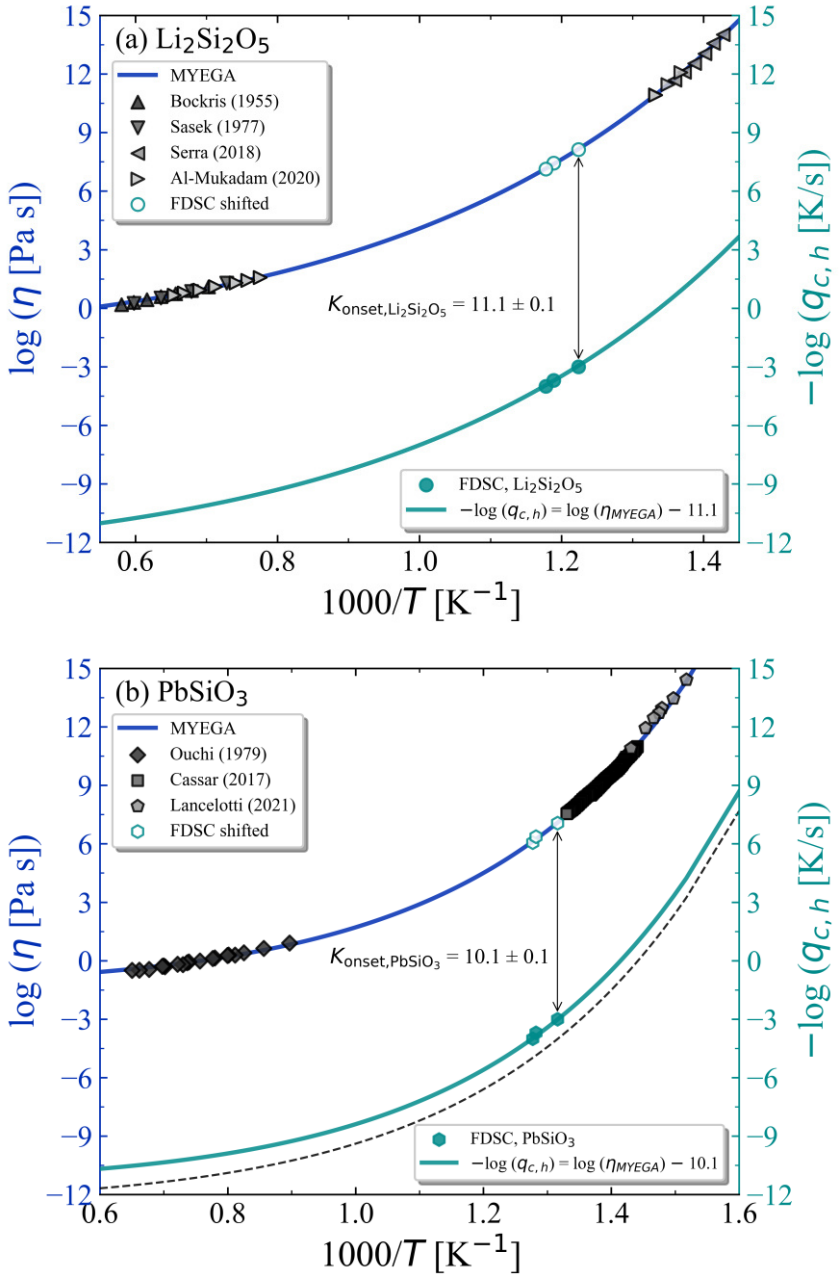

Figure 3.4: Arrhenian diagram of equilibrium shear viscosity from literature [64,102,108–112] is shown on the left axis (blue). On the right axis (dark cyan), the reciprocal cooling/heating rates vs. reciprocal T_f are displayed for the (a) $Li_2Si_2O_5$ and (b) $PbSiO_3$ glasses. Solid blue curves represent the MYEGA regressions (Eq. (3.1)) obtained using viscosity data. Solid dark cyan curves and open dark cyan symbols are the shifted data used to obtain the shift factors of $K_{onset,Li_2Si_2O_5} = 11.1 \pm 0.1$ and $K_{onset,PbSiO_3} = 10.1 \pm 0.2$. Dashed black curve for the $PbSiO_3$ glass is plotted considering a composition-independent shift factor of 11.1 [102], which proved to be inadequate for describing the measured data.

Figure 3.5 shows the heat flow curves obtained at a reheating rate of 5,000 K/s after cooling at rates of 10,000, 5,000, 1,000, 500, 100, and 50 K/s. In the glass transition region, the glasses cooled at different rates recover back to the metastable SCL equilibrium state, exhibiting overshoots in the FDSC curves. The area of these overshoot peaks decreases with increasing cooling rates, correlating with the enthalpy released, as previously discussed for the similar findings using conventional DSC [98,99].

Each $T_{g,\text{onset}}$ value, derived from **Figure 3.5**, is an average of 6–8 measurements to ensure that the material has not crystallized during cooling, which resulted in an error bar of ± 2 K for most cases. The $T_{g,\text{onset}}$ values for glass samples with different T_f values are presented in **Figure 3.6**. When the material is slowly cooled and then quickly heated ($q_h > q_c$), there is not enough time for relaxation within the experimental time-scale until reaching the glass transition region, where the relaxation time is of the same order of magnitude as the experimental time. Therefore, the glass transition temperature, measured here as $T_{g,\text{onset}}$, shifts to lower temperatures as the cooling rate increases. In contrast, when the material is quickly cooled and slowly heated ($q_h < q_c$), there is sufficient time for structural relaxation during the heating stage, resulting in negligible variation in the measured $T_{g,\text{onset}}$. This latter behavior is evident on the right side of the dash-dotted line for both glasses. It is well-known that $T_{g,\text{onset}}$ increases as the experimental time decreases because of the use of higher heating rates [34]. However, **Figure 3.6** shows $T_{g,\text{onset}}$ values obtained using the same heating rate of 5,000 K/s, demonstrating different behaviors related to the structural relaxation phenomenon, resulting from diverse cooling rates for glass samples with varying compositions and atomic structures.

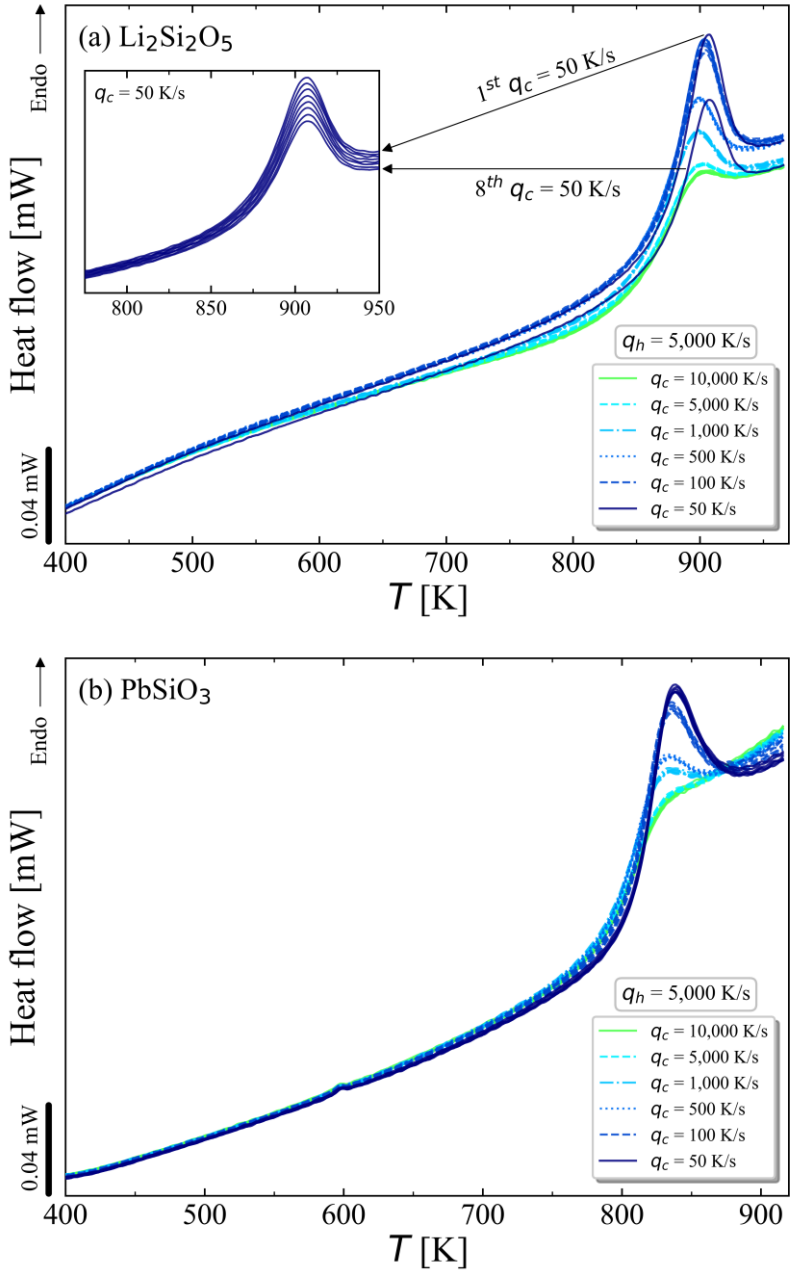

Figure 3.5: FDSC scans obtained at a constant q_h of 5,000 K/s in the glass transition region for (a) $Li_2Si_2O_5$ and (b) $PbSiO_3$ glass samples cooled at different q_c. For $Li_2Si_2O_5$, only the first and eighth heating curves are presented after cooling at 50 K/s. Inset shows the remaining curves that did not overlap using the lowest cooling rate, q_c = 50 K/s, as they probably crystallized during the slower cooling path.

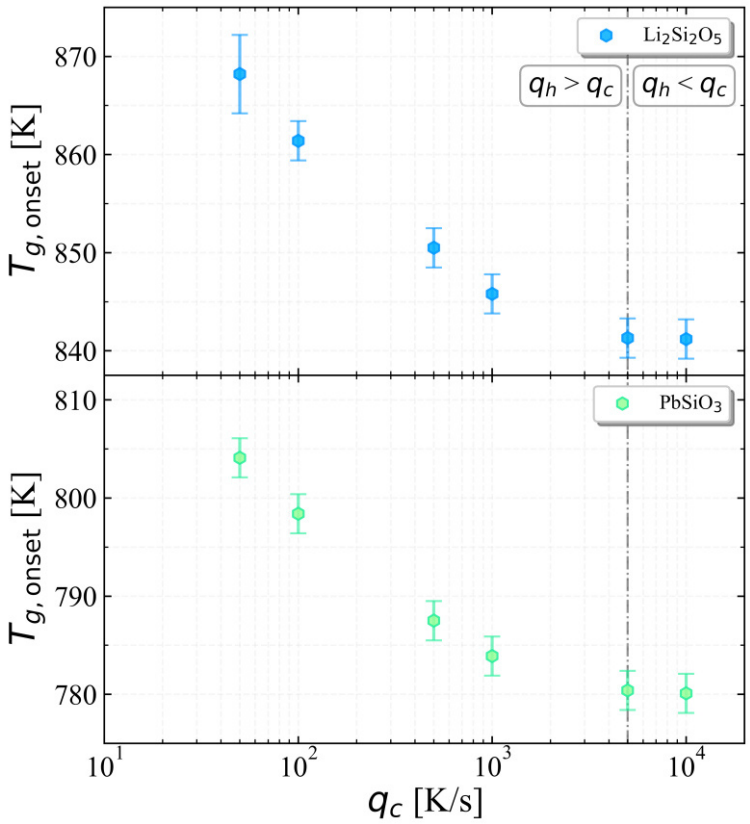

Figure 3.6: $T_{g,\text{onset}}$ obtained at a constant heating rate of 5,000 K/s as a function of previous cooling rates for $Li_2Si_2O_5$ and $PbSiO_3$ glasses. The data indicate that $T_{g,\text{onset}}$ values differ when $q_h > q_c$ and are equal when $q_h < q_c$. Dash-dotted line represents the condition where $q_h = q_c$.

It should be noted that **Figure 3.5** reveals distinct behaviors for the $Li_2Si_2O_5$ and $PbSiO_3$ glasses. All curves of the $PbSiO_3$ glass overlapped for all cooling rates. However, when the $Li_2Si_2O_5$ glass was cooled at a rate of 50 K/s (the slowest applied rate), partial stoichiometric crystallization probably occurred. The curves obtained from these runs at 50 K/s are shown in the figure inset. This result indicates that $PbSiO_3$, even with only 50 mol% of SiO_2, is a better glass former than $Li_2Si_2O_5$. This finding is corroborated by the *Jezica* parameter [115], which evaluates glass-forming ability (GFA) based on viscosity and liquidus temperature (T_L), GFA $\propto \eta(T_L)/T_L^2$. The GFA reflects the easiness to vitrify a liquid on the cooling path, while glass stability denotes the resistance against devitrification during heating. Using T_L values of 1,311 K for $Li_2Si_2O_5$ and 1,037 K for $PbSiO_3$ [116,117], along with $\eta(T_L)$ values obtained from the MYEGA equation (Eq. (3.1)), the calculated *Jezica* parameters were 1.8×10^{-5} Pa s/K^2 for $Li_2Si_2O_5$ and

2.2×10^{-5} Pa s/K^2 for $PbSiO_3$. Therefore, these results indicate that $PbSiO_3$ has a higher GFA than $Li_2Si_2O_5$, in agreement with the current results.

To explain the structural details underscoring the unusual GFA of this metasilicate, it has been proposed that $PbSiO_3$ glass consists of two subnetworks: one formed by SiO_4 tetrahedra and the other by PbO_x polyhedra (x = 3–5) [118]. In this context, Pb could be considered a cation that partially contributes to the network structure, exhibiting network-forming-like behavior, in contrast to Li in $Li_2Si_2O_5$ glass, which, as an alkali cation, is more randomly distributed throughout the structure, providing local charge neutrality and serving only as a network modifier [30]. Conversely, Sen et al. [119] in a recent study of the isotropic and anisotropic ^{207}Pb nuclear magnetic resonance spectra of glasses within the PbO-SiO_2 system reported that a significant fraction of Pb-O-Pb linkages appears only in glasses with PbO ≥ 60 mol%. They propose that the exceptional GFA conferred by PbO as an additive to SiO_2 is possibly due to the formation of an open and highly interconnected network of PbO_n pyramids and SiO_4 tetrahedra. Furthermore, they suggest that the presence of a small concentration of silicate anions is crucial to the stability of the network.

It is important to note that all the FDSC experiments were conducted using only one specimen of each glass (see **Figure 3.1** for $Li_2Si_2O_5$). The inability to reproduce the $Li_2Si_2O_5$ heat flow curves after cooling at 50 K/s could be attributed to the slight crystallization of the sample during each cooling run at this comparatively slow rate. The sample was not analyzed after the FDSC experiments because of the practical limitations associated with the equipment, as micrometric samples tend to flow and adhere to the sensor, making further use of both the sensor and the sample challenging. Although it is technically possible, as demonstrated in a very recent study that successfully analyzed the sample after FDSC measurements by removing it from the sensor and subsequently preparing it using Focused Ion Beam technology for Transmission Electron Microscopy analysis [120].

Regarding the crystallization behavior of $Li_2Si_2O_5$, Ota et al. [121] directly measured the critical cooling rate (q_{cr}) using optical microscopy to examine the surface and interior of samples quenched at different rates, and reported a value of 1 K/s. Similarly, Asayama et al. [122] applying microscopy, determined a q_{cr} of approximately

5 K/s. However, $Li_2Si_2O_5$ exhibited significant changes in its heat flow curves for a cooling rate of 50 K/s, which is at least 10 times higher than these reported q_{cr} values.

The experimental, microscopy-based methods employed to obtain these critical cooling rates may *underestimate* the correct values, as they depend on the nucleation and growth of crystals to a size that is detectable under a microscope. In contrast, the flash-DSC technique eliminates the need for such observations, proving to be a powerful tool for investigating these critical cooling rates through multiple cooling and heating cycles. Additionally, it is known that GFA heavily depends on the chosen measurement technique and on the fact that, when surface crystallization prevails over internal nucleation, the critical cooling rate is increased.

3.4 Conclusions

The application of the flash-DSC technique enabled the determination of fictive temperatures, which were subsequently used to obtain the composition-dependent shift factors, $K_{\mathrm{onset,Li_2Si_2O_5}} = 11.1 \pm 0.1$ and $K_{\mathrm{onset,PbSiO_3}} = 10.1 \pm 0.2$, contradicting assumptions from previous studies. Additionally, by employing glass samples obtained with widely different cooling rates followed by a constant heating rate of 5,000 K/s, the impact of the cooling rate on the glass transition temperature was demonstrated, thus shedding light on the relationship between structural relaxation and experimental timing. The results also demonstrated the superior glass-forming ability of $PbSiO_3$ compared to $Li_2Si_2O_5$, as the latter partially crystallized during cooling at a slow rate of 50 K/s.

CHAPTER 4 – RELAXATION KINETICS VIA REFRACTIVE INDEX AND IONIC CONDUCTIVITY

4.1 Introduction

The dependence of the relaxation kinetics on the specific property being measured has been studied by many authors; however, the current situation is still controversial. While some researchers argue that the relaxation kinetics is the same for different properties, others sustain that it is different.

DeBolt et al. [123] compared their enthalpy (H) relaxation data of B_2O_3 glass at 536 K with the Boesch et al. [124] refractive index (n) relaxation data for the same glass composition and temperature, and found that enthalpy relaxes faster than refractive index. In a classic paper, Moynihan et al. [93] summarized the kinetic parameters of the structural relaxation process of several authors and materials, and concluded that the average relaxation time and the non-exponentiality parameter are different for different properties of the same glass. Although those authors compared some properties for the same temperature and nominal glass composition, the measurements were performed by different research groups using glass samples of different batches, which were produced and measured in different environments. Hence, because of the likely difference in impurity contents, especially water, which strongly affects relaxation dynamics, this comparison is subject to significant uncertainty.

An aging study conducted by Sasabe and Moynihan [125] compared the enthalpy and dielectric relaxation results of samples from the same batch of poly(vinyl acetate) (PVAc) above the glass transition region. They also found that enthalpy and dielectric relaxation measured at the same temperature seemed to be characterized by somewhat different relaxation times. Also, Dingwell and Webb [33] compiled relaxation times in $Na_2Si_3O_7$ melt from shear viscosity and electrical relaxation data. As expected, they showed that the relaxation times estimated from electrical modulus are much faster than those from shear viscosity. Therefore, all these studies indicated significant differences in relaxation dynamics probed by distinct properties.

On the other hand, Rekhson et al. [126] analyzed a window glass and reported that volume and viscosity relax with similar kinetics within the experimental uncertainty. Webb et al. [127] concluded that relaxation times for shear viscosity, volume, and

enthalpy are equivalent in $Na_2Si_2O_5$. Also, Echeverría et al. [128] investigated the relaxation behavior of amorphous selenium through enthalpy recovery and the creep-recovery response. They found that the times to reach equilibrium seem to be the same in the glass transition region, but to diverge at lower temperatures, with enthalpy coming to equilibrium before volume and creep. Málek et al. [22] also used amorphous selenium to study the specific volume and enthalpy relaxation in the glass transition region. Their relaxation parameters were only slightly different, and they concluded that these two properties relax with the same kinetics.

In this chapter, the objective is to verify this controversy by systematically comparing the structural relaxation dynamics throughout the physical aging of a lithium disilicate ($Li_2Si_2O_5$) glass through changes in refractive index, n, and DC conductivity, σ_{DC}, at several temperatures below the initial T_f. In this case, these two properties were measured in glass samples from the same batch, treated at identical conditions.

4.2 Materials and Methods

The $Li_2Si_2O_5$ glass used in this chapter is from the same batch described in Chapter 3, with a T_g of (727 ± 2) K. A portion of this glass was annealed at 663 K for 2 h, followed by slow cooling to room temperature at 3 K/min to alleviate the residual stresses and allow sample preparation.

The samples were divided into two sets so that glasses with two different initial fictive temperatures could be obtained. The first set was treated at 720 K ($T_{f,1}$) and the second set at 727 K ($T_{f,2}$), both for 4 h, which is sufficient to reach their metastable SCL equilibrium state (> 99% relaxed). Subsequently, physical aging experiments were conducted by alternating isothermal treatments at $T < T_f$, with determinations of refractive index at room temperature and ionic conductivity at 308 K. To this end, the samples from the first set were subjected to isothermal treatments at different temperatures (705, 695, and 685 K), which are 15, 25, and 35 K below $T_{f,1}$, and those from the second set at 703 K, which is 24 K below $T_{f,2}$, for cumulative times, that is, the samples were heat treated at the indicated temperature, taken out of the furnace, had their proprieties measured, and were inserted back into the furnace at the study temperature until a constant value within the experimental error was reached. The experimental data were fitted with a KWW-type function (Eq. (2.7)).

The refractive index was measured at a wavelength λ of 546.1 nm (e-line) using a high-precision V-block refractometer (Pulfrich PR2, Carl Zeiss), equipped with a VoF5 glass prism having a refractive index $n_{\lambda,p}$ = 1.74800(1) at the e-line. The reported refractive index values were obtained at room temperature from an average of 10 consecutive measurements in samples of 10 × 10 × 3 mm^3 with perpendicular polished faces. The refractometer measures the angle of the refracted beam γ from a sample placed on the V-prism with a thin layer of immersion oil. The wavelength-dependent refractive index n_λ is then correlated with that of V-prism through the following equation:

$$n_\lambda = \sqrt{n_{\lambda,p}^2 - \cos(\gamma)\sqrt{n_{\lambda,p}^2 - \cos^2(\gamma)}}. \quad (4.1)$$

The ionic conductivity of the samples was obtained through electrochemical impedance spectroscopy (EIS) using an impedance analyzer (Alpha-A, Novocontrol), measuring the magnitude of the impedance $|Z|$ and phase angle ϕ. The experiments were performed at 308 K in a frequency f range of 10^{-1}–10^7 Hz and voltage amplitude of 300 mV. The two samples used had two parallel surfaces with thickness and area values of l_1 = 0.2875(5) cm and S_1 = 0.696(2) cm^2, and l_2 = 0.3185(5) cm and S_2 = 0.902(1) cm^2, respectively. Before the measurements, gold electrodes were sputtered on the two parallel surfaces using a sputter (Q150R ES, Quorum) with current of 20 mA and time deposition of 300 s. The Fourier domain impedance is a complex function [129]:

$$Z(\omega) = |Z|\cos(\phi) - |Z|i\sin(\phi) = Z'(\omega) - iZ''(\omega), \quad (4.2)$$

where ω ($2\pi f$) is the angular frequency and i is $\sqrt{-1}$. Impedance data can be represented in several correlated formalisms, including the impedance complex plane plot with the imaginary part of impedance $-Z$'' at the y-axis and the real part Z' at the x-axis. Sample resistance (R) can be directly read at the low-frequency intersection of the semicircle with the real x-axis. Thus, σ_{DC} is calculated by the following equation:

$$\sigma_{DC} = \frac{1}{R}\frac{l}{S}. \quad (4.3)$$

4.3 Results and Discussion

Figure 4.1 shows the temporal variation of the refractive index and DC conductivity during the isothermal heat treatments at 705, 703, 695, and 685 K of $Li_2Si_2O_5$ samples pre-annealed at 720 and 727 K.

The magnitude of property changes associated with completing relaxation increased as the study temperature moved away from the initial T_f toward lower temperatures, corroborating previous results for other glasses via refractive index [13,64,130] and DC conductivity [69]. **Figure 4.2** shows the results from EIS experiments conducted at 308 K for a sample pre-annealed at 720 K and aged at 695 K for different times. It is important to emphasize that, unlike other studies [33,68,131], this investigation did not measure electrical relaxation, which leads to a very fast relaxation behavior. Instead, the ionic resistivity (ρ, the inverse of DC conductivity) was directly obtained from the low-frequency intersection of the semicircle with the x-axis, since the impedance results were normalized by the geometrical factor of the sample (l/S, respectively, sample thickness and area).

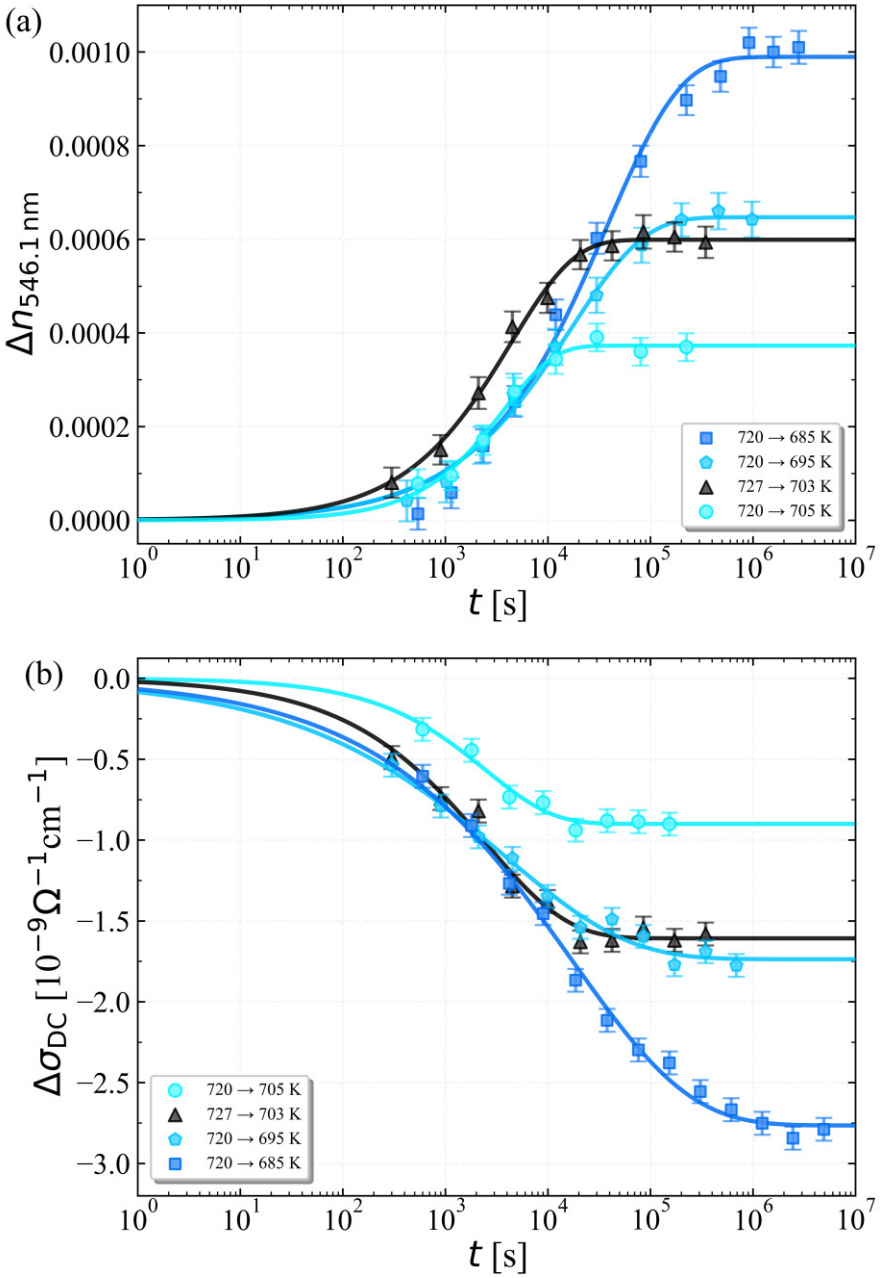

Figure 4.1: Variation of (a) refractive index and (b) DC conductivity of a $Li_2Si_2O_5$ glass as a function of aging time for four experiments below a pre-established initial T_f. Solid lines are the KWW function regressions (Eq. (2.7)).

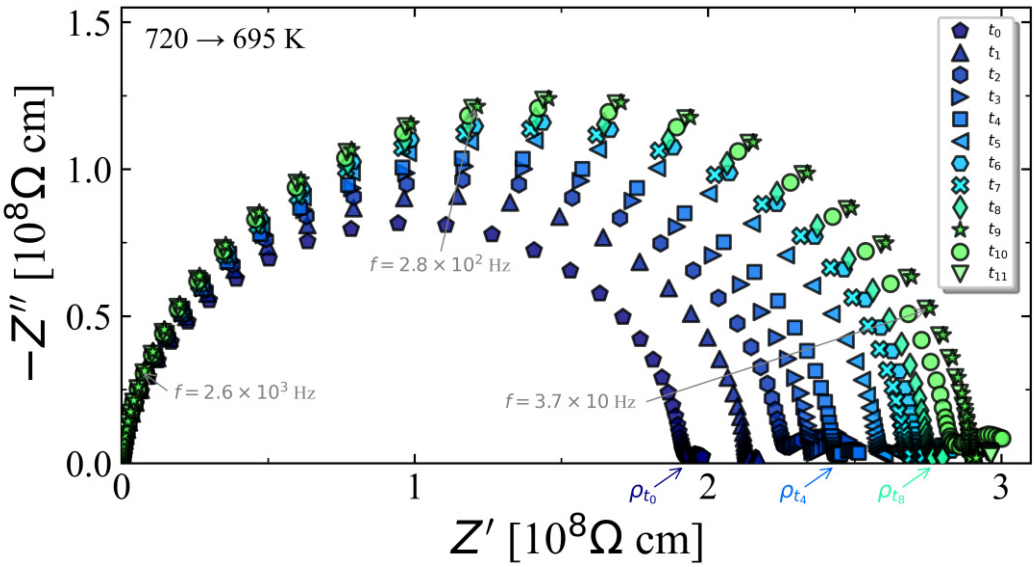

Figure 4.2: Impedance complex plane plots measured at 308 K for a sample ($l/S = 0.413$ cm^{-1}) pre-annealed at 720 K and aged at 695 K by $t_0 = 0$ s, $t_1 = 300$ s, $t_2 = 900$ s, $t_3 = 2{,}100$ s, $t_4 = 4{,}500$ s, $t_5 = 9{,}900$ s, $t_6 = 20{,}700$ s, $t_7 = 42{,}300$ s, $t_8 = 85{,}500$ s, $t_9 = 171{,}900$ s, $t_{10} = 344{,}700$ s, and $t_{11} = 690{,}300$ s.

Property variations are strongly linked to the difference between the initial T_f and the measurement temperature. For example, a similar variation is observed when the property is measured at $T_{f,1} - 25$ K = 695 K and $T_{f,2} - 24$ K = 703 K (see **Figure 4.1**), even though the initial fictive temperatures and also the studied temperatures were different. **Figure 4.3** illustrates this behavior for DC conductivity data, showing results for two different initial fictive temperatures (720 and 727 K). The samples were heat treated at different temperatures (685, 695, 703, and 705 K) for cumulative times and measured at 308 K.

These temporal changes, as measured by refractive index and DC conductivity, were fitted by the KWW function, which described quite well all the experimental data. **Figure 4.4** shows the adjustable parameters ($p_\infty - p_0$, τ_k, and β) obtained from regressions, as well as the average relaxation time, $\langle\tau\rangle$. Linear regression analyses were performed considering one standard deviation.

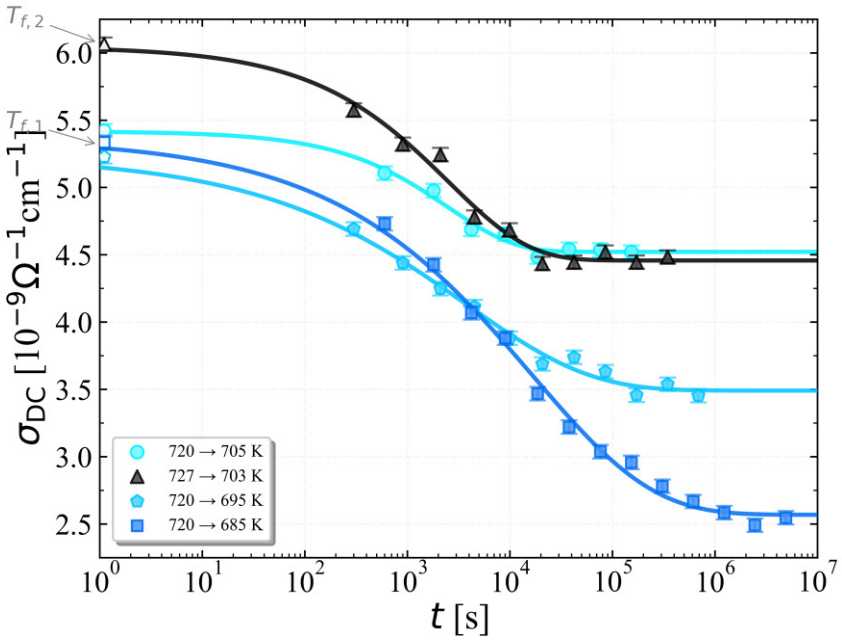

Figure 4.3: Temporal evolution of DC conductivity measured at 308 K of a $Li_2Si_2O_5$ glass during aging at different temperatures. Open symbols refer to the values of DC conductivity measured at $t = 0$ s, i.e., the values for the initial T_f.

The results shown in **Figure 4.4** indicate a relationship between each parameter and the temperature. The difference $p_\infty - p_0$ is zero for $T = T_f$. When the difference between the T_f and the study temperature increases in the $T < T_f$ range, $n_\infty - n_0$ also increases, whereas $\sigma_\infty - \sigma_0$ and β decrease, and τ_k and $\langle\tau\rangle$ increase exponentially. These results agree with those previously reported for a lead metasilicate glass via changes in refractive index [64].

Figure 4.5 shows the relaxation parameter, ϕ, as a function of time. The DC conductivity undergoes a faster start of relaxation, which yields a lower characteristic relaxation time, as shown in **Figure 4.4**(c). The DC conductivity also has the lower β, **Figure 4.4**(b). Eq. (2.6) demonstrates that these two parameters have distinct effects on $\langle\tau\rangle$, resulting in a very similar average relaxation time for both properties. The aging results at $T_{f,1} - 35$ K, shown in **Figure 4.5**(c) have the larger change in T_f and, consequently, larger property variations and lower uncertainty.

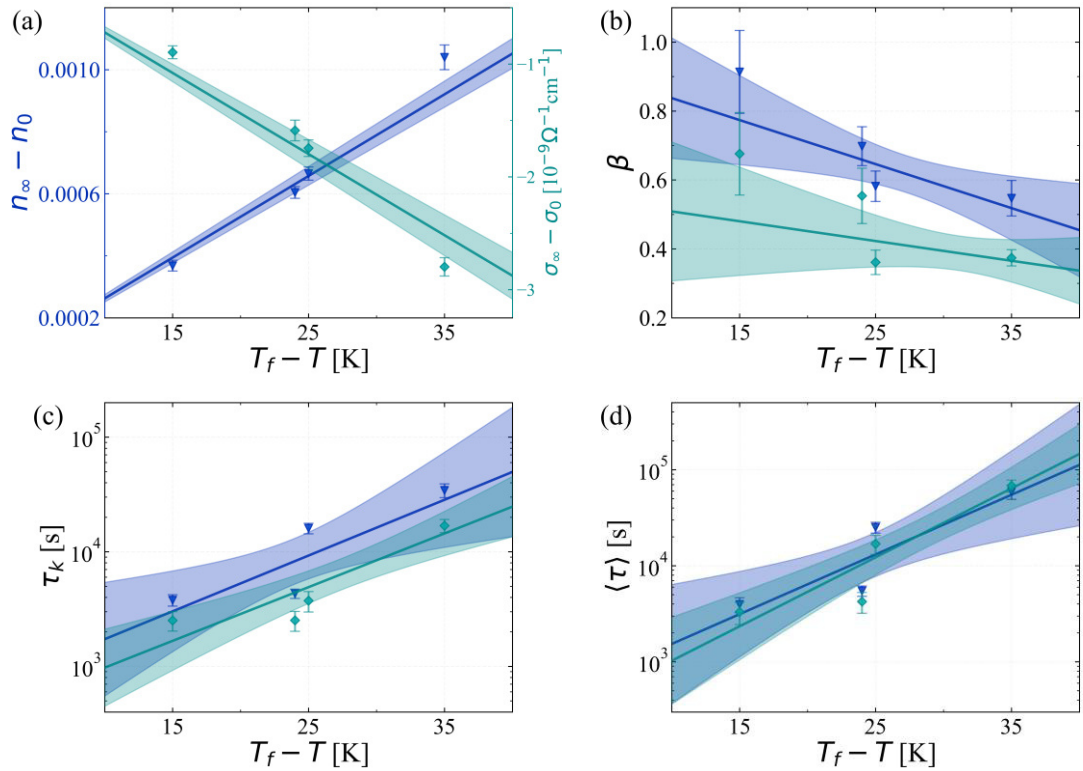

Figure 4.4: Parameters related to the relaxation of refractive index (blue triangles) and DC conductivity (dark cyan diamonds): (a) variation of properties, (b) non-exponentiality parameter, (c) characteristic relaxation time, and (d) average relaxation time. Solid lines represent linear regressions and the shaded areas show the confidence bands.

The DC conductivity changes faster at the beginning of the process and has a lower β than refractive index, but they show similar average relaxation times. The non-exponentiality parameter β is a measure of the width of the relaxation dynamics, encompassing the slowest to the fastest structural groups in the α-relaxation and the so-called slow β-relaxation (as opposed to fast β-relaxation). In other words, the characteristic relaxation time and the non-exponentiality parameter resulting from conductivity measurements are *shorter* than those obtained from refractive index; however, the average relaxation times are similar.

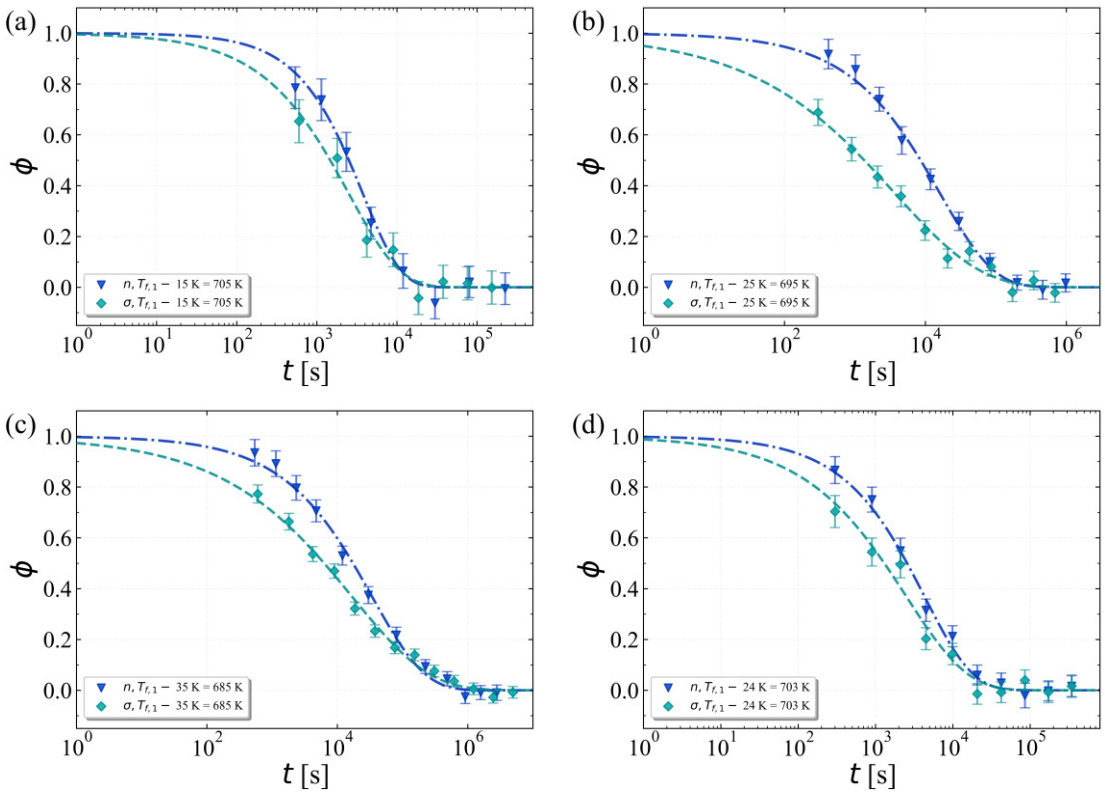

Figure 4.5: Relaxation parameter as a function of heat treatment time calculated by the variation of the refractive index and DC conductivity at (a) $T_{f,1}$ − 15 K, (b) $T_{f,1}$ − 25 K, (c) $T_{f,1}$ − 35 K, and (d) $T_{f,2}$ − 24 K.

It has been demonstrated that classifying the relaxation type as α- or slow β-relaxation based on different properties in not straightforward. Indeed, ionic conductivity was measured by the migration of lithium ions in the $Li_2Si_2O_5$ glass, but this process becomes easier or more difficult by the cooperative relaxation of the lattice depending on whether the conductivity is measured above or below the fictive temperature [69]. Moreover, as shown in **Figure 4.4**, the non-exponentiality parameter is a function of both temperature and thermal history and decreases as the temperature moves away from the initial T_f towards lower temperatures. This result agrees with other experimental findings [64,92].

Lower β result from relaxation at lower temperatures as well as from some properties such as conductivity, whereas the refractive index yields larger β. Consequently, it is possible to distinguish different kinetics in the same sample by measuring different properties at a given temperature. Recently, the temperature dependence of β has been discussed [8,132]. It is sometimes assumed that β is a constant

of 3/5 or 3/7, as derived by Phillips [21,91] and experimentally indicated by other authors [89,133], or that it is only temperature dependent [92]. The current results showed herein evidence that β indeed depends on the measurement temperature, the fictive temperature, and also on the analyzed property, i.e., $\beta(T, T_f, p)$.

Therefore, the measured structural relaxation kinetics depends on the analyzed property, which corroborates the findings of some previous studies [93,123–125]. The dependence of relaxation dynamics on the measured property may be explained by the different effects that structural rearrangements of the glass have on each property. These rearrangements increase the glass density when the study temperature is lower than the initial fictive temperature [12,134], and change the local environment of the lithium ions [135]. Thus, changes in density may have a greater influence on the refractive index, whereas the ionic conductivity may be more influenced in the early stages by changes in the distance of lithium ions, although it is also affected by changes in density. The structural changes are always the same, but small structural rearrangements at the beginning of the process imply more marked changes in ionic conductivity than in refractive index.

4.4 Conclusions

At all temperatures, the property variations were precise enough to capture the structural changes during the relaxation process. The KWW function has described quite well all the isothermal experimental relaxation data. The results confirmed that the non-exponentiality parameter is indeed complex, since it is a strong function of the measurement temperature, fictive temperature, and analyzed property. The relaxation process starts faster when measured by ionic conductivity than by refractive index. Ionic conductivity also shows a lower non-exponentiality parameter than refractive index; however, both properties present similar average relaxation times. This means that the very small structural rearrangements that occur at the beginning of glass relaxation have a greater influence on ionic conductivity, whereas refractive index is more influenced by the more cooperative α-relaxation. As a result, the relaxation kinetics depends on the analyzed property.

CHAPTER 5 – STRUCTURAL RELAXATION FOLLOWING TEMPERATURE UP- AND DOWN-JUMPS

5.1 Introduction

Several studies have reported that, in some cases, the structural relaxation dynamics can be faster than exponential, i.e., a compressed exponential with the non-exponentiality parameter $\beta > 1$ [136–145]. It should be noted that a compressed exponential function cannot be expressed as a sum of exponentials (as shown in Chapter 2, Eq. (2.9)), but may originate from a sum of Gaussian decay functions [138],

$$\phi(t) = \sum_{i=1}^{N} w_i \exp\left[-\left(\frac{t}{\tau_i}\right)^2\right]. \quad (5.1)$$

For instance, Vela and Simmons [142] performed simulations of model polymeric and small-molecule glass-formers in the iso-configurational ensemble and observed that non-exponential relaxation is not solely a consequence of spatial averaging over a distribution of locally exponential processes, and it cannot be interpreted as a direct measure of dynamic heterogeneity through spatial averaging. A range of non-exponential relaxation behavior is displayed even at the level of a single particle without time averaging. Their findings indicate that faster-relaxing particles in low-density regions of a liquid tend to exhibit locally stretched relaxation, while slower-relaxing particles in high-density regions show compressed relaxation.

Jaeger and Simmons [145], in their physical aging experiments involving up- and down-jumps in temperature, identified compressed exponential relaxation in up-jump experiments with large temperature jumps. It should be noted that up-jump aging experiments are characterized by a reduction in glass density as the T_f increases over time [12,134]. In separate experiments conducted by Guerette et al. [140], a silica glass was densified under hot compression at 4 GPa and 1,373 K (T_g of approximately 1,473 K). This led to a significant increase in the refractive index, from 1.461 to 1.525, and in density, from 2.20 to 2.53 g/cm^3. Then the glass structure was isothermally relaxed at 1,123 K. During this process, the refractive index returned to its initial value of approximately 1.461 and the density to 2.20 g/cm^3, a behavior similar to that observed in

temperature up-jump experiments. In this case, relaxation followed a compressed exponential decay of index and density with $\beta = 1.28$.

The shape of the relaxation function in up- and down-jump experiments are expected to be distinctly different. The down-jump data typically display a stretched exponential relaxation, while many of the up-jump data exhibit a compressed exponential recovery [12,22,134,146]. This difference in kinetics between the up- and down-jump experiments is a manifestation of the fact that the relaxation rate in the glassy state depends not only on the actual temperature but also on the T_f of the glass, where the latter evolves over time differently for the two experiments. In other words, this difference in kinetics results from the non-linear effect of the intrinsic structural changes, as described by the TNM model presented in Chapter 2. While this model is widely utilized in the literature, its phenomenological nature does not provide a clear insight into the physical origin of the non-linearity parameter x, its temperature dependence, or whether it should be related to the non-exponentiality parameter β. Moreover, the inadequacy of the TNM model for large temperature jumps (larger than 30 K in a silicate glass, which corresponds to a magnitude of ~4.2% in terms of $\Delta T/T_g$) was noted by Moynihan [147] himself, as well as by other authors under similar circumstances [67,148–150].

In this chapter, the objective is to apply and test the validity of the KWW function and the TNM model by monitoring enthalpy recovery and refractive index changes following temperature up- and down-jumps (up to 40 K, $\Delta T/T_g = 5.5\%$), using lithium disilicate glass ($Li_2Si_2O_5$), which exhibits good thermal stability against moisture and crystallization for long physical aging experiments below T_g.

5.2 Materials and Methods

The $Li_2Si_2O_5$ glass used in this chapter is from the same batch used and described in the previous chapters, with a T_g of (727 ± 2) K.

For the refractive index measurements, two samples (referred to here as sample I and sample II) of ~10 × 10 × 3 mm^3 were cut using a diamond saw, and their two perpendicular faces were polished to optical quality. Initially, the starting fictive temperature T_0 of samples I and II was set by annealing the samples at 720 K for 4 h.

For the enthalpy measurements, the process started by annealing a sample of similar dimensions (10 × 10 × 3 mm^3) at a temperature 40 K below its T_g for 15 days

(687 K, starting temperature T_0), aiming to lower the T_f. The sample was annealed at 687 K (40 K below T_g) for 15 days based on the results of a previous study on refractive index relaxation which indicated that, at 685 K, the same $Li_2Si_2O_5$ glass required 7 days to relax by 99% and 14 days to achieve practical equilibrium (99.9% relaxed) [151]. This sample was then fragmented into multiple small pieces for the subsequent aging experiments and enthalpy measurements. Some of these pieces were heat-treated at another starting temperature, 727 K for 6.5 h.

Structural relaxation during physical aging experiments was followed by monitoring changes in refractive index and enthalpy. Up- and down-jump experiments were performed, where samples were first equilibrated at T_0 for a specified initial time *t*, as shown in **Table 5.1**. Next, the samples were aged at temperature *T* until a constant value within the experimental error was reached. Some refractive index relaxation data were collected and reported in a previous study [151].

Table 5.1: Parameters used in each physical aging experiment.

Experiment	t in T_0	T_0 [K]	T [K]	Ref.
Ref. index, sample I	4 h	720	705	[151]
	32 days	685	705	–
Ref. index, sample II	4 h	720	695	[151]
	20 days	695	720	–
Enthalpy	15 days	687	717	–
	15 days	687	727	–
	6.5 h	727	717	–

The refractive index relaxation experiments using sample I were performed for jumps ending at the same temperature of 705 K. A temperature down-jump was executed from 720 to 705 K, and the refractive index was monitored over time, as reported in a previous study [151]. Subsequently, the same sample was rejuvenated by being annealed again at 720 K for 4 h, followed by equilibrating at 685 K for approximately 32 days. This sample equilibrated at 685 K was used to conduct an up-jump experiment at 705 K. For sample II, the down-jump from 720 to 695 K was conducted over approximately 20 days, followed by an up-jump to 720 K.

All refractive index measurements were carried using a similar procedure and equipment described in Chapter 4 after quenching the samples following each annealing

treatment. The evolution of the refractive index during aging was followed by periodically taking the sample out of the furnace at the end of each timestep, quenching it in air and stabilizing it for 20 min, performing an index measurement, and inserting it back into the furnace for the next timestep (i.e., the heat treatment was accumulative) until a constant index value was reached.

The enthalpy relaxation measurements were performed by annealing each small piece for a certain time period at a specific temperature *T* in a Mettler Toledo DSC1 under nitrogen atmosphere. For each experimental run, (10 ± 1) mg of the sample pre-equilibrated at 687 or 727 K was inserted into hermetically sealed aluminum pans. The isothermal temperature jump experiments comprised a series of steps. The initial step was aging the sample at a temperature *T* for a certain time, as schematized in **Figure 5.1**, exemplifying an aging experiment at 717 K for 60 min. Once the target aging temperature was reached on the DSC equipment, the sample was inserted to initiate the experiment. After the aging period, which ranged from 5 min up to 4 h, the sample was cooled from the aging temperature to 573 K (T_a) at a rate of 100 K/min. This cooling step was followed by a 5 min holding period at 573 K to ensure thermal stabilization. Subsequently, the sample was heated to about 50 K above the glass transition region (T_b) at a heating rate q_h of 10 K/min, producing a DSC heat flow scan $\dot{Q}$ in W/g. Following this scan, the sample was cooled to 573 K at a rate of 10 K/min, held for 5 min, and then reheated at the same rate to T_b to obtain the rejuvenated DSC heat flow curve $\dot{Q}_{rejuv}$ in W/g.

The enthalpy recovery ΔH_R given in J/g was determined from the difference in the area under the sample and rejuvenated heat flow curves as follows:

$$\Delta H_R = \frac{1}{q_h}\int_{T_a}^{T_b}\left(\dot{Q} - \dot{Q}_{rejuv}\right)dT, \tag{5.2}$$

where q_h is the heating rate and T_a–T_b is the integration temperature range, with $T_a < T_g < T_b$.

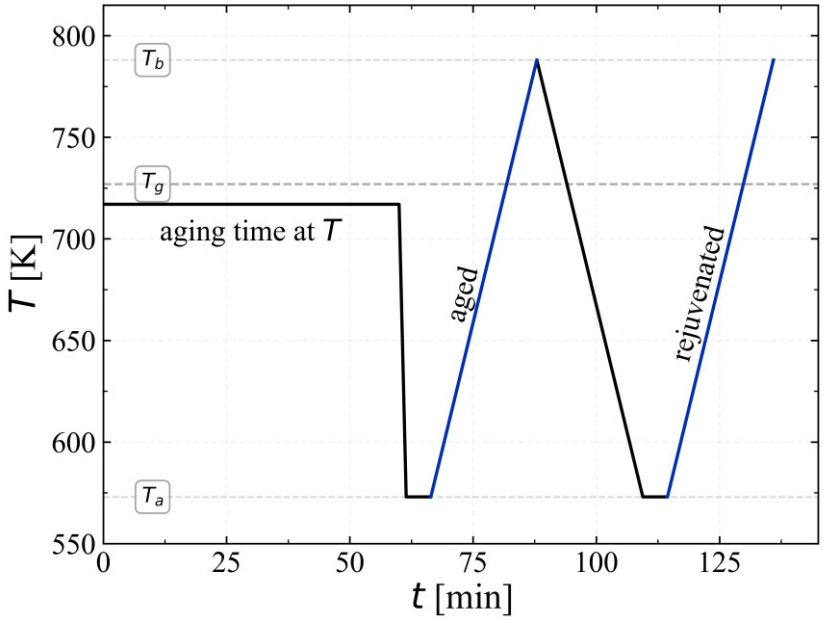

Figure 5.1: Schematic diagram of the physical aging protocol for enthalpy recovery experiments, illustrating an aging experiment at 717 K for 60 min.

Each temperature jump dataset was individually fitted with a KWW-type function (Eq. (2.7)) on the experimental refractive index and enthalpy data to obtain the parameter β. On the other hand, combined regressions were carried out for up- and down-jump experiments using the TNM model to simultaneously capture the non-exponential and non-linear nature of the aging kinetics [5,10,93,152]. To achieve this, the data were plotted using Eq. (2.11) and subsequently performed regressions using a numerical method to conduct the TNM fitting.

Initially, Eq. (2.12) was applied using the known parameters δ_0, T_0, and T. The evolution of $T_f(t)$ from T_0 to T was described by numerically integrating the reduced time using Eq. (5.3). For this numerical integration, the procedure detailed by Málek et al. [22] was adopted, where the total aging time was divided into j logarithmically spaced subintervals, with the relaxation response calculated at the end of each subinterval:

$$T_{f,j} = T + (T_0 - T)\exp\left[-\left(\sum_{j=1}^{n}\frac{\Delta t_j}{\tau_j}\right)^{\beta}\right]. \tag{5.3}$$

The subintervals, $\Delta t_j = t_j - t_{j-1}$, were divided into 500 logarithmic increments, and τ_j was calculated using Eq. (5.4):

$$\tau_j = A \exp\left(\frac{x\Delta h^*}{RT} + \frac{(1-x)\Delta h^*}{RT_{f,j-1}}\right). \quad (5.4)$$

Hence, the TNM model was fitted to the experimental data with β, A, and x as fitting parameters, while $\Delta h^*/R$ was fixed at 80.06 kK, obtained from the shear viscosity activation energy in the T_g region for the same $Li_2Si_2O_5$ batch used in this chapter. Therefore, this fitting procedure assumes that the structural relaxation process has the same activation energy as that of viscous flow, as demonstrated by Moynihan et al. [153] through comparisons of various glass-forming systems and supported by a recent study on the relaxation of $Li_2Si_2O_5$ glass [151].

5.3 Results and Discussion

The room temperature refractive index of the $Li_2Si_2O_5$ glass is shown in **Figure 5.2** as a function of aging time at 705 K for samples pre-aged at 720 K for 4 h and at 685 K for 32 days. In **Figure 5.2**(a), the refractive index variations were described by the KWW function, resulting in a stretching exponent of β_{KWW} = 0.93 for the temperature down-jump (720 to 705 K). In contrast, the up-jump (685 to 705 K) yielded a compressing exponent of β_{KWW} = 1.31. Although the down-jump data can be fitted reasonably well using β_{KWW} = 1.00, this value of the non-exponentiality parameter is unable to describe the up-jump data with significant accuracy. On the other hand, in **Figure 5.2**(b), the relaxation parameters δ were fitted using the TNM model. Both the up-jump and down-jump datasets could be fitted to the TNM model using β_{TNM} = 1.00 and x = 0.65. All parameters obtained from these fits are provided in **Tables 5.2** and **5.3**, corresponding to the KWW function and the TNM model, respectively.

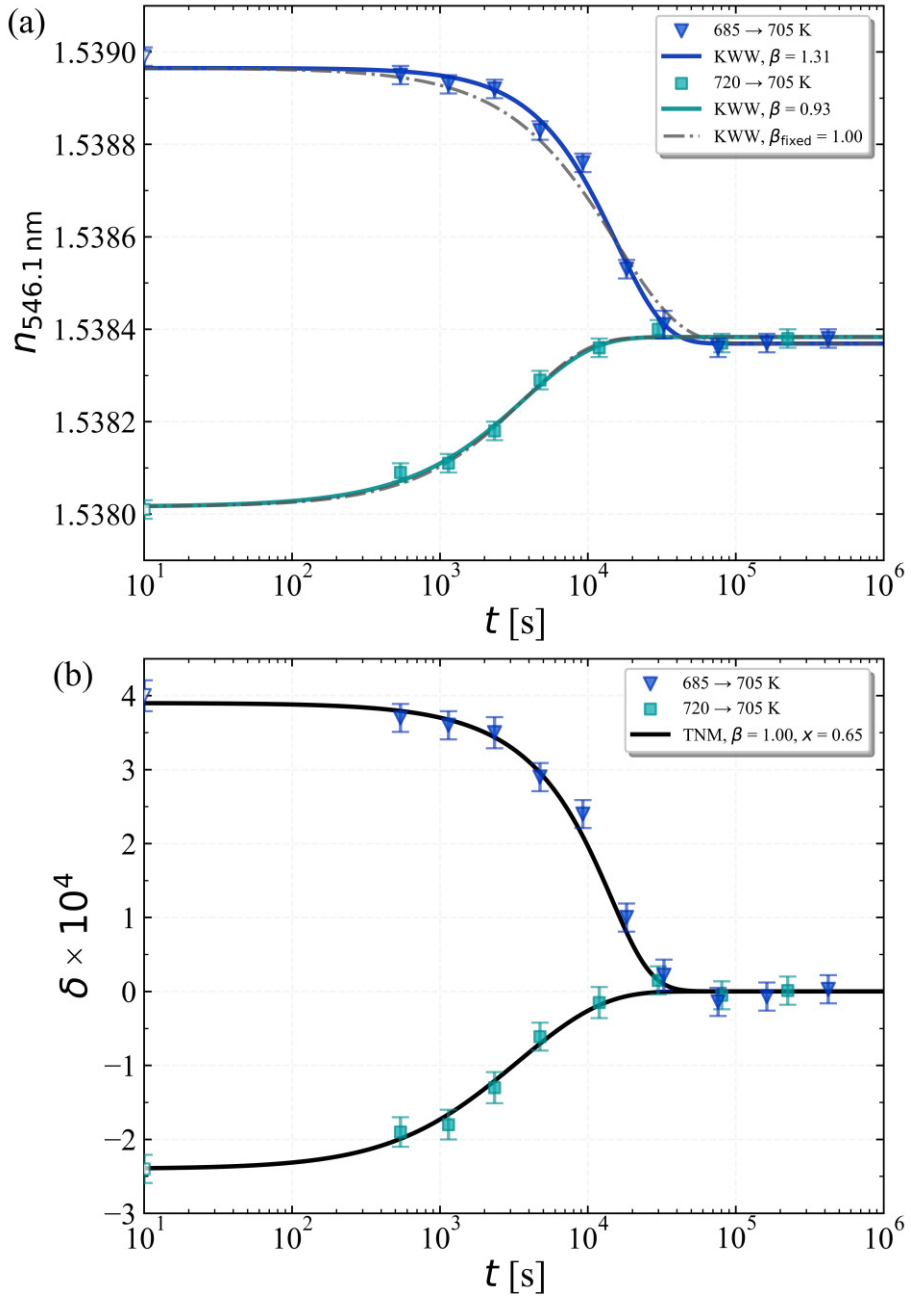

Figure 5.2: Room temperature refractive index relaxation data of sample I corresponding to temperature up- and down-jumps. Filled symbols refer to the refractive index values measured over time, while open symbols indicate the values at $t = 0$ s. (a) Solid lines represent fitting curves obtained using KWW function (Eq. (2.7)) and dash-dotted lines correspond to fits with a fixed β value of 1.00. (b) Solid lines represent TNM model fits via Eqs. (2.12), (5.3), and (5.4), which describe both datasets with a single set of β and x values.

Table 5.2: Summary of the KWW parameters.

Experiment	T_0 [K]	T [K]	p_0	p_∞	β_{KWW}	τ_K [s]
Ref. index, sample I	720	705	1.53802	1.53838	0.93	3711
	685	705	1.53896	1.53837	1.31	15592
Ref. index, sample II	720	695	1.53750	1.53815	0.56	17822
	695	720	1.53814	1.53752	1.94	3693
Enthalpy	687	717	25.2	3.1	1.22	4539
	687	727	24.9	0.6	1.43	1648
	727	717	0.8	3.3	0.87	983

Table 5.3: Summary of the TNM parameters.

Experiment	T_0 [K]	T [K]	δ_0	$\Delta h^*/R$ [kK]	ln (A [s])	β_{TNM}	x
Ref. index, Sample I	720	705	$3 \times 10^{-5} - 1.8 \times 10^{-5}(T_0 - T)$	80.06	-104.8	1.00	0.65
	685	705					
Ref. index, Sample II	720	695	$-1.5 \times 10^{-6} - 1.71 \times 10^{-5}(T_0 - T)$	80.06	-104.2	0.85	0.50
	695	720					
Enthalpy	687	717	$0.955 - 0.1705(T_0 - T)$	80.06	-104.3	0.90	0.66
	727	717					
Enthalpy	687	727	$5.988 - 0.6738(T_0 - T)$	80.06	-104.3	0.84	0.61
	727	717					

The DSC excess heat flow data obtained by subtracting the DSC curve of the rejuvenated glass from the aged glass are compiled in **Figure 5.3**. The structural recovery is observed through an endothermic enthalpy overshoot at the glass transition region. In the temperature up-jump experiment, the area of the endothermic peak decreases with increasing aging times, while for the down-jump experiment, it increases with increasing aging times. Since the glass structure is frozen, its atomic mobility below glass transition is markedly reduced. During the initial aging of the material at T_0, for example at 687 K for 15 days, volume relaxation results in an increase in density [12]. As a result, when this sample is heated, a greater amount of energy is required for the glass transition, resulting in a larger area under the endothermic peak [154]. However, when this sample is subjected to a temperature up-jump at T, the density decreases with aging time. Therefore, as the aging time increases, the sample requires less energy for glass transition, leading to a reduction in the area under the endothermic peak.

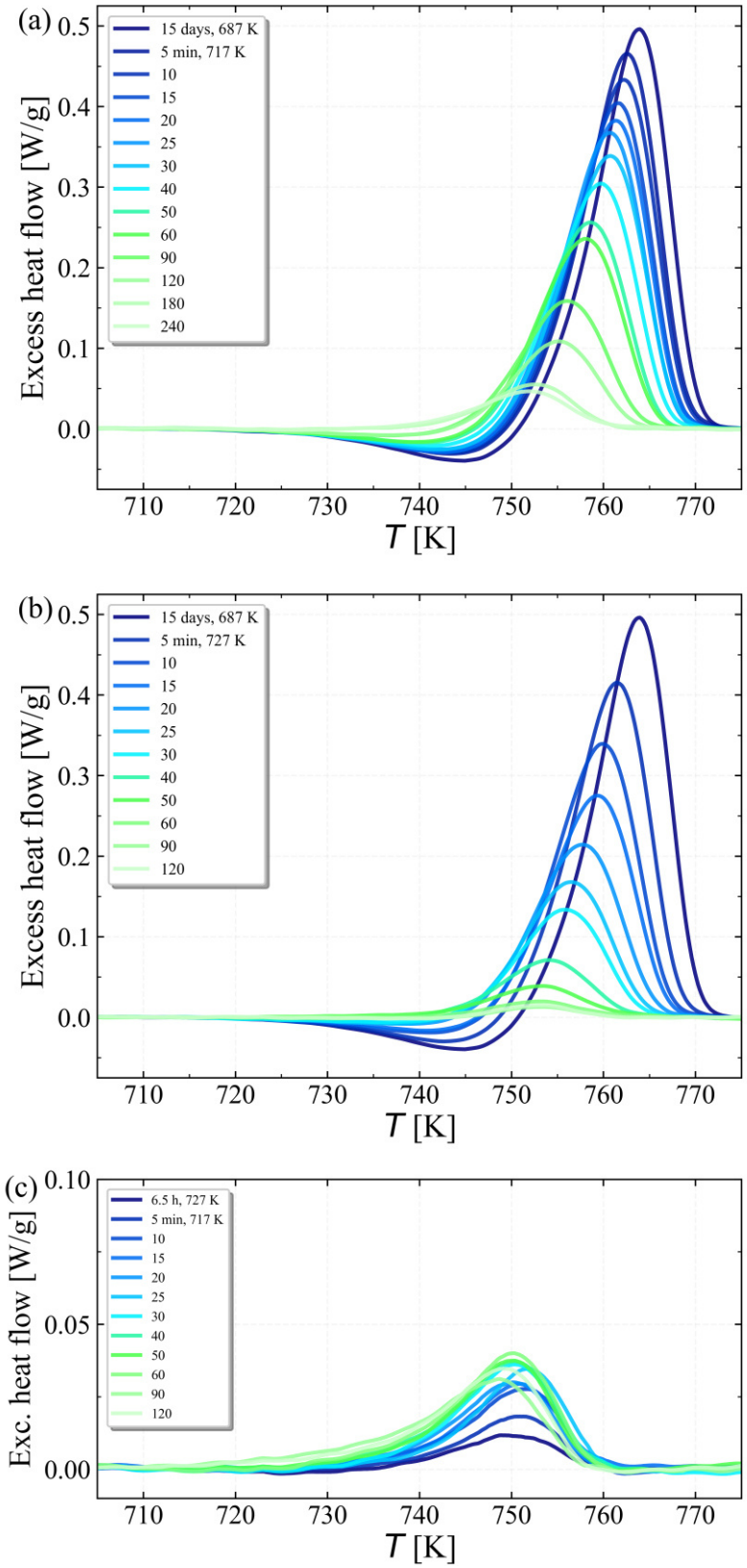

Figure 5.3: Excess heat flow scans after aging from T_0 to T. (a) 687 to 717 K, (b) 687 to 727 K, and (c) 727 to 717 K, at indicated aging times.

The enthalpy recovery ΔH_R was estimated from the endothermic peaks, and is presented in **Figure 5.4** as a function of aging time at 717 K and 727 K for samples pre-aged at 727 K for 6.5 h and at 687 K for 15 d. In **Figure 5.4**(a), the KWW fit yielded a stretched exponent of β_{KWW} = 0.87 for the temperature down-jump from 727 to 717 K. However, once again, for temperature up-jumps, it resulted in compressed exponents of β_{KWW} = 1.22 from 687 to 717 K, and β_{KWW} = 1.43 from 687 to 727 K. Even considering the measurement uncertainties, a fixed value of β_{KWW} = 1.00 was unable to describe the up-jump data at 727 K. Moreover, β_{KWW} increases markedly for larger temperature jumps. **Figure 5.4**(b) shows that the TNM model provides a good description of the data with somewhat similar β_{KWW} values of 0.87 and 1.22, when employing β_{TNM} = 0.90 and x = 0.66. However, as the difference between the β_{KWW} values increased for larger up- and down-jumps, the TNM model starts to exhibit a reduced capacity to describe the data. This is evident in **Figure 5.4**(c) considering the data with β_{KWW} values of 0.87 and 1.43 for an up-jump of 40 K, for which the TNM model was unable to describe the data using the same β_{TNM} = 0.90 and x = 0.66 (solid lines). In this particular case, the data were fitted with β_{TNM} = 0.84 and x = 0.61 (dashed lines). This is also shown in **Figure 5.5**, where the refractive index data at $T_0 - T$ = 25 K and $T_0 - T$ = − 25 K exhibit significantly different β_{KWW} values, both far from 1.0, as indicated by the dash-dotted green curves in **Figure 5.5**(a). In this case, the temperature down-jump data exhibit a behavior much slower than exponential with a β_{KWW} = 0.56, while the temperature up-jump data show a behavior much faster than exponential with a β_{KWW} = 1.94.

Figure 5.5(b) shows a reasonably good fit of the TNM model to the temperature up-jump data with β_{TNM} = 1.00 and x = 0.50, but a poor fit to the down-jump data. In contrast, **Figure 5.5**(c) shows a good fit to the down-jump data with a β lower than unit, β_{TNM} = 0.70, while keeping the same x = 0.50. However, these fitting parameters lead to a poor description of the up-jump data. Moreover, **Figure 5.5**(d) shows that an average value of the non-exponentiality parameter β_{TNM} = 0.85 does not provide the best fit for either dataset, but still approximately describes the data considering the measurement uncertainties.

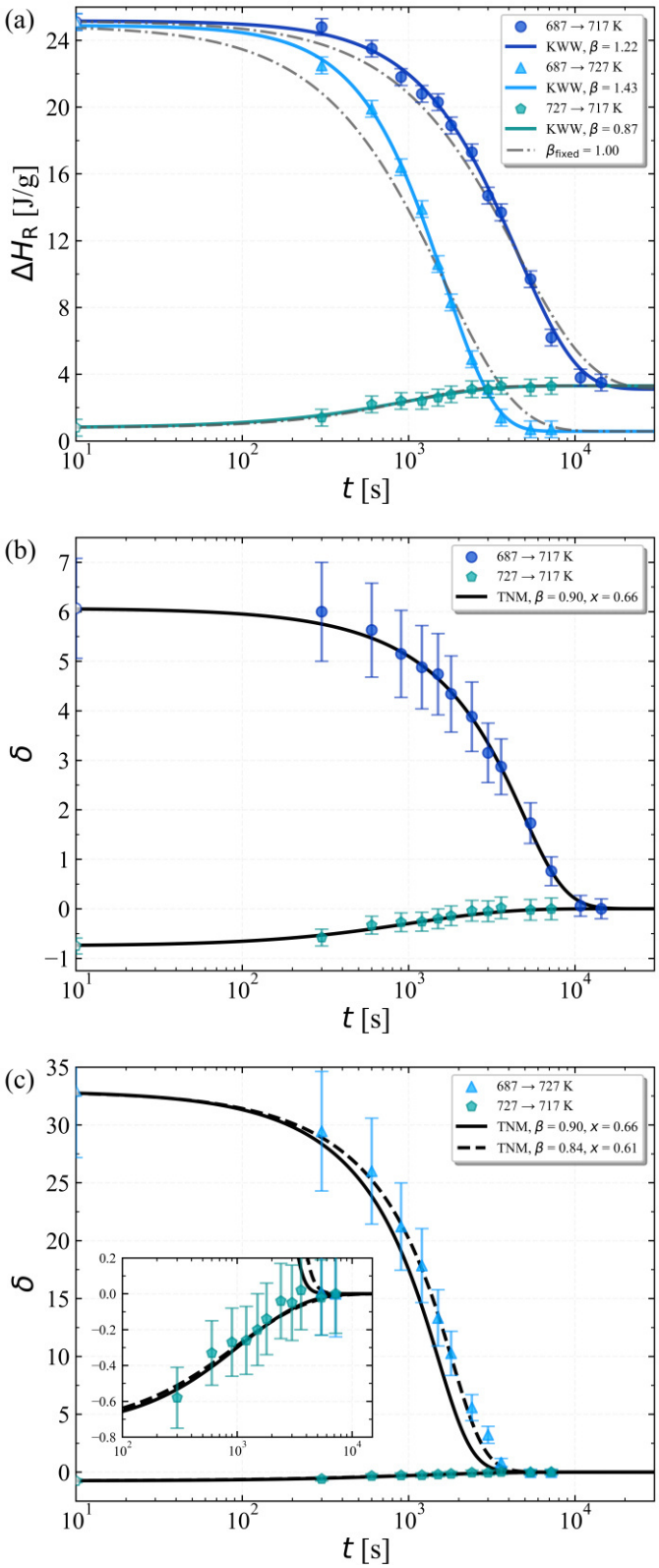

Figure 5.4: Enthalpy recovery relaxation data as a function of aging time for temperature up- and down-jumps. (a) Fits obtained using the KWW function, Eq. (2.7). Fits obtained using the TNM model via Eqs. (2.12), (5.3), and (5.4) for temperature jumps from

(b) 687 to 717 K and 727 to 717 K, and (c) 687 to 727 K and 727 to 717 K. Inset in Figure (c) shows a zoomed-in view of the down-jump data.

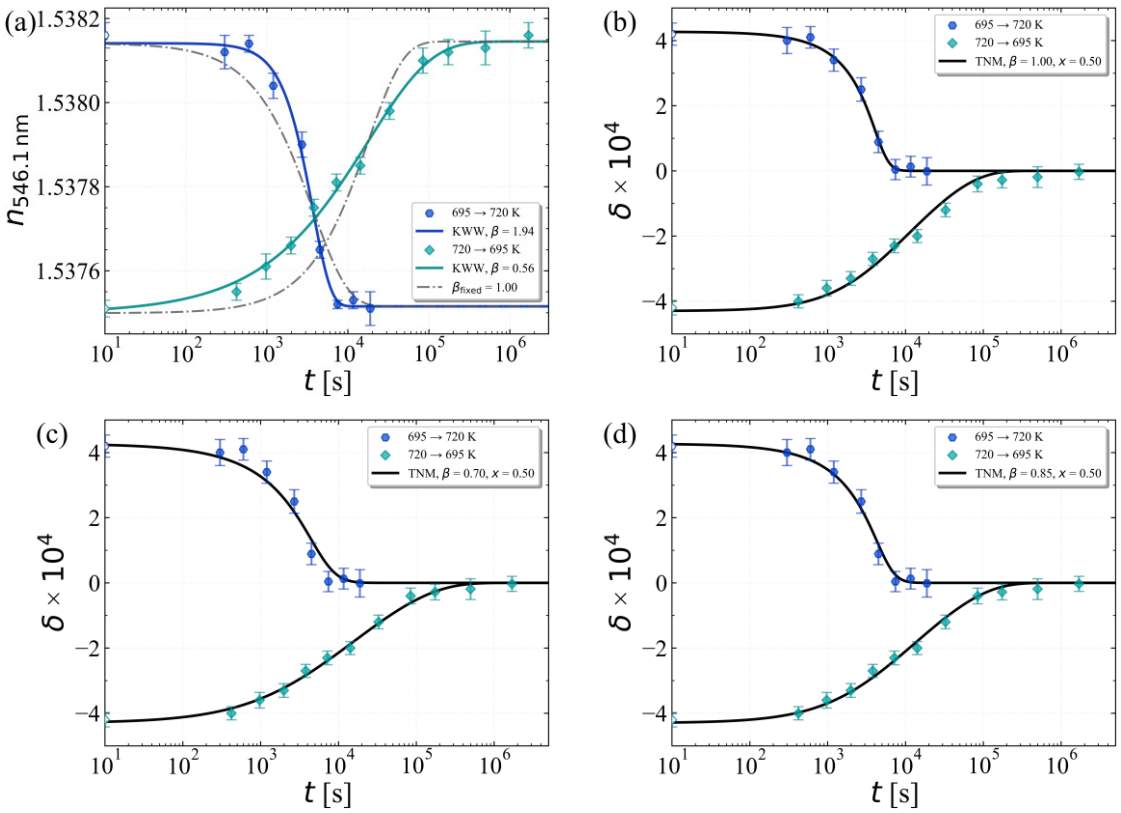

Figure 5.5: Refractive index relaxation data of sample II as a function of aging time for down-jump from 720 K to 695 K and up-jump from 695 K to 720 K. (a) Best fit curves obtained using the KWW function, Eq. (2.7). Fitting curves using the TNM model (Eqs. (2.12), (5.3), and (5.4)) with x = 0.50 and (b) β_{TNM} = 1.00 describing the up-jump data; (c) β_{TNM} = 0.70 describing the down-jump data; (d) β_{TNM} = 0.85, which describe both datasets approximately, within the measurement uncertainties.

Since the goal of this chapter was to test the validity of the TNM model for the relaxation kinetics of two different properties, efforts were made to optimize the changes in these properties to achieve the best possible experimental precision in enthalpy and refractive index measurements. As a result, different temperature jumps T_0 and T were used (**Tables 5.2** and **5.3**), which makes direct comparison of the relaxation kinetics for both properties difficult. However, the fitting parameters of the TNM model β_{TNM} and x are similar for the relaxation of these two properties over a similar temperature range, and good fits to the data could be obtained by keeping A fixed and a similar Δh^* for all cases (**Table 5.3**). Since the refractive index can be considered a reliable proxy for the sample

density or volume, the observed similarity between the TNM parameters (**Table 5.3**) corresponding to the relaxation of the index and enthalpy of the $Li_2Si_2O_5$ glass does suggest that the physical processes responsible for enthalpy and volume relaxation are likely the same. The TNM model has proved capable of fitting both up- and down-jump datasets with $\beta \leq 1$ via introduction of the non-linearity parameter x, although it becomes progressively challenging, especially for large temperature jumps. Previous studies have also reported a similar failure of this model under these circumstances [67,147–150]. This result may be indicative of the fact that the TNM model, in its current form, does not include any temperature dependence of β and x, which needs to be accounted for in case of substantial changes in T_f associated with large temperature jumps.

Physically, the compressed relaxation observed in the temperature up-jump data can be explained by considering the spatiotemporal evolution of the free volume in the structure at a given aging temperature. The structural relaxation induced rearrangement, which controls the physical aging, is a function of the thermodynamic state of the glass. When a glass is subjected to a temperature up-jump, its structure evolves from a smaller to a larger specific volume with aging time. In this case, a possible hypothesis is that the initial denser packing of atoms on average starts the relaxation process via nucleation events of mobile centers where the packing is less dense, i.e., the free volume is larger than average. This process results in an initially long relaxation time and slow evolution of the properties, including T_f. Eventually, these mobile centers grow in size and coalesce or percolate, leading to a rapid drop in relaxation time associated with a self-accelerated behavior characterized by an avalanche-like dynamics and compressed exponential relaxation kinetics [144]. This nucleation and growth process was recently observed in molecular dynamics simulations of temperature up-jump experiments for the transformation of an ultrastable glass into a liquid [155]. Additionally, experimental evidence of nucleation and growth of supercooled liquid-like regions during temperature up-jump of other glasses to $T > T_g$ has been reported in the literature [156–158]. It is worth noting here that the compressed exponential behavior is a characteristic of the Johnson-Mehl-Avrami model of transformation kinetics based on nucleation, growth, and coalescence [159,160]. In contrast, in the case of a temperature down-jump, the glass structure evolves from a larger to a smaller specific volume. This reverse process does not require any nucleation event of mobile regions, as the larger initial free volume favors

atom mobility, causing a rapid evolution of the properties at the beginning of the aging process. Then, as the denser regions percolate over time, it produces a self-retardation of the aging process with a stretched exponential behavior [146]. This difference in the relaxation kinetics during temperature up- and down-jumps and in the associated evolution of the T_f of a glass is captured phenomenologically by the non-linearity parameter x and the non-exponentiality parameter β of the primary or α-relaxation in the TNM model. However, it may be noted that as an alternative explanation for the compressed relaxation observed in the temperature up-jumps, as well as to account for the failure of the TNM model, the possible involvement of mechanisms distinct from those corresponding to the α-relaxation has also been discussed in the literature [149,150,161].

5.4 Conclusions

An analysis of the structural relaxation process using the KWW function revealed distinct kinetic behaviors for temperature up- and down-jumps, associated with the non-linearity of glassy relaxation. The down-jump data exhibit a stretched exponential behavior ($\beta < 1$), whereas the up-jump data display a compressed exponential behavior ($\beta > 1$). The non-exponentiality of the kinetics increases with increasing the magnitude of the temperature jump. However, both up- and down-jump datasets could be fitted simultaneously using the TNM model with a single set of A, Δh^*, $\beta \leq 1$, and $x < 1$, especially when the temperature jump is relatively small, resulting in a comprehensive mathematical description of the relaxation process. However, as the magnitude of the temperature jump increases, the TNM model fails to accurately fit both datasets exhibiting compressed and stretched behaviors. This failure likely arises from the TNM model's treatment of β and x as temperature-independent variables in a phenomenological manner. This approximation is probably inadequate for large temperature jumps, when the T_f of the glass varies significantly during the relaxation process.

CHAPTER 6 – ATOMISTIC ORIGIN OF STRUCTURAL RELAXATION

6.1 Introduction

The structural mechanism of the aging-induced relaxation process has been a subject of great interest. One of the pioneering studies in understanding the atomic-scale structural rearrangements involved in the relaxation of glass was carried out on silicate glasses by Brandriss and Stebbins [162] using ^{29}Si nuclear magnetic resonance (NMR) spectroscopy. These authors investigated the Q^n speciation as a function of T_f in alkali and alkaline earth silicate glasses quenched at different cooling rates. Their findings suggested that the Si-O network relaxed through Q-species disproportionation reaction of the type:

$$Q^{n-1} + Q^{n+1} \rightleftharpoons 2Q^n, \tag{6.1}$$

which shifted to the right with decreasing T_f as the cooling rate decreased. This behavior was supported by molecular dynamics (MD) simulations performed by Li et al. [163] on a series of sodium silicate glasses with different T_f obtained by quenching them at different cooling rates. The results of that study indicate that while the short-range order structure, such as bond length, coordination number, and angles, remains unaffected by the cooling rate, intermediate-range structural features like the Q^n distribution exhibit a greater dependency. Song et al. [164] also studied the effect of the cooling rate on the silicate ring structure of a sodium silicate glass through MD simulations. These authors found that smaller silicate rings, those with fewer than six members, were unstable and decreased with decreasing the cooling rate. They concluded that the structural relaxation in these glasses occurred through the transformation of small rings into larger ones.

It is noteworthy that T_f can be modified not only by changing the cooling rate of the SCL but also within the glassy state through isothermal aging, although the associated relaxation processes may not be necessarily identical. This issue has been investigated in previous studies, particularly in borosilicate glasses and liquids using high-resolution ^{11}B NMR spectroscopy [165–169]. These studies showed that the changes in T_f whether due to variations in cooling rate or physical aging, led to similar changes in boron speciation, specifically in the conversion between BO_4 and BO_3 units. Raman spectroscopic studies have similarly demonstrated that structural relaxation, whether in response to T_f changes due to physical aging in germanium selenide glasses or

temperature changes in the corresponding supercooled liquids, is closely associated with the conversion between corner- and edge-shared $GeSe_4$ tetrahedra [58,95,170]. Recent studies by Jurca et al. [171] and Hamada et al. [54], using Raman spectroscopy, suggested that physical aging in soda-lime-silica glasses, similar to quench rate variation, also resulted in a shift of the disproportionation reaction (Eq. (6.1)) to the right with decreasing T_f. Finally, Bradtmüller et al. [135], employing ^{7}Li NMR spectroscopy observed significant changes in the spatial distribution of lithium ions in lithium disilicate glass due to physical aging. However, these authors noted no change in the Q^n distribution after aging over a narrow temperature range within 20 K of T_g.

Although these previous studies have made significant progress in developing a fundamental atomistic understanding of structural relaxation in glasses with highly connected networks, results on networks with a lower degree of connectivity (e.g., two or more non-bridging oxygens (NBO) per Si atom in silicates) remain missing in the literature. Moreover, a robust experimental description of the structural mechanism for relaxation should ideally be consistent across different structural characterization techniques.

In this chapter, the objective is to investigate the Q^n speciation and rearrangements during structural relaxation in lithium disilicate ($Li_2Si_2O_5$, NBO/Si = 1.0) and lead metasilicate ($PbSiO_3$, NBO/Si = 2.0) glasses, which have significantly different Q^n distributions [32,135], using a combination of Raman and NMR spectroscopy.

6.2 Materials and Methods

The $Li_2Si_2O_5$ and $PbSiO_3$ glasses used in this chapter are from the same batches used in the previous chapters and described in Chapter 3. The resulting glasses from the melt-quenching method are termed "as-quenched" in the subsequent discussions to indicate their thermal history. The T_g of these glasses was determined during the reheating process using a Mettler Toledo DSC1. Samples of ~10 mg were placed in hermetically sealed Al pans and heated at a rate of 10 K/min under a nitrogen atmosphere to 50 K above the glass transition region to erase any thermal history. The samples were then cooled in the calorimeter at a 10 K/min rate to 473 K and subsequently reheated at the same rate. The T_g onset values obtained during the reheating process were (730 ± 2) K for $Li_2Si_2O_5$ and (684 ± 2) K for $PbSiO_3$.

A portion of the as-quenched glasses was aged in a vertical furnace at 673 K ($T_g - T$ = 57 K; T_g/T = 1.085) for 30 days for $Li_2Si_2O_5$, and at 643 K ($T_g - T$ = 41 K; T_g/T = 1.064) for 37 days for $PbSiO_3$. After the heat treatments, the samples were removed from the furnace and allowed to cool to room temperature before their properties were measured. These samples are referred to as "aged" in the subsequent discussions. The temperatures and periods were chosen to maximize changes in the T_f of these glasses compared with that of their as-quenched counterparts within a reasonable time period, considering the physical aging curves previously obtained for the same compositions [64,151].

The degree of relaxation following the physical aging of $Li_2Si_2O_5$ and $PbSiO_3$ glasses was determined through measurements of density, enthalpy recovery, and refractive index. The density and enthalpy recovery of the as-quenched glass upon aging were measured using gas pycnometry and DSC, respectively; while the accompanying structural changes were probed using Raman and ^{29}Si MAS NMR spectroscopy. The refractive index measurements require cutting and polishing the samples to specific geometries, and the as-quenched glass was not amenable to such sample preparation procedure because of the presence of a significant amount of residual stress from quenching. Therefore, a portion of the as-quenched $Li_2Si_2O_5$ glass was annealed at 673 K for 3 h (below T_g since the highest crystal nucleation rates in the $Li_2Si_2O_5$ glass occur at temperatures close to T_g [172]), and a portion of the as-quenched $PbSiO_3$ glass was annealed near T_g, at 683 K, for 4 h to relieve the thermal stress, followed by slow cooling to room temperature at 3 K/min. This annealing step enabled the cutting of samples for refractive index measurements, and these samples are termed "annealed" in the subsequent discussion.

Density measurements were carried out at room temperature on the as-quenched and aged samples using a gas displacement pycnometer (Micromeritics AccuPyc II 1340) under a helium environment of 6N purity. Approximately 1.0 g (m_s) of each sample was placed into a 1 cm^3 cup, and then 10 density readings were taken over 10 cycles of gas pumping and evacuation. The gas pycnometer comprises a sample chamber and an expansion chamber with calibrated volumes V_{cel} and V_{exp}, respectively. The AccuPyc determines the sample volume V_s using Eq. (6.2). The expansion chamber is filled to an elevated pressure P_1, while the sample chamber remains at ambient pressure. After P_1

stabilizes, a valve is opened, and the pressure falls to an intermediate value P_2. The sample density ρ is then be calculated according to Eq. (6.3),

$$V_s = V_{cel} - V_{exp}\left(\frac{P_1}{P_2} - 1\right), \tag{6.2}$$

$$\rho = \frac{m_s}{V_s}. \tag{6.3}$$

Enthalpy measurements were performed on the as-quenched, annealed, and aged samples using a similar procedure and equipment described in Chapter 5, in which the enthalpy recovery ΔH_R was determined from the difference in the area under the sample and rejuvenated heat flow curves, as given by Eq. (5.2).

Refractive index measurements were conducted on the annealed and aged samples using a similar procedure and equipment described in Chapter 4. The samples, approximately 10 × 10 × 2 mm^3 in size with two perpendicularly polished faces, were measured using a VoF5 prism ($n_{\lambda,p}$ = 1.74800(1) at the e-line) for the $Li_2Si_2O_5$ glass and a VeF4 prism ($n_{\lambda,p}$ = 1.93493(1) at the e-line) for the $PbSiO_3$ glass. Only one sample was used for each glass composition, as maintaining the same sample geometry is important to achieve the highest accuracy in index measurements. Following the splat-quenching and annealing processes, the refractive indices of the glasses were initially measured. Subsequently, the samples underwent aging before the final refractive index measurements were conducted.

Unpolarized Raman spectra of both as-quenched and aged $Li_2Si_2O_5$ and $PbSiO_3$ glasses were acquired at room temperature using a Fourier-transform Raman spectrometer (Bruker RFS 100/S) equipped with a Nd:YAG laser operating at a wavelength of 1,064 nm, and a liquid nitrogen cooled solid-state Ge detector. Spectra were collected in the high-frequency region of 700–1,300 cm^{-1}, employing a resolution of 2 cm^{-1} and a laser power level of 400 mW. Each spectrum was an average of 4,000 scans, with an acquisition time of approximately 2 h. The Raman spectral line shapes were fitted with Gaussian peaks using the Fityk software [173].

The ^{29}Si magic angle spinning (MAS) NMR spectra were acquired at room temperature for the as-quenched and aged $Li_2Si_2O_5$ and $PbSiO_3$ glasses using a Bruker Avance 500 MHz spectrometer operating at a Larmor frequency of 99.3 MHz (11.74 T)

for ^{29}Si and utilizes a 7 mm Bruker CPMAS probe. The crushed glass samples were placed in ZrO_2 rotors and spun at 7 kHz for $Li_2Si_2O_5$ and 5 kHz for $PbSiO_3$. All spectra were acquired with a $\pi/3$ pulse (pulse length of 2.3 to 2.7 μs) and a recycle delay of 60 s. To obtain each spectrum, approximately 500–1,500 transients were averaged and Fourier transformed. The Q^n distributions were determined by simulating the spectral line shapes using the DMFit software [174].

6.3 Results and Discussion

The density ρ of $Li_2Si_2O_5$ and $PbSiO_3$ glasses increased after aging, changing from an initial value of (2.337 ± 0.002) g/cm^3 to (2.352 ± 0.001) g/cm^3 for $Li_2Si_2O_5$ and from (5.931 ± 0.003) g/cm^3 to (5.983 ± 0.007) g/cm^3 for $PbSiO_3$ (**Figure 6.1**).

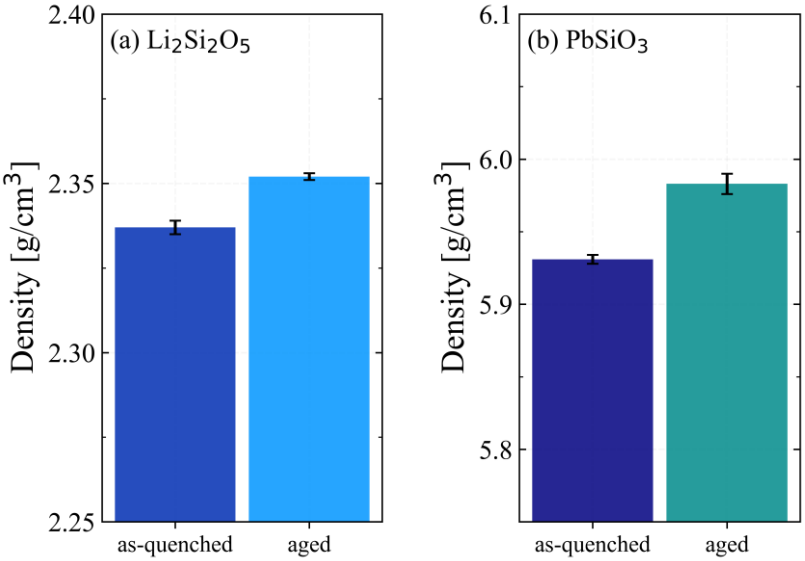

Figure 6.1: Experimental density relaxation data of (a) $Li_2Si_2O_5$ and (b) $PbSiO_3$ glasses for as-quenched and aged samples.

The evolution of the enthalpy recovery is shown in **Figure 6.2**. As expected, aging led to a larger endothermic overshoot peak near T_g. The endothermic peak was very small for the as-quenched samples and became sharper and more resolved for the aged samples. The annealed samples showed behavior similar to the rejuvenated samples obtained from a second heating after cooling at 10 K/min. Therefore, the enthalpy recovery for the as-quenched samples was negative, indicating overshoots lower than those in the rejuvenated samples. This finding agrees with the data of Claudy et al. [175], who utilized an initial glass sample quenched in liquid nitrogen. The annealed samples showed practically zero

recovery, indicating a small change in T_f upon annealing compared to the rejuvenated samples. The aged samples exhibited pronounced recovery, which is in good agreement with literature data [60,176], indicating effective relaxation at the utilized aging temperatures and times.

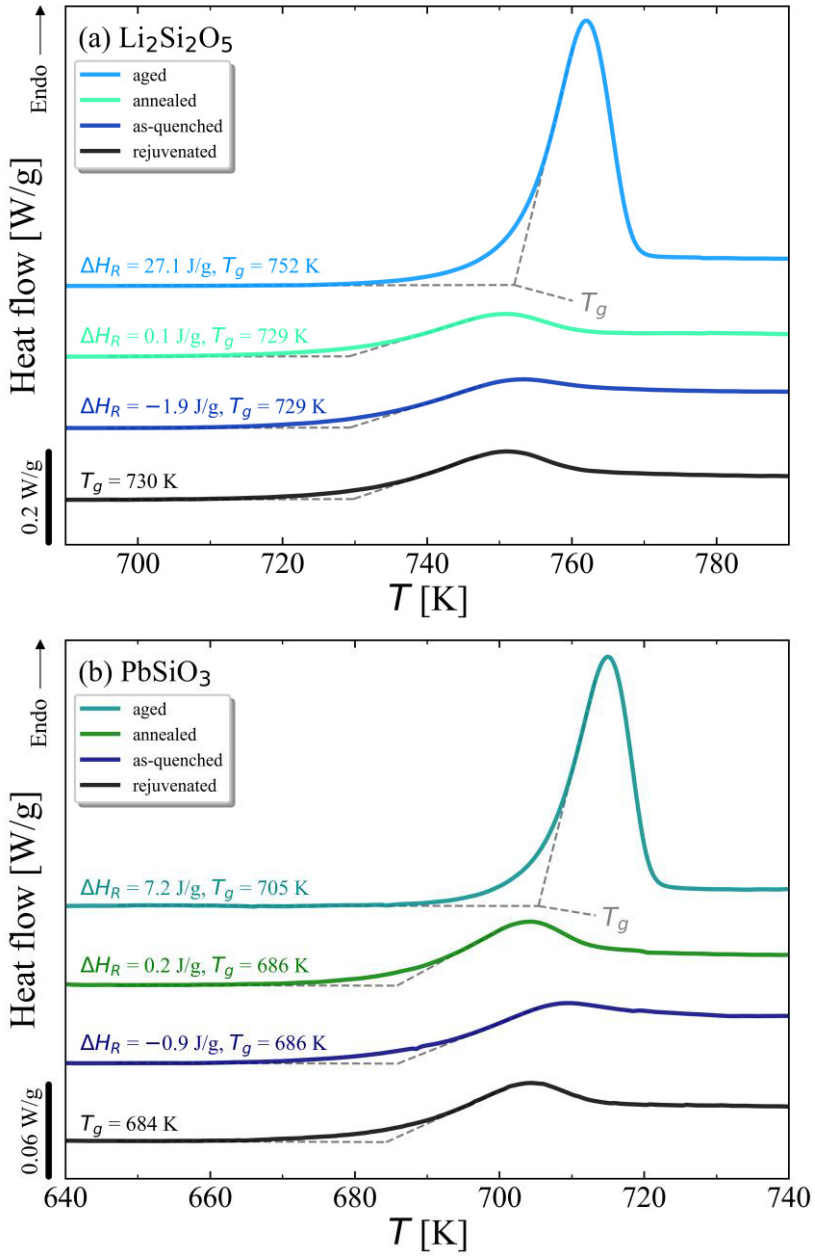

Figure 6.2: Experimental enthalpy recovery data of (a) $Li_2Si_2O_5$ and (b) $PbSiO_3$ glasses for aged, annealed, as-quenched, and rejuvenated (second heating after cooling at 10 K/min) samples.

Figure 6.2 also shows that the onset T_g increases in the first heating after temperature down-jumps, with a 23 K increase for $Li_2Si_2O_5$ and 19 K for $PbSiO_3$. This

reinforces the need for the protocol to report the T_g on the second heating, after erasing the thermal history using a standardized cooling and heating rate (10 K/min), when comparing T_g values between different batches or glasses.

The magnitude of increase in the refractive index of the aged samples compared with that of their annealed counterparts is shown in **Figure 6.3**. This figure also shows the refractive index relaxation data from previous studies on the physical aging of $Li_2Si_2O_5$ [151] and $PbSiO_3$ [64] glasses. It is clear that the most significant change in refractive index occurred in the samples prepared in this chapter, aged at the lowest temperatures. It may be noted that the annealed samples exhibited a recovery of 2.0 J/g for $Li_2Si_2O_5$ and 1.1 J/g for $PbSiO_3$ in enthalpy when compared to their as-quenched counterparts. These values correspond to 7% for $Li_2Si_2O_5$ and 15% for $PbSiO_3$ of the enthalpy recovery for the aged samples. Therefore, it is clear that the variation in refractive index would have been greater if it had been possible to use the as-quenched samples instead of the previously annealed ones for index measurements. However, the measurements of density, enthalpy recovery, and refractive index were conducted to confirm significant property variations following the physical aging treatments, thereby qualifying the aged samples for structural analyses using Raman and NMR spectroscopy.

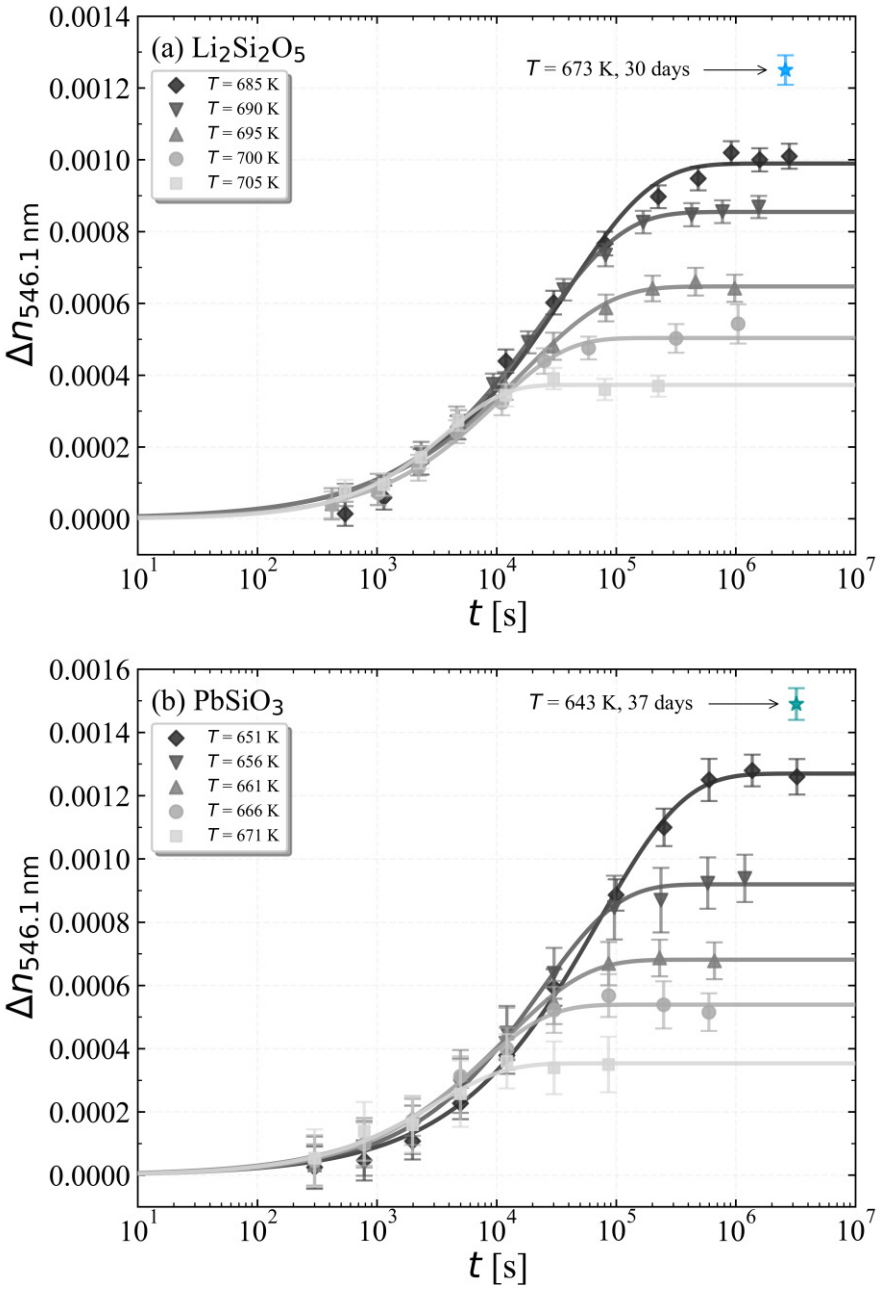

Figure 6.3: Change in refractive index (indicated by a star) of aged (a) $Li_2Si_2O_5$ and (b) $PbSiO_3$ glasses, compared with that of their annealed counterparts. Other symbols correspond to previously reported refractive index relaxation data for these glass compositions at higher aging temperatures [64,151].

The Raman spectra of the as-quenched and aged $Li_2Si_2O_5$ glass samples in the high-frequency region are presented in **Figure 6.4**. These spectra display two well-resolved peaks near 950 and 1,080 cm^{-1} and clearly indicate a significant increase in the relative intensity of the latter band in the aged sample. The high-frequency bands in these spectra correspond to symmetric Si-O stretching vibrations of the various Q^n units in these

glasses [177,178]. Following the approach of previous studies, these two spectral line shapes were fitted with four Gaussian bands at approximately 950, 1,020, 1,080 and 1,130 cm^{-1} to qualitatively assess the variation of the relative fractions of these units induced by physical aging [177,179–183]. The position and width of these Gaussian bands were allowed to vary within a rather narrow-range between the two sample fits, and the resulting parameters for each band are listed in **Table 6.1**.

The Raman bands at ~950, 1,080, and 1,130 cm^{-1} in silicate glasses can be readily assigned to Q^2, Q^3, and Q^4 units, respectively, based on systematic studies in the literature [177,182,183]. In contrast, the assignment of the 1,020 cm^{-1} band remains somewhat controversial [180]. This band occurs in the same region as in fully polymerized silica glass with Q^4 units, leading some authors to attribute it to these units [54,181,184]. However, a band in this region was observed by Mysen et al. [179] in the Raman spectra of glasses with low SiO_2 content, where Q^4 units are unlikely to be present. Other studies, in line with the observation made by Mysen et al., attributed this band to $Q^{3\prime}$ species [183,185,186], which are Q^3 species bonded to Q^2 tetrahedra. This $Q^{3\prime}$ species is considered structurally and vibrationally distinct from the Q^3 species that are solely connected to Q^3 in Q^3-rich clusters, characterized by the 1,080 cm^{-1} band.

The aging-induced variation in the relative areas under these Raman bands (**Table 6.1**), based on the aforementioned Q-species assignments, is consistent with the disproportionation reaction of Eq. (6.1). After aging, there is an increase in the ($Q^{3\prime} + Q^3$) area from 68.1 to 70.5% and a corresponding decrease in the ($Q^2 + Q^4$) area from 31.9 to 29.5%. Notably, the Q^3:$Q^{3\prime}$ band area ratio also increases upon aging from 1.87 to 1.90, suggesting an enlargement in the size of Q^3 clusters in the glass structure.

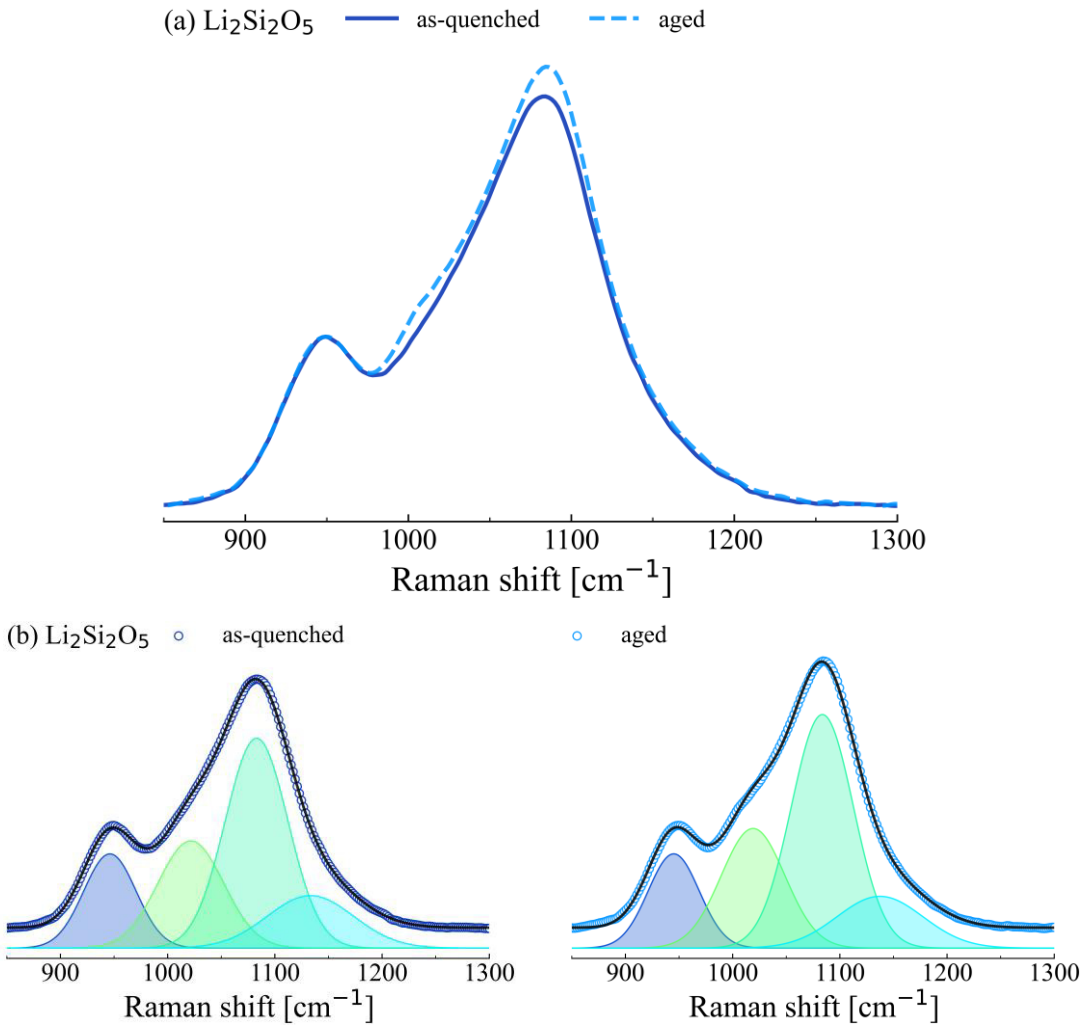

Figure 6.4: (a) High-frequency Raman spectra of as-quenched (solid line) and aged (dashed line) $Li_2Si_2O_5$ glass samples normalized to the intensity of the band at ~950 cm^{-1}. (b) Simulation (solid black lines) of experimental (circles) spectra with Gaussian bands attributed from left to right to Q^2, $Q^{3´}$, Q^3, and Q^4 units, respectively.

Table 6.1: Fitting parameters including peak position, full-width at half-maximum (FWHM), and relative area fraction of Gaussian peaks, used for simulating the Raman spectra of as-quenched and aged $Li_2Si_2O_5$ glass samples.

Sample	Frequency (cm^{-1})	FWHM (cm^{-1})	Area (%)	Q^n
$Li_2Si_2O_5$	946.2	57.5	16.6	Q^2
as-quenched	1,021.7	72.3	23.7	$Q^{3´}$
	1,083.0	69.0	44.4	Q^3
	1,133.3	95.2	15.3	Q^4
$Li_2Si_2O_5$	945.1	56.1	15.3	Q^2
aged	1,019.1	70.0	24.3	$Q^{3´}$
	1,083.7	68.2	46.2	Q^3
	1,137.5	94.5	14.2	Q^4

The evolution of the ^{29}Si MAS NMR spectra for the as-quenched and aged samples of $Li_2Si_2O_5$ glass is shown in **Figure 6.5**. These spectra display a broad resonance centered at ~−90 ppm with two shoulders near −80 and −100 ppm. A detailed inspection of these spectra, normalized to the shoulder near −80 ppm, reveals a significant increase in the relative intensity of the resonance near −90 ppm in the aged sample. Consistent with methodologies from previous studies, the line shapes of these spectra were simulated using three Gaussian components. These components, centered at approximately −80, −90, and −104 ppm, correspond to the resonance of the Q^2, Q^3, and Q^4 units, respectively [187,188]. The simulation parameters are listed in **Table 6.2**. Consistent with the qualitative trend observed in the normalized experimental spectra (**Figure 6.5**(a)) and the Raman spectroscopic results discussed earlier, the simulations (**Figure 6.5**(b)) indicate a relative increase in the fraction of Q^3 species by ~1% and a corresponding decrease in Q^2 and Q^4 in $Li_2Si_2O_5$ glass upon aging.

These results represent a direct observation of aging-induced Q-species disproportionation in $Li_2Si_2O_5$ glass via ^{29}Si NMR, following the disproportionation reaction in Eq. (6.1) after isothermal aging. Bradtmüller et al. [135] also investigated structural changes in $Li_2Si_2O_5$ glass after physical aging experiments but did not detect significant changes in the ^{29}Si NMR spectra associated with structural relaxation. It is noteworthy that their study focused on glass relaxation only 20 K below T_g. Although the disproportionation of Q-species is expected to occur in a similar manner in their case, its extent is likely to be significantly smaller than that observed in this chapter, and thus potentially undetectable by ^{29}Si NMR because of the relatively small temperature jump employed by the authors. However, these authors and others observed changes in the spatial distribution of lithium ions in $Li_2Si_2O_5$ glass upon aging using ^{7}Li NMR spectroscopy and X-ray scattering measurements [135,189]. The current observation of aging-induced Q-species disproportionation agrees well with similar disproportionation in alkali and alkaline earth silicate glasses reported by Brandriss and Stebbins, where changes in T_f were induced by variations in the quench rate of the parent liquid [162]. Collectively, these results suggest that similar structural relaxation mechanisms operate in silicate networks in both glassy and SCL states.

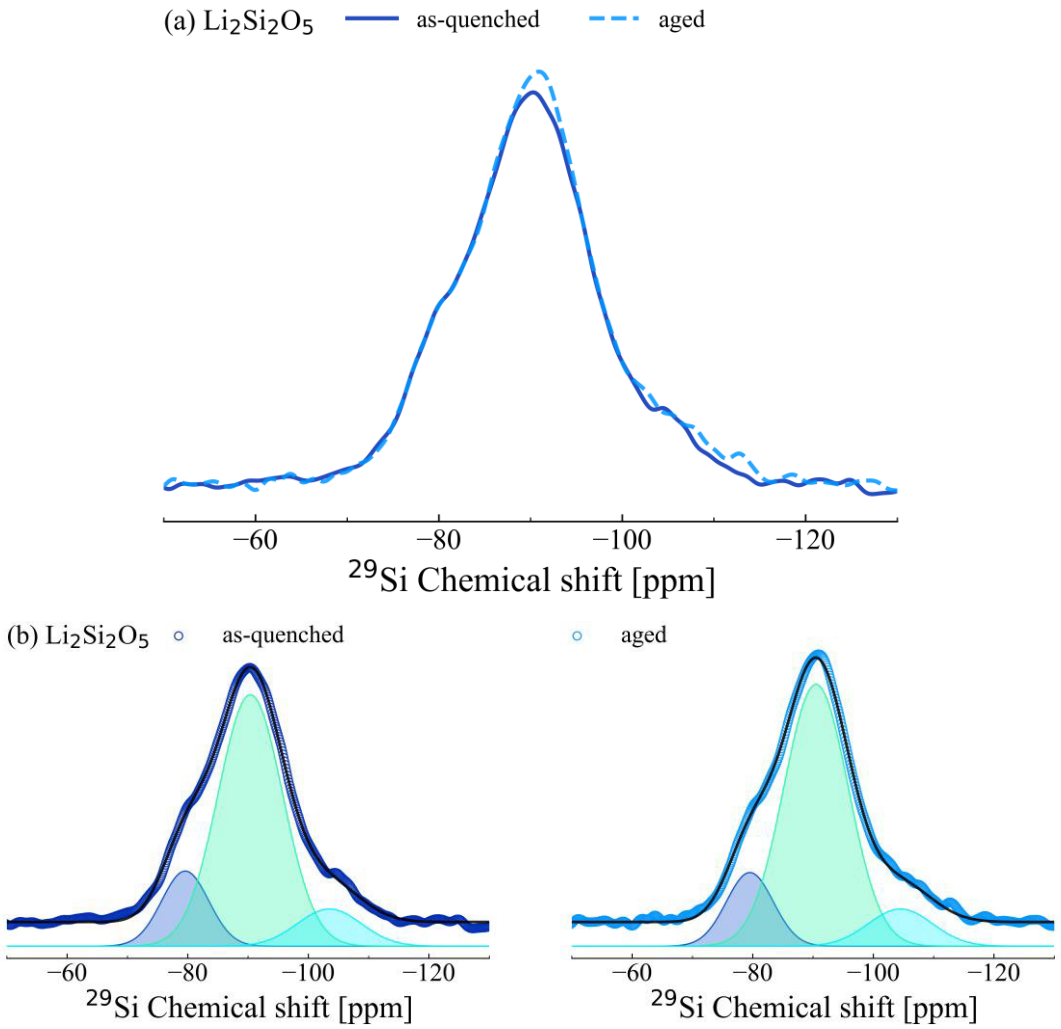

Figure 6.5: (a) ^{29}Si MAS NMR spectra of as-quenched (solid line) and aged (dashed line) $Li_2Si_2O_5$ glass samples normalized to the shoulder near −80 ppm. (b) Simulation (solid black lines) of experimental (circles) spectra with Gaussian bands attributed from left to right to Q^2, Q^3, and Q^4 units, respectively.

Table 6.2: Fitting parameters including isotropic chemical shift (δ), FWHM, and relative area fraction of the Gaussian peaks, used for simulating the ^{29}Si MAS NMR spectra of as-quenched and aged $Li_2Si_2O_5$ glass samples.

Sample	δ (ppm)	FWHM (ppm)	Area (%)	Q^n
$Li_2Si_2O_5$	−79.6	9.2	16.0	Q^2
as-quenched	−90.4	12.6	73.3	Q^3
	−103.5	12.5	10.8	Q^4
$Li_2Si_2O_5$	−79.5	9.1	15.2	Q^2
aged	−90.5	12.6	74.3	Q^3
	−104.5	12.5	10.5	Q^4

In contrast to disilicate glasses such as $Li_2Si_2O_5$, where the Q^3 species are predominant, metasilicate glasses like $PbSiO_3$ exhibit Q^2 as the main tetrahedral unit in their silicate network [190]. A detailed inspection of the Raman spectra of as-quenched and aged $PbSiO_3$ glasses (**Figure 6.6**(a)) reveals a clear increase in relative intensity in the region between 950 and 1,000 cm^{-1} after aging, indicating a corresponding change in Q speciation. Unlike alkali silicates, Pb-silicate glasses are typically characterized by a wider variety of Q-species, owing to an order-of-magnitude larger equilibrium constant for Q-speciation in the latter system [186,191]. The compositional evolution of the Raman spectra of glasses in the $PbO\text{-}SiO_2$ system has systematically been analyzed in previous studies [192,193]. Following these methodologies, the high-frequency envelope of the two Raman spectra in **Figure 6.6**(a) was simulated using six Gaussian bands located at approximately 850, 900, 955, 1,000, 1,045, and 1,100 cm^{-1}, corresponding to the stretching modes of Q^0, Q^1, Q^2, Q^3, $Q^{3\prime}$, and Q^4 species, respectively [32,194,195]. Again, the position and width of these Gaussian bands were allowed to vary within a rather narrow-range between the two sample fits, and the resulting parameters are presented in **Table 6.3**.

The results, as illustrated in **Figure 6.6**(b), show an increase in the relative area under the Q^2 band from 39.3% to 40.1% and a decrease in the Q^1 and (Q^3 + $Q^{3'}$) band areas from 26.0 to 25.3 and from 23.5 to 23.0, respectively (**Table 6.3**). This trend follows the disproportionation reaction outlined in Eq. (6.1). Similar to $Li_2Si_2O_5$, the Q^3:$Q^{3\prime}$ band area ratio in $PbSiO_3$ increases from 2.01 to 2.48 upon aging (**Table 6.3**). This finding agrees with the reduction in Q^3–Q^2 connectivity, possibly due to the increased spatial clustering length scale of Q^2 and Q^3 species in the aged $PbSiO_3$ glass, suggesting an enlargement of Q^3 clusters within the glass structure. While such small changes in the relative areas of the constituent bands needs to be interpreted with caution, it should be emphasized that the normalized Raman spectra in **Figure 6.6**(a) display clear differences between the as-quenched and the aged samples, as previously mentioned.

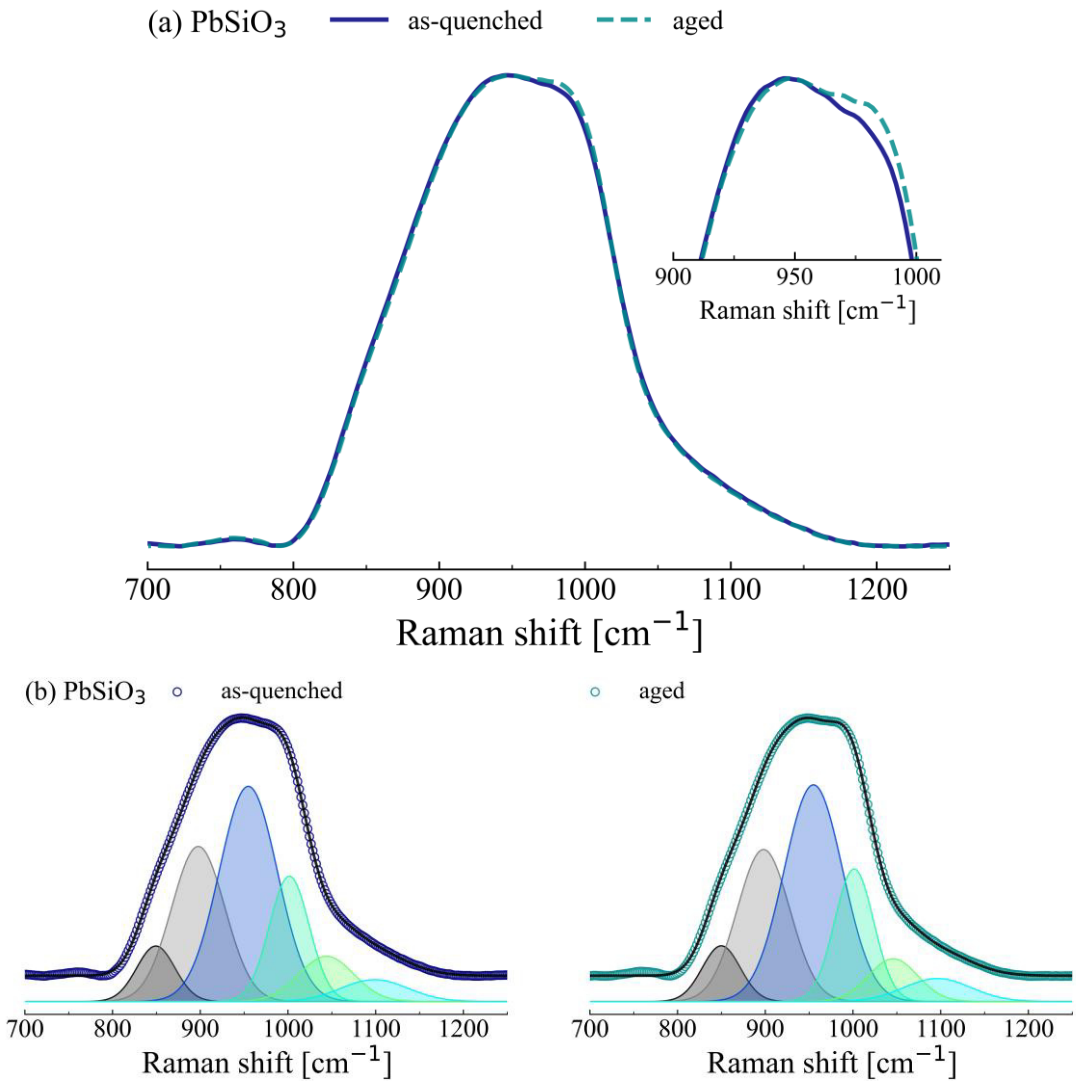

Figure 6.6: (a) High-frequency Raman spectra of as-quenched (solid line) and aged (dashed line) $PbSiO_3$ glass samples normalized to the maximum intensity. Inset shows a magnified view of the peak region. (b) Simulation (solid black lines) of experimental (circles) with Gaussian bands attributed from left to right to Q^0, Q^1, Q^2, Q^3, $Q^{3´}$, and Q^4 units, respectively.

Table 6.3: Fitting parameters including peak position, FWHM, and relative area fraction of Gaussian peaks, used for simulating the Raman spectra of as-quenched and aged $PbSiO_3$ glass samples.

Sample	Frequency (cm^{-1})	FWHM (cm^{-1})	Area (%)	Q^n
$PbSiO_3$	849.4	51.4	6.7	Q^0
as-quenched	897.8	71.5	26.0	Q^1
	954.8	78.0	39.3	Q^2
	1,001.6	53.4	15.7	Q^3
	1,044.0	73.6	7.8	$Q^{3'}$
	1,098.7	90.1	4.6	Q^4
$PbSiO_3$	849.9	51.0	6.7	Q^0
aged	898.1	70.7	25.3	Q^1
	955.0	78.7	40.1	Q^2
	1,001.4	52.4	16.4	Q^3
	1,045.8	66.2	6.6	$Q^{3'}$
	1,096.4	90.4	4.9	Q^4

To corroborate the observations from the Raman spectra, ^{29}Si MAS NMR spectra of the as-quenched and aged samples were analyzed. These two NMR spectra show rather subtle differences in the line shape (**Figure 6.7**(a)). Following the approach of previous systematic ^{29}Si NMR spectroscopic studies of Pb-silicate glasses [191,196], these line shapes were simulated with five Gaussians, centered at approximately −70, −80, −87, −95, and −105 ppm, corresponding to Q^0, Q^1, Q^2, Q^3, and Q^4 units, respectively [196] (**Figure 6.7**(b)). A reliable quantitative analysis of the subtle aging-induced changes in the ^{29}Si MAS NMR spectra of $PbSiO_3$ proved to be challenging because of the presence of all possible Q^n units in this glass. Nevertheless, the spectral line shape simulations detailed in **Table 6.4** indicate a more complex Q-speciation than the qualitative trends suggested by the Raman spectroscopic results. Aging of $PbSiO_3$ glass seems to increase the relative fraction of Q^0 and Q^4 units, while those of Q^1 and Q^3 units decrease (**Figure 6.7**(a)). However, further ^{29}Si NMR studies are needed, potentially at higher magnetic fields and with isotopic enrichment, to achieve higher signal-to-noise to confirm these unique speciation results.

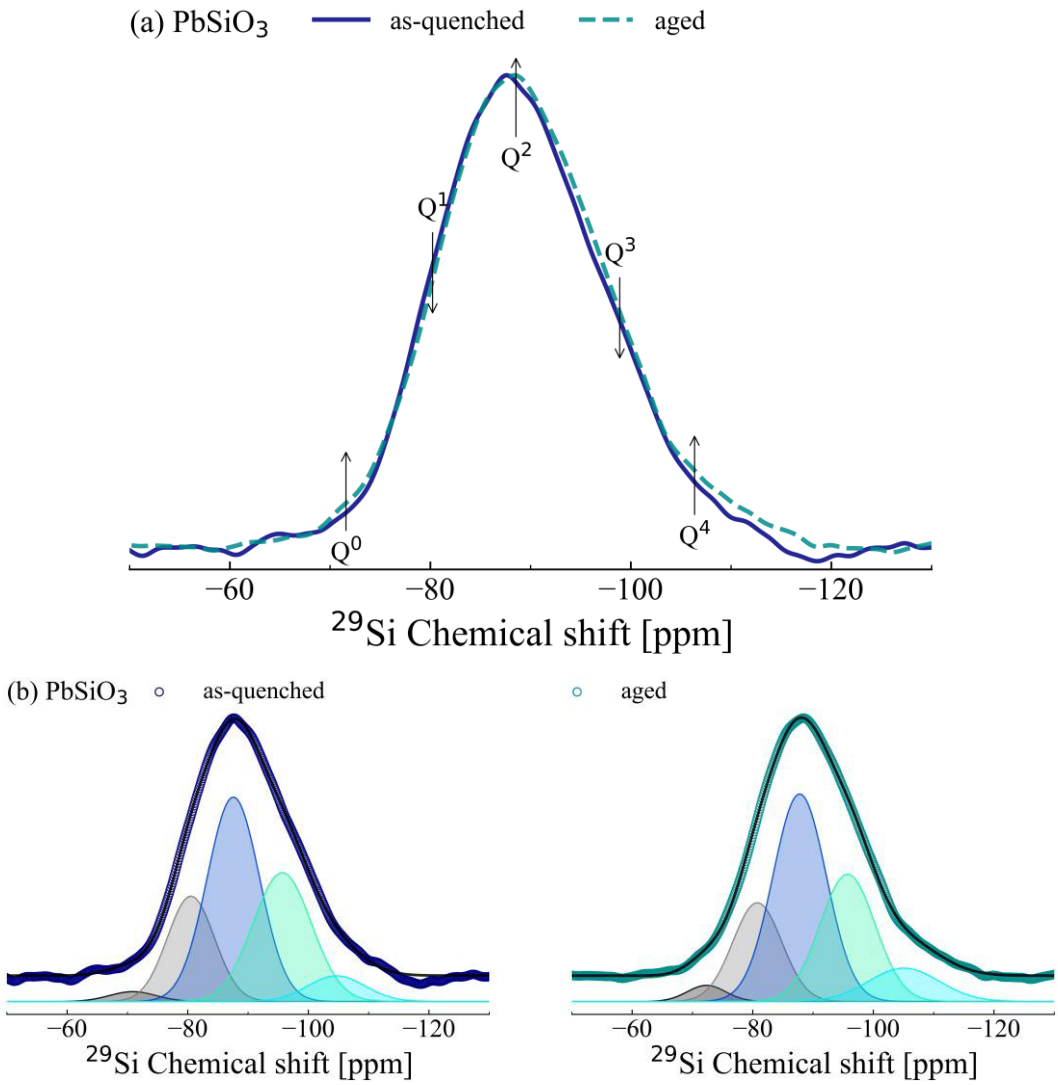

Figure 6.7: (a) ^{29}Si MAS NMR spectra of as-quenched (solid line) and aged (dashed line) $PbSiO_3$ glass samples normalized to the maximum intensity. Vertical arrows indicate changes in Q-species after aging. (b) Simulation (solid black lines) of experimental (circles) spectra with Gaussian bands attributed from left to right to Q^0, Q^1, Q^2, Q^3, and Q^4 units, respectively.

Table 6.4: Fitting parameters including δ, FWHM, and relative area fraction of the Gaussian peaks, used for simulating the ^{29}Si MAS NMR spectra of as-quenched and aged $PbSiO_3$ glass samples.

Sample	δ (ppm)	FWHM (ppm)	Area (%)	Q^n
$PbSiO_3$	−70.8	9.0	1.8	Q^0
as-quenched	−80.5	9.2	19.7	Q^1
	−87.5	10.2	42.7	Q^2
	−95.6	11.4	30.0	Q^3
	−104.6	11.2	5.8	Q^4
$PbSiO_3$	−72.3	7.5	2.4	Q^0
aged	−80.7	9.5	18.6	Q^1
	−87.7	10.4	42.8	Q^2
	−95.7	10.8	27.1	Q^3
	−105.0	13.8	9.1	Q^4

It may be noted that the total concentration of NBO is normally expected to remain constant during the aging process, unless free oxide ions (FO), solely bonded to the modifier cations, form via the transformation reaction: $2NBO \rightarrow BO + FO$. However, FO formation is rather unlikely in $Li_2Si_2O_5$ or $PbSiO_3$ glasses, which have relatively low modifier contents. Indeed, the NBO/Si ratio, calculated as $4Q^0+3Q^1+2Q^2+Q^3$ from the Q-speciation in as-quenched and aged $Li_2Si_2O_5$ and $PbSiO_3$ glasses (**Tables 6.2** and **6.4**), remains conserved during the aging-induced relaxation process, with values of ~1.05 and ~1.8, respectively. These values are close to the expected NBO/Si ratios of 1.0 for $Li_2Si_2O_5$ and 2.0 for $PbSiO_3$, based on nominal stoichiometry. The significantly lower NBO/Si value for the $PbSiO_3$ glass is likely related to some PbO loss due to its volatilization during glass melting. Additionally, Raman spectroscopic results suggest an increased degree of spatial clustering of the dominant Q-species in both glasses upon aging. It is tempting to hypothesize that these clusters may act as critical nuclei for the crystallization of phases such as $Li_2Si_2O_5$ in lithium disilicate glass, which contains only Q^3 species [197,198], and $PbSiO_3$ alamosite in lead metasilicate glass, which contains solely Q^2 species [199,200].

6.4 Conclusions

The aging-induced relaxation process in $Li_2Si_2O_5$ and $PbSiO_3$ glasses following a temperature down-jump leads to increases in density, enthalpy recovery, and refractive

index. A comparative analysis between the Raman and the ^{29}Si MAS NMR spectra of as-quenched and aged $Li_2Si_2O_5$ glass samples indicates that aging following a temperature down-jump results in the disproportionation reaction $Q^2 + Q^4 \rightleftharpoons 2Q^3$ shifting to the right. In contrast, $PbSiO_3$ glass exhibits a more complex Q-speciation, with the ^{29}Si MAS NMR spectra suggesting a significant increase in the relative fractions of Q^0 and Q^4 units, while those of Q^1 and Q^3 units decreased. Such Q-species disproportionation appears to result in increased clustering of the major Q-species.

CHAPTER 7 – EFFECT OF STRUCTURAL RELAXATION ON IONIC CONDUCTIVITY

7.1 Introduction

The conventional wisdom is that structural relaxation in oxide glasses and deeply supercooled liquids is controlled by bond switching or bond scission-renewal dynamics involving the bonds between the network-forming cations and oxygen (e.g., Si–O, B–O bonds) [166,168,171,201]. On the other hand, the dynamics of network-modifying cations, such as alkalis, is believed to be strongly decoupled from this process, as the hopping timescale of these ions, which is responsible for electrical conductivity, is typically orders of magnitude faster than the timescale of α-relaxation [33,68,202].

Ionic conduction in glasses is ascribed to the hopping of ions from one local energy minimum to another, leading to a long-range diffusive transport of modifier ions [203]. The DC conductivity is a function of ionic charge (q), mobility (μ) and concentration (n), expressed as $\sigma_{\mathrm{DC}} = nq\mu$. The experimental ionic conductivity is commonly described by a simplified Arrhenius equation:

$$\sigma_{\mathrm{DC}} = \sigma_0 \exp\left(-\frac{E_a'}{RT}\right), \tag{7.1}$$

where σ_0 is a pre-exponential factor and E_a' is the activation energy. This equation links the two experimental parameters, σ_{DC} and T, without any theory that addresses the issue of ionic conductivity [204]. However, the following equation is also frequently used:

$$\sigma_{\mathrm{DC}} T = A \exp\left(-\frac{E_a}{RT}\right), \tag{7.2}$$

where A is a pre-exponential term and E_a is the activation energy for ion conduction. This equation is a simplified version of the expression given below, which has been derived many times before [203–207], from the Nernst–Einstein relation, expressing a direct relationship between diffusion and conductivity,

$$\sigma_{\mathrm{DC}} = \frac{n(Ze)^2 \lambda^2 \omega_0}{6k_B T} \exp\left(-\frac{\Delta G_m}{RT}\right), \tag{7.3}$$

or, after separating the migrational enthalpic (ΔH_m) and entropic (ΔS_m) terms from the free energy of migration (ΔG_m),

$$\sigma_{\mathrm{DC}} = \frac{n(Ze)^2\lambda^2\omega_0}{6k_BT}\exp\left(\frac{\Delta S_m}{R}\right)\exp\left(-\frac{\Delta H_m}{RT}\right), \tag{7.4}$$

where n is the charge carrier concentration, Ze the charge of the ions, λ the hopping distance, ω_0 the attempt frequency, and k_B the Boltzmann constant. Thus, comparing Eqs. (7.2) and (7.4), $E_a = \Delta H_m$ and the pre-exponential term A can be expressed as,

$$A = \frac{n(Ze)^2\lambda^2\omega_0}{6k_B}\exp\left(\frac{\Delta S_m}{R}\right). \tag{7.5}$$

Recent studies have demonstrated significant effects of aging on the DC conductivity of glasses, which undergo α-relaxation in response to the evolution of the network structure during the relaxation process [69,208]. This observation is consistent with the findings in Chapter 4, which revealed that the timescale for conductivity relaxation was slightly faster than that for the volume relaxation measured via refractive index relaxation.

In this chapter, the objective is to elucidate the impact of α-relaxation on the fast modifier motion of different glass-forming systems with varying fragility indices by monitoring the migration enthalpy and entropy of ionic conduction after physical aging experiments.

7.2 Materials and Methods

Three glasses with compositions of $33.3Li_2O{\cdot}66.7SiO_2$ ($Li_2Si_2O_5$), $50.0Li_2O{\cdot}50.0P_2O_5$ ($LiPO_3$), and $37.5Na_2O{\cdot}12.5MgO{\cdot}50.0P_2O_5$ ($Na_{0.75}Mg_{0.125}PO_3$) (in mol%) were prepared by the conventional melt-quenching method. The $Li_2Si_2O_5$ glass used in this chapter is from the same batch described in Chapter 3. For the phosphate glasses, appropriate mixtures of reagent grade Li_2CO_3 (99.0%, Alfa Aesar), Na_2CO_3 (99.999%, Alfa Aesar), MgO (99.999%, Alfa Aesar), and orthophosphoric acid solution 85 wt% H_3PO_4 (Sigma Aldrich) were mixed. The mixtures were dried at 573 K for 2 days and calcinated at 823 K for 1 day to remove H_2O and CO_2. Then, the powders were subsequently melted in a platinum crucible in air at 1,273 K for 1 hour before being poured on a plate and splat-quenched by pressing with a steel block.

The calorimetric fragility index, m, of these glasses was determined using differential scanning calorimetry (DSC, Mettler Toledo DSC1) on samples of ~10 mg, placed in hermetically sealed Al pans and analyzed under a nitrogen atmosphere. The samples were heated at rates (q_h) of 5, 10, 15, 20, 25, and 30 K/min to 50 K above the glass transition region to erase any thermal history. Following this, the samples were cooled at the same rate (q_c) to 100 K below the glass transition, and finally reheated at the same rate. The m value was determined using the Eqs. (2.17) and (2.18), where the calorimetric T_f set during the cooling path was obtained upon reheating from the onset of the glass transition by matching the reheating rates to the cooling rates for each rejuvenation curve [46,52]. The estimated error in T_f is within ± 2 K. The standard T_g onset obtained through DSC corresponds to the T_f value measured during the reheating at a rate of 10 K/min after a prior cooling scan at the same rate [100]. For these measurements, the T_g onset values obtained were (728 ± 2) K for $Li_2Si_2O_5$, (600 ± 2) K for $LiPO_3$, and (612 ± 2) K for $Na_{0.75}Mg_{0.125}PO_3$.

Physical aging experiments were carried out using the temperature down-jump protocol. A portion of the as-quenched glasses was aged for 15 days in an electric furnace at 687 K ($T_g - T$ = 41 K; T_g/T = 1.060) for $Li_2Si_2O_5$, 582 K ($T_g - T$ = 18 K; T_g/T = 1.031) for $LiPO_3$, and 579 K ($T_g - T$ = 33 K; T_g/T = 1.057) for $Na_{0.75}Mg_{0.125}PO_3$. These temperatures and periods were chosen based on the results of a previous study on refractive index relaxation, which indicated that at 685 K the $Li_2Si_2O_5$ glass required 7 days to relax by 99% and 14 days to achieve practical equilibrium (99.9% relaxed) [151]. Then, to age $LiPO_3$ and for $Na_{0.75}Mg_{0.125}PO_3$ glasses for the same period of 15 days, the temperatures were chosen where the average relaxation times are similar based on their m values. The extent of the α-relaxation following the physical aging was determined by measuring changes in density, fictive temperature, and ionic conductivity between the as-quenched and aged samples.

The density measurements were carried out on the as-quenched and aged samples using a similar procedure and equipment described in Chapter 6, with approximately 0.5 g of each glass sample.

The T_f values of the as-quenched and aged samples were determined using the unified area-matching approach, as described by Eq. (2.3). The isobaric specific heat (c_p) given in $Jg^{-1}K^{-1}$ was measured under a nitrogen atmosphere using a DSC (Mettler Toledo

DSC1) and a sapphire standard (14.2 mg). Samples weighing ~10 mg were placed in hermetically sealed aluminum pans and were heated from 150 K below the glass transition region (T_a) to about 50 K above it (T_b) at a heating rate q_h of 10 K/min, producing a specific heat curve, c_{p1}. Following this scan, the samples were cooled to the same 150 K below the glass transition at a rate of 10 K/min, held for 5 min, and then reheated at the same rate to the same temperature 50 K above the glass transition to obtain the second specific heat curve, c_{p2}.

The angular frequency-dependent ionic conductivity $\sigma(\omega)$ of the samples was measured by EIS using a similar procedure and equipment described in Chapter 4. The measurements were conducted over a temperature range of 323 to 483 K for the phosphates and of 423 to 583 K for the silicate samples. The impedance data can be represented in several correlated formalisms from the real Z' and imaginary Z'' components of the impedance. The $\sigma(\omega)$ was computed using the values of the real $Z'(\omega)$ and imaginary $Z''(\omega)$ parts of the impedance obtained from EIS measurements and through the relation:

$$\sigma(\omega) = \frac{1}{\sqrt{Z'(\omega)^2 + Z''(\omega)^2}} \frac{l}{S} \tag{7.6}$$

where l and S denote the sample thickness and the electrode area, respectively. The l/S values were 0.607(1) cm^{-1} for $Li_2Si_2O_5$, 1.728(1) cm^{-1} for $LiPO_3$, and 0.326(1) cm^{-1} for $Na_{0.75}Mg_{0.125}PO_3$. The frequency independent conductivity (DC conductivity), σ_{DC}, was directly read on the frequency plateau of the $\sigma(\omega)$ curve, which is essentially identical to that calculated from the impedance complex plane plot of $-Z''$ vs. Z', as presented in Chapter 4.

7.3 Results and Discussion

The activation energy for enthalpy relaxation, E, and the calorimetric fragility index, m, for $Li_2Si_2O_5$, $Na_{0.75}Mg_{0.125}PO_3$, and $LiPO_3$ glasses are presented in **Figure 7.1**. The $LiPO_3$ is the most fragile of the analyzed compositions, with E of (970 ± 30) kJ/mol and m of 84 ± 2. The $Na_{0.75}Mg_{0.125}PO_3$ exhibited intermediate fragility, with E of (690 ± 10) kJ/mol and m of 59 ± 1. The relatively strong composition is $Li_2Si_2O_5$, with E of (600 ± 10) kJ/mol and m of 43 ± 1.

The density of these glasses increased after aging, while the corresponding molar volume decreased, as presented in **Table 7.1**. This result indicates that both silicate and phosphate tetrahedral networks were significantly more open prior to the structural reorganization induced by aging.

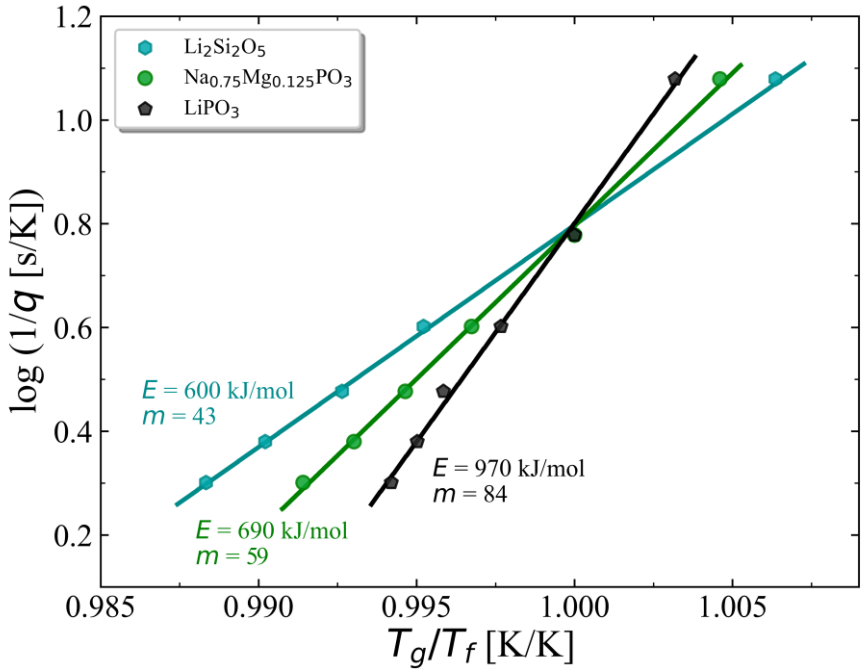

Figure 7.1: Reciprocal reheating rate as a function of T_g/T_f for $Li_2Si_2O_5$, $Na_{0.75}Mg_{0.125}PO_3$, and $LiPO_3$ glasses.

Table 7.1: Density and molar volume of as-quenched and aged glasses.

Sample	density [g/cm^3]	molar volume [cm^3/mol]
$Li_2Si_2O_5$, as-quenched	2.337 ± 0.002	21.41 ± 0.02
$Li_2Si_2O_5$, 15 days at 687 K	2.349 ± 0.002	21.30 ± 0.02
$LiPO_3$, as-quenched	2.343 ± 0.002	36.67 ± 0.03
$LiPO_3$, 15 days at 582 K	2.351 ± 0.002	36.54 ± 0.03
$Na_{0.75}Mg_{0.125}PO_3$, as-quenched	2.523 ± 0.002	39.34 ± 0.03
$Na_{0.75}Mg_{0.125}PO_3$, 15 days at 579 K	2.541 ± 0.002	39.06 ± 0.03

The fictive temperatures of the as-quenched and aged glasses, determined using the unified area-matching approach of Guo et al. [51], are shown in **Figure 7.2**. $LiPO_3$ and $Na_{0.75}Mg_{0.125}PO_3$ glasses, which were rapidly quenched, undergo structural relaxation during heating. This leads to broad exothermic enthalpy relaxation before the glass transition interval, as observed in **Figures 7.2**(c) and **7.2**(e), respectively. These glasses were splat-quenched into thin samples with thickness below 1 mm, while the $Li_2Si_2O_5$

glass was splat-quenched into a thicker sample of 3 mm, and thus does not exhibit an exothermic deviation before the glass transition interval, as seen in **Figure 7.2**(a).

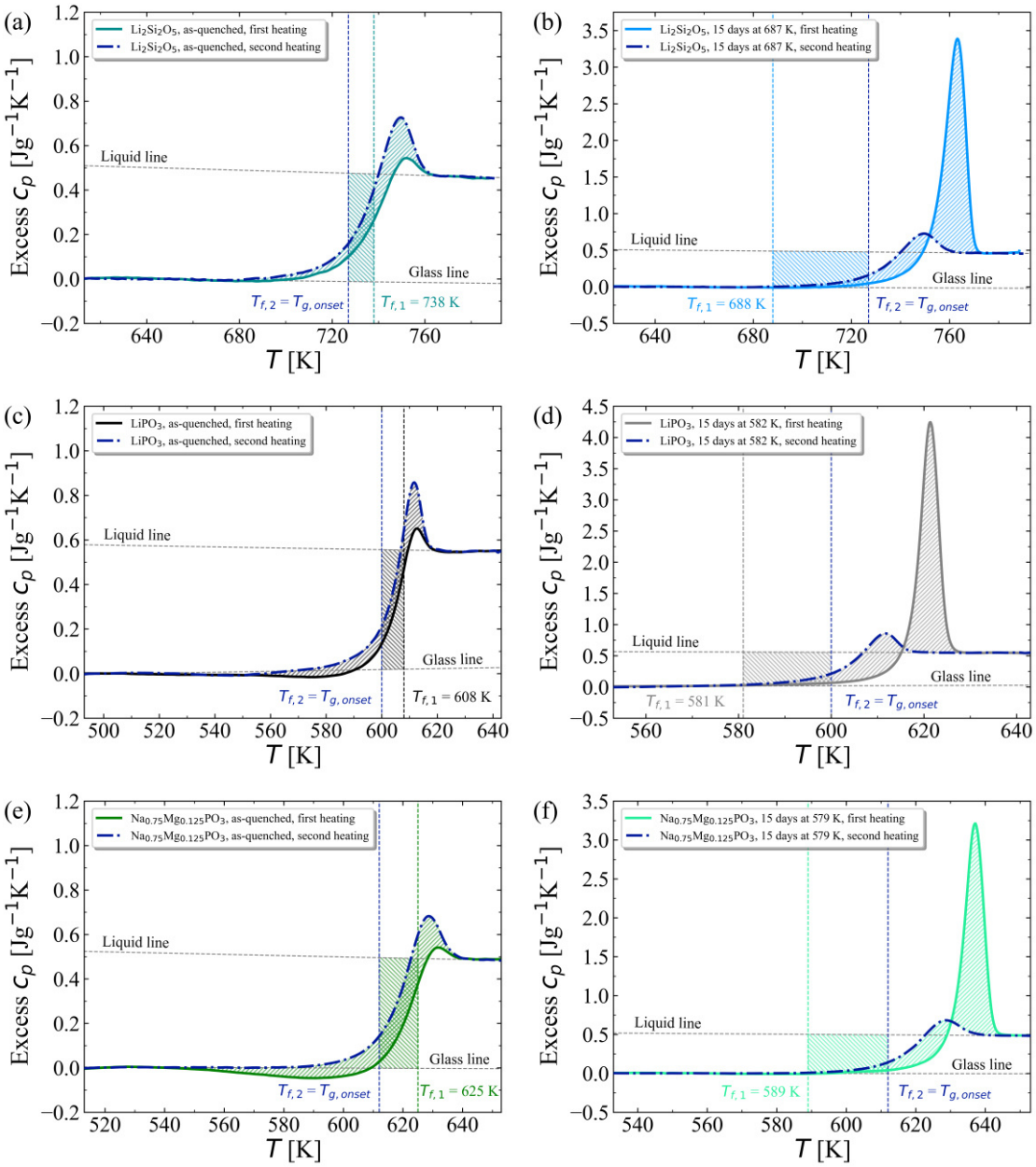

Figure 7.2: Isobaric specific heat curves used to determine experimental fictive temperature of different glasses: (a) $Li_2Si_2O_5$ as-quenched, (b) $Li_2Si_2O_5$ aged for 15 days at 687 K, (c) $LiPO_3$ as-quenched, (d) $LiPO_3$ aged for 15 days at 582 K, (e) $Na_{0.75}Mg_{0.125}PO_3$ as-quenched, and (f) $Na_{0.75}Mg_{0.125}PO_3$ aged for 15 days at 579 K.

As expected, the initial fictive temperature for all glasses was higher than the glass transition temperature. After the 15-day aging treatment, all samples exhibited a decrease in T_f toward the aging temperature, with a pronounced overshoot peak in the first heating

curve. The $Li_2Si_2O_5$ and $LiPO_3$ glasses reached the expected T_f, with the measured T_f matching the aging temperatures of 687 and 582 K, respectively. However, 15 days proved to be insufficient for the $Na_{0.75}Mg_{0.125}PO_3$ glass at 579 K, as the measured T_f was 589 K. This difference does not pose a problem for this study, as the aim is to investigate the effects of structural changes after aging, with sufficient variation in T_f for this purpose.

The temperature and frequency dependence of σ for the single-alkali $Li_2Si_2O_5$ and $LiPO_3$ glasses are shown in **Figure 7.3**. At each temperature, σ_{DC} was obtained from the frequency-independent region of $\sigma(\omega)$, as indicated by the arrows in **Figure 7.3**. It is clear from the data in **Figures 7.3** and **7.4** that at any given temperature the conductivity of the aged glass is lower than that of its quenched counterpart. The most fragile $LiPO_3$ glass exhibits a more significant decrease in conductivity, by a factor of 2.0, compared to the relatively strong $Li_2Si_2O_5$ glass, which decreases by a factor of 1.4 (**Figure 7.4**), despite the fact that the $LiPO_3$ glass was aged at $T_g - 18$ K, whereas $Li_2Si_2O_5$ was aged at $T_g - 41$ K.

As the charge carrier concentration of the mobile Li ions in $Li_2Si_2O_5$ and $LiPO_3$ glasses has only a negligible increase due to a decrease in molar volume after aging, the observed decrease in conductivity by a factor of 1.4 and 2.0 for $Li_2Si_2O_5$ and $LiPO_3$ glasses, respectively, in **Figure 7.3** can only be attributed to a reduction in μ due to structural reorganization.

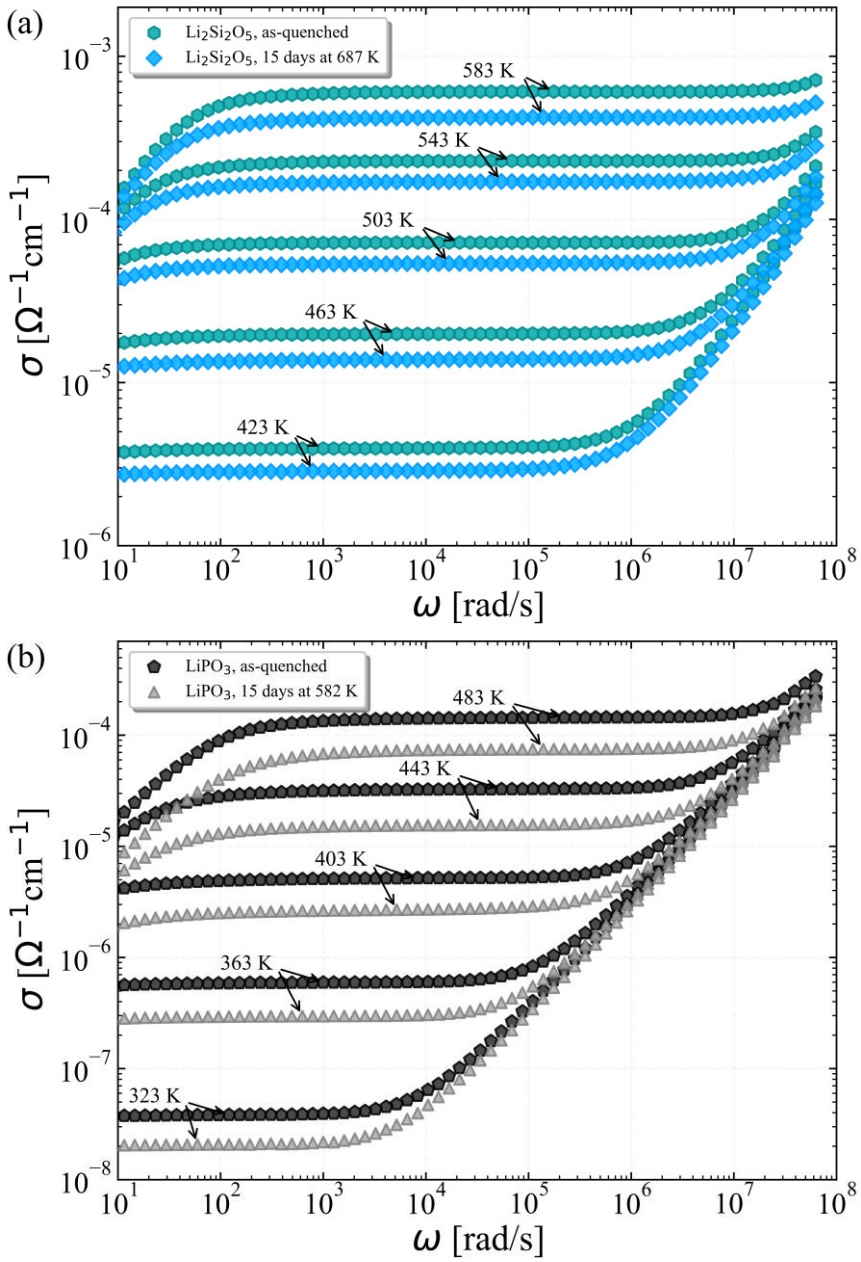

Figure 7.3: Frequency dependence of ionic conductivity for as-quenched and aged (a) $Li_2Si_2O_5$ and (b) $LiPO_3$ glasses at various temperatures.

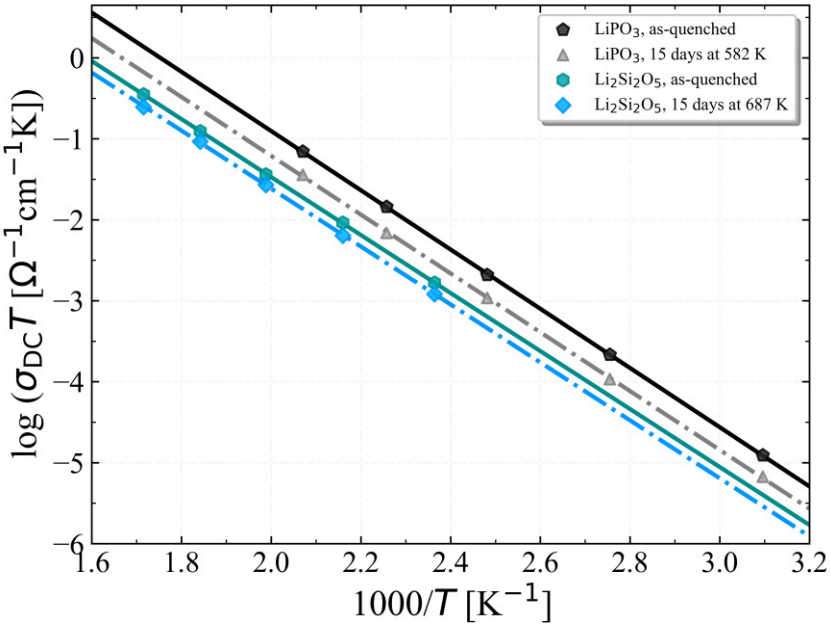

Figure 7.4: Reciprocal temperature dependence of DC conductivity for $Li_2Si_2O_5$ and $LiPO_3$ glasses. Solid and dash-dotted lines represent Arrhenius temperature dependence in the as-quenched and aged glasses, respectively.

It should be noted that the EIS experiments were conducted on both as-quenched and aged samples at temperatures well below T_g, where the possibility of further structural relaxation over the timescale of these measurements can be safely ignored. In contrast, **Figure 7.5**(a) displays the results of physical aging measured in-situ at 582 K for the $LiPO_3$ glass. **Figure 7.5**(b) shows the evolution of σ_{DC} from its initial equilibrium state to its final equilibrium state, demonstrating an agreement between the *ex situ* and *in situ* results. The initial and final data points, shown in darker color and indicated by arrows as "as-quenched" and "15 days at 582 K, *ex situ*", were obtained by extrapolating a fit of the data in **Figure 7.4** to 582 K using Eq. (7.2). It is crucial to capture the initial stage of structural relaxation, as significant changes occur immediately following the temperature jump. Many experiments, particularly *in situ* ones, may miss this early stage due to the time required for the sample temperature stabilization. Some authors [22,209–211] account for this by using a normalized time axis $(t - t_i)$, where t_i represents the thermal equilibration of the sample. As shown in **Figure 7.5**(b), up to 50% of the property changes can be missed within the first 15 min of aging, highlighting the importance of the initial stage of the α-relaxation phenomenon.

The time evolution of the DC ionic conductivity, $\sigma_{DC}(t)$, for $LiPO_3$ glass aged at 582 K was fitted with a KWW-type function (Eq. (2.7)). By fixing σ_0 to its initial measured value of 0.00230 $\Omega^{-1}cm^{-1}$, the following fitting parameters were obtained: $\sigma_\infty = (0.00115 \pm 0.00001)\ \Omega^{-1}cm^{-1}$, $\tau_K = (0.078 \pm 0.003)$ days, and $\beta = 0.251 \pm 0.003$.

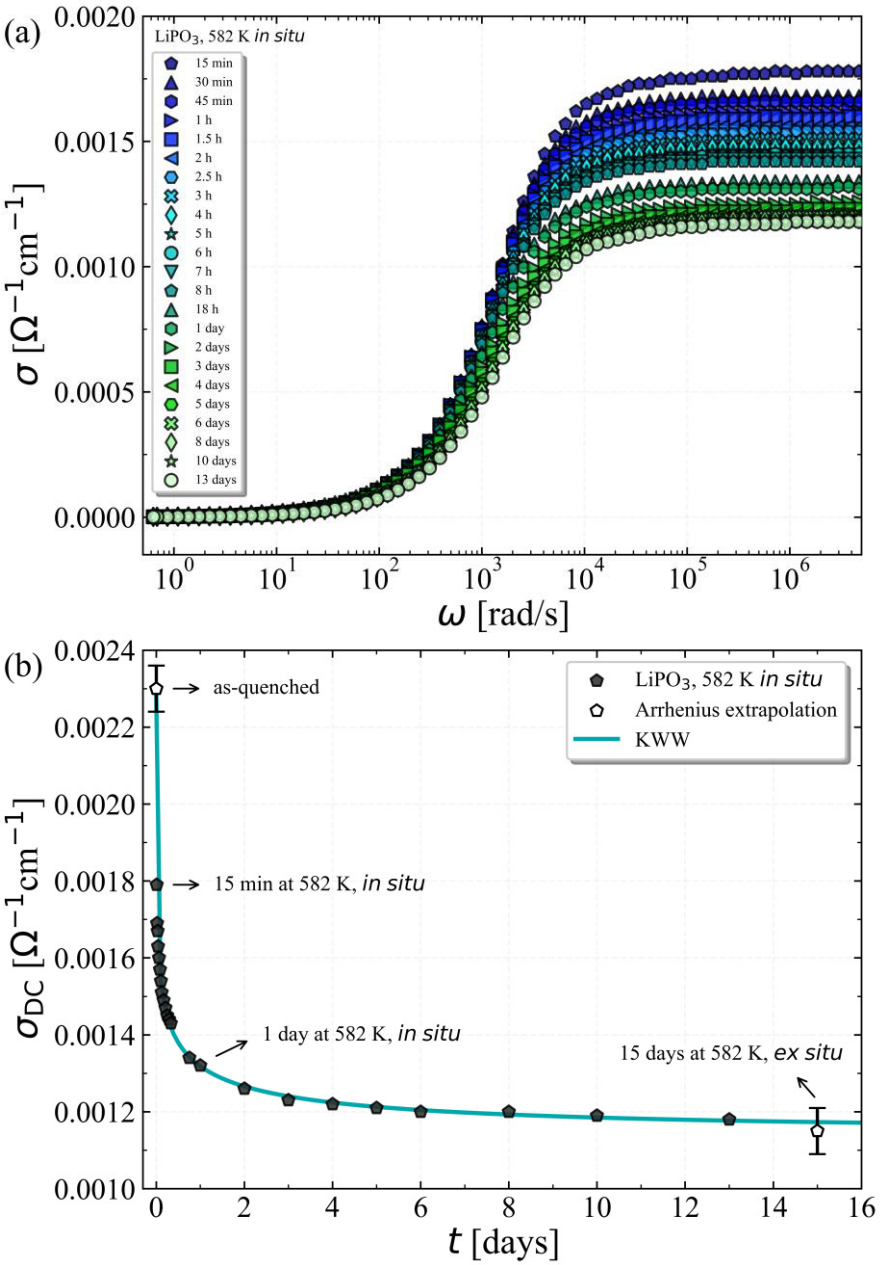

Figure 7.5: (a) Frequency dependence of ionic conductivity for $LiPO_3$ glass measured *in situ* during aging at 582 K for 13 days. (b) Temporal evolution of DC conductivity from (a), as it changes between the as-quenched sample and a sample aged *ex situ* for 15 days at 582 K. Solid line represents a fit to the data obtained using the KWW function, Eq. (2.7).

The migration enthalpy ΔH_m (activation energy E_a) for Li ion conduction was obtained by fitting the data in **Figure 7.4** using Eq. (7.2). While the activation energy of ionic conduction remains unchanged after aging for both $Li_2Si_2O_5$ and $LiPO_3$ glasses, the pre-exponential term A changes upon aging (**Table 7.2**), which is associated with the change in the entropy of migration ΔS_m. This relates to the difference in entropy contributions between the initial state and the saddle-point configuration during a local hopping process, where the entropy is considered vibrational in the initial state and translational at the saddle point [212].

The migration entropy ΔS_m may be numerically assessed since n can be obtained from the number of the modifier ion in the glass (using the chemical formula) divided by the molar volume, $\lambda = \sqrt[3]{1/n}$, and $\omega_0 = 1/\lambda\sqrt{2\Delta H_m/M}$, where M is the atomic mass of the mobile ions [213]. The values of n, λ, ω_0, and ΔS_m for the as-quenched and aged glasses are listed in **Table 7.2**.

Table 7.2: Migration enthalpy for ionic conduction ΔH_m, conductivity pre-exponential term A, charge carrier concentration n, hopping distance λ, attempt frequency ω_0, and migration entropy ΔS_m of as-quenched and aged glasses.

Sample	ΔH_m [kJ/mol]	log (A [Ω^{-1}cm^{-1}K])	$n \times 10^{-22}$ [cm^{-3}]	λ [Å]	$\omega_0 \times 10^{-13}$ [Hz]	ΔS_m [Jmol^{-1}K^{-1}]
$Li_2Si_2O_5$, as-quenched	68.5 ± 0.3	5.69 ± 0.03	1.873 ± 0.002	3.766 ± 0.001	1.180 ± 0.001	13.5 ± 0.1
$Li_2Si_2O_5$, 15 d 687 K	68.5 ± 0.5	5.54 ± 0.05	1.883 ± 0.002	3.759 ± 0.001	1.182 ± 0.001	10.6 ± 0.1
$LiPO_3$, as-quenched	70.0 ± 0.2	6.41 ± 0.03	1.642 ± 0.001	3.935 ± 0.001	1.141 ± 0.001	27.9 ± 0.2
$LiPO_3$, 15 d 582 K	69.5 ± 0.5	6.05 ± 0.07	1.647 ± 0.001	3.930 ± 0.001	1.143 ± 0.001	21.0 ± 0.3
$Na_{0.75}Mg_{0.125}PO_3$, as-quenched	69.4 ± 0.2	4.98 ± 0.03	1.148 ± 0.001	4.433 ± 0.001	0.555 ± 0.001	7.5 ± 0.1
$Na_{0.75}Mg_{0.125}PO_3$, 15 d 579 K	75.4 ± 0.5	5.09 ± 0.07	1.156 ± 0.001	4.423 ± 0.001	0.579 ± 0.001	9.2 ± 0.1

An analysis of Eq. (7.5) indicates that the decrease in the pre-exponential term A upon aging of $Li_2Si_2O_5$ and $LiPO_3$ glasses can be attributed to variations in the charge carrier concentration n, the hopping distance λ, the attempt frequency ω_0, or the entropy of migration ΔS_m. However, in these aged glasses, the increase in n due to a decrease in molar volume cannot explain the observed reduction in A. Similarly, the minor decrease in λ and negligible change in ω_0 are also insufficient to account for this change. Therefore, the primary factor responsible for the reduction in A is likely a decrease in ΔS_m in aged samples.

It should be noted that the hopping frequency of mobile Li ions ω_h is thermally activated and is described by the relation [214]:

$$\omega_h = \omega_0 \exp\left(\frac{\Delta S_m}{R}\right) \exp\left(-\frac{\Delta H_m}{RT}\right). \quad (7.7)$$

Given the negligible change in ω_0 and ΔH_m, a decrease in ΔS_m due to aging is expected to lead to a corresponding decrease in ω_h. This expectation is indeed confirmed by the $\sigma(\omega)$ data of the as-quenched and aged glasses (**Figure 7.6**(a)), which yield the hopping frequency ω_h when fitted to the Jonscher universal power-law relation [214,215]:

$$\sigma(\omega) = \sigma_{\mathrm{DC}} \left[1 + \left(\frac{\omega}{\omega_h}\right)^a\right], \quad (7.8)$$

where a is a material dependent constant. It is easy to see from this relation that ω equals ω_h in the frequency-dependent conductivity spectra when $\sigma(\omega)$ equals $2\sigma_{\mathrm{DC}}$. These fits yield ω_h in rad/s since the data is based on $\sigma(\omega)$, but the ω_h values shown in **Figure 7.6**(b) are in Hz and decrease after aging.

The role of migration entropy and hence, that of the hopping rate, in superionic conduction in solid electrolytes has only recently been emphasized in the literature [214]. The analysis of the aging-induced changes in the ionic conduction in $Li_2Si_2O_5$ and $LiPO_3$ glasses presented in this chapter clearly highlights the important role of migration entropy on ionic conduction.

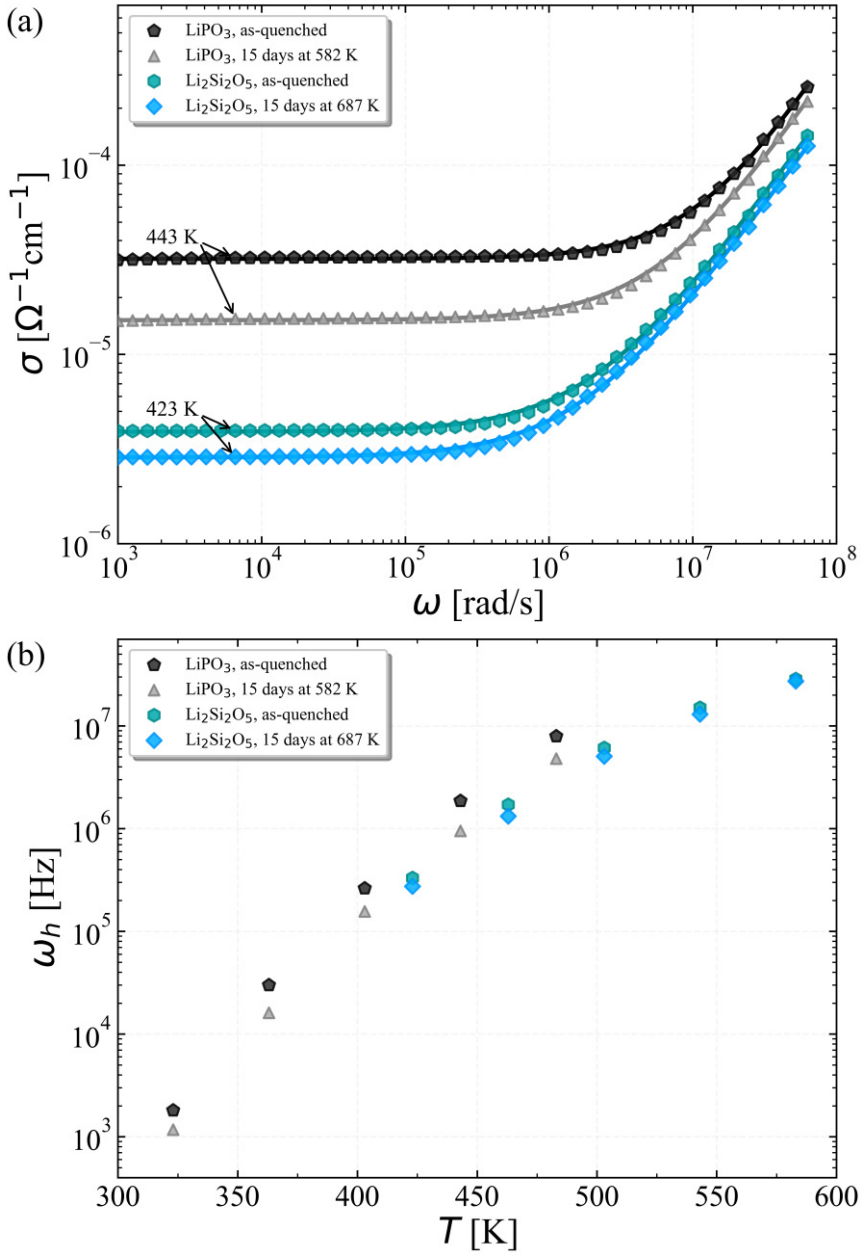

Figure 7.6: (a) Frequency dependence of ionic conductivity for as-quenched and aged $LiPO_3$ and $Li_2Si_2O_5$ glasses. Solid lines represent the fitting curves obtained using the Jonscher universal power-law relation via Eq. (7.8). (b) Variation of the hopping frequency with temperature for as-quenched and aged $LiPO_3$ and $Li_2Si_2O_5$ glasses.

The $\sigma(\omega)$ for the mixed-modifier $Na_{0.75}Mg_{0.125}PO_3$ glass is shown in **Figure 7.7**. The results indicate a decrease in conductivity after aging at T_g – 33 K = 579 K, with a significant reduction at 323 K, approaching almost one order of magnitude. This trend is similar to what was observed during the aging of the single-alkali $Li_2Si_2O_5$ and $LiPO_3$ glasses. The σ_{DC} of the as-quenched and aged mixed-modifier $Na_{0.75}Mg_{0.125}PO_3$ glass,

obtained directly from the frequency plateau as indicated by the arrows in **Figure 7.7**, are presented in **Figure 7.8**.

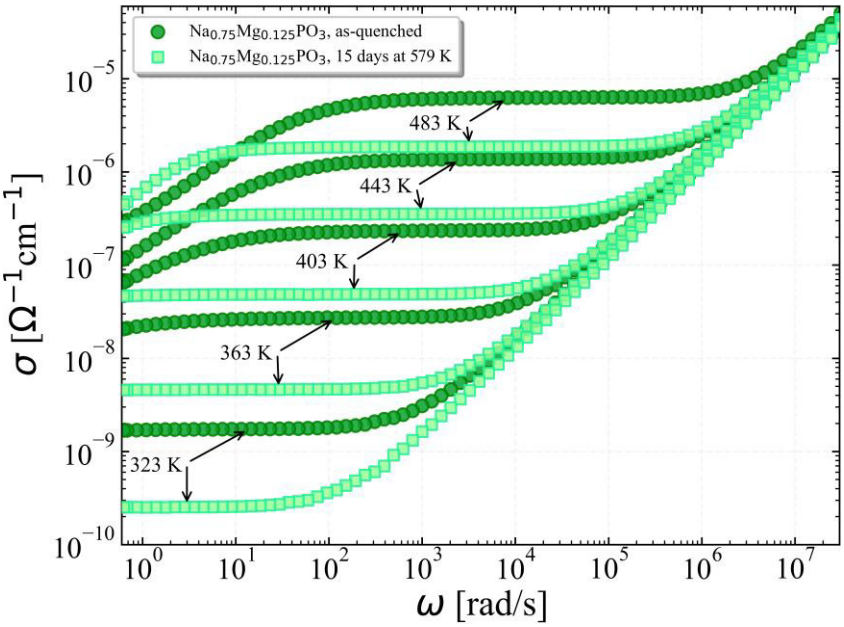

Figure 7.7: Frequency dependence of ionic conductivity for as-quenched and aged $Na_{0.75}Mg_{0.125}PO_3$ glass samples.

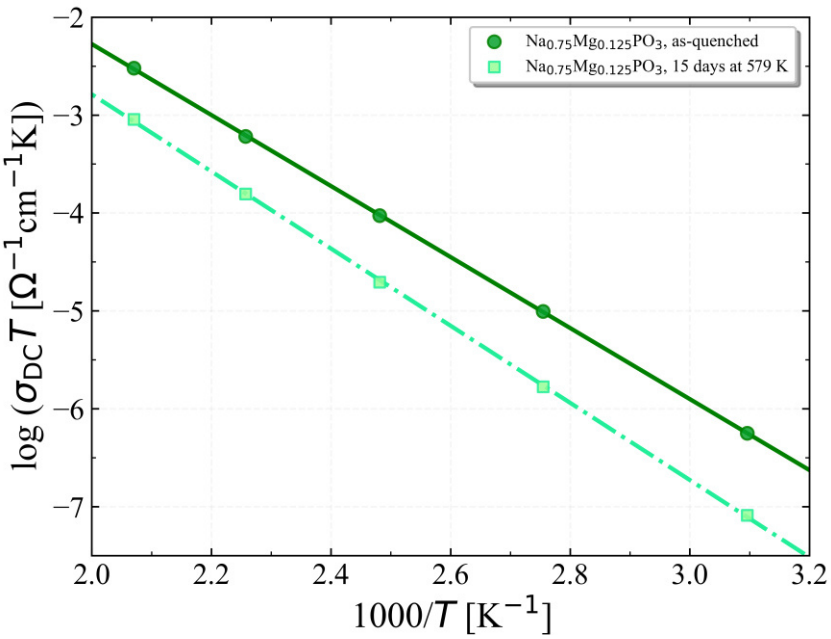

Figure 7.8: Reciprocal temperature dependence of DC conductivity for $Na_{0.75}Mg_{0.125}PO_3$ glass. Solid and dash-dotted lines represent Arrhenius temperature dependence in as-quenched and aged samples, respectively.

It may be noted that unlike the single-alkali glasses discussed above, this mixed-modifier $Na_{0.75}Mg_{0.125}PO_3$ glass exhibits an increase in both ΔH_m and the pre-exponential term A upon aging, leading to an increase in ΔS_m, as shown in **Table 7.2**. Variations in the pre-exponential term and migration enthalpy have been discussed in the literature on superionic argyrodites Li_6PS_5X (X = Cl, Br, I) [213], and $40\%Li_2S{-}60\%Ge(S,Se)_2$ sulfo-selenide glasses [216], suggesting that softening of the structural network leads to a decrease in ΔH_m and ΔS_m.

In this mixed-modifier glass, the ionic conductivity is expected to result from the hopping of the weakly bound, and thus mobile Na ions, while the strongly bound Mg ions would have significantly lower diffusivity. As a result, neighboring Mg ions would exert a blocking effect on the diffusion of Na, with the strength of this effect depending on the structural evolution of the network during aging. If Na and Mg become homogeneously distributed in the aged sample, Na ions would be more uniformly surrounded by Mg, leading to more efficient blocking of Na motion. This structural ordering of modifier cations may explain the significant decrease in conductivity and the concomitant increase in ΔH_m and ΔS_m (**Table 7.2**) observed in the aged mixed-modifier glass. In contrast, in the as-quenched glass with high fictive temperature (**Figure 7.2**), the Na-Mg distribution is expected to be more random, potentially allowing for the formation of Na-rich percolation pathways in the structure that facilitate Na motion.

7.4 Conclusions

The effect of α-relaxation on the ionic conductivity of single- and mixed-modifier glasses with different fragility indices was systematically investigated using temperature down-jump experiments. After physical aging, the density of the glass samples increased, while ionic conductivity decreased. The single-alkali glasses exhibited unchanged migration enthalpy and a reduction in the pre-exponential term A, primarily due to a decrease in migration entropy, which is related to reduced hopping frequency after structural densification. In contrast, the mixed-modifier glass showed increases in both migration enthalpy and entropy after aging, likely due to the structural ordering of the modifier Mg and Na ions, leading to more efficient blocking of Na motion.

CHAPTER 8 – GENERAL CONCLUSIONS

The spontaneous structural relaxation of glass towards the supercooled liquid state is an intrinsic characteristic of the glassy state. From the standpoint of technological importance, understanding structural relaxation and its effects on physical properties is key to designing new glass products or optimizing the performance of functional glasses.

Structural relaxation can be monitored isothermally through physical aging experiments or non-isothermal by heating or cooling a glass with different rates. Recently developed techniques such as Flash-DSC presented in Chapter 3 allow for very high quench and heating rates, extending the conventional range by about four orders of magnitude. This technique has proven effective in capturing changes in T_g of glasses with different thermal histories due to the relaxation phenomenon.

Despite extensive studies on structural relaxation during physical aging experiments, conflicting results have been reported on whether the kinetics of structural relaxation depends on the analyzed property. In Chapter 4, the time evolution of the refractive index and ionic conductivity following temperature down-jumps showed that relaxation dynamics depend on the analyzed property, with the relaxation process starting faster when probed by ionic conductivity than by refractive index.

A down-jump in fictive temperature is the predominant method employed to investigate structural relaxation, where the melt-quenched glass can be readily aged at a temperature below T_g, resulting in an increase in density. In contrast, conducting an up-jump experiment to decrease the density involves the time-consuming initial step of lowering T_f for several days or even weeks before initiating the actual up-jump procedure. In Chapter 5, physical aging experiments was conducted by changes in refractive index and enthalpy following up- and down-jumps in temperature. The KWW function exhibited a typical stretched exponential kinetic behavior with the non-exponentiality parameter $\beta < 1$ for temperature down-jumps, whereas up-jumps showed a compressed exponential behavior ($\beta > 1$). However, the non-exponential and non-linear TNM model described both up- and down-jump datasets using a single value of $\beta \leq 1$.

While the kinetics of relaxation can be obtained by measuring the temporal variation in a variety of physical properties during physical aging, the experimental determination of the atomic-scale structural rearrangements by which a glass relaxes has remained elusive. In Chapter 6, Raman and NMR spectroscopy were employed to

characterize the evolution of the structure during physical aging. The collective analysis of Raman and NMR spectra revealed that the aging-induced structural relaxation in the studied silicate glasses involves a disproportionation reaction, $Q^{n-1} + Q^{n+1} \rightleftharpoons 2Q^n$, shifting to the right with decreasing T_f.

Besides of the conventional single-alkali glasses used in all the other chapters, a mixed-modifier glass was used in Chapter 7 to study the impact of structural relaxation on the migration enthalpy ΔH_m and migration entropy ΔS_m of ionic conduction. In single-alkali Li disilicate and Li metaphosphate glasses, ΔH_m remains constant after aging, while ΔS_m decreases, leading to a corresponding reduction in the hopping rate of mobile alkali ions. In contrast, in the mixed-modifier Na-Mg metaphosphate glass, both ΔH_m and ΔS_m increase after aging. This behavior is potentially explained by a spatial redistribution of Na and Mg cations likely occurring alongside α-relaxation during aging. The results presented in that chapter demonstrate how the ionic conductivity of glasses can be tuned via their T_f. An increase in T_f of the mixed-modifier phosphate glass by approximately 36 K resulted in an increase in ionic conductivity by nearly an order of magnitude.

In conclusion, the implications of deeply understanding structural relaxation and its effects on physical properties are far-reaching. For example, fiberization can result in a cooling rate of nearly 10^6 K/s, which can easily increase the fictive temperature of the resulting glass by a few hundred degrees, and may result in rather large increase in its ionic conductivity. Thus, glass fibers or other fast-quenched products such as thin films may find novel applications in the areas such as sensors and solid electrolytes. These insights advance the understanding of the structural relaxation phenomena in glasses and their effects on macroscopic properties.

SUGGESTIONS FOR FUTURE WORKS

To study the structural relaxation process by enthalpy changes during temperature up-jumps using the Flash-DSC technique, avoiding missing any initial stages of the phenomenon.

To investigate the relaxation behavior as a function of the pressure release from a densified glass structure.

To evaluate the different existing models of structural relaxation to improve their predictive capabilities and accuracy.

To work on improving the ^{29}Si NMR signal-to-noise ratio for $PbSiO_3$ glass, which exhibits a wide variety of Q-species. This may be achieved through the use of higher magnetic fields and isotopic enrichment.

To study the structural origins of glass relaxation in other glass compositions, such as phosphate glasses formed by Q^1, Q^2, and Q^3 units using ^{31}P NMR.

To improve the ionic conductivity of high ion-conducting glasses by increasing their fictive temperature through producing glass fibers or thin films.

REFERENCES

[1] A. Cavagna, Supercooled liquids for pedestrians, Phys. Rep. 476 (2009) 51–124.

[2] A.Q. Tool, Relaxation of stresses in annealing glass, J. Res. Natl. Bur. Stand.(US). 34 (1945) 199–211.

[3] G.P. Johari, M. Goldstein, Viscous liquids and the glass transition. II. Secondary relaxations in glasses of rigid molecules, J. Chem. Phys. 53 (1970) 2372–2388.

[4] H.R. Lillie, Viscosity-time-temperature relations in glass at annealing temperatures, J. Am. Ceram. Soc. 16 (1933) 619–631.

[5] O.S. Narayanaswamy, A model of structural relaxation in glass, J. Am. Ceram. Soc. 54 (1971) 491–498.

[6] G.W. Scherer, Volume relaxation far from equilibrium, J. Am. Ceram. Soc. 69 (1986) 374–381.

[7] M. Micoulaut, Relaxation and physical aging in network glasses: a review, Reports Prog. Phys. 79 (2016) 66504.

[8] C.J. Wilkinson, K. Doss, O. Gulbiten, D.C. Allan, J.C. Mauro, Fragility and temperature dependence of stretched exponential relaxation in glass-forming systems, J. Am. Ceram. Soc. 104 (2021) 4559–4567.

[9] A. Winter, Transformation region of glass, J. Am. Ceram. Soc. 26 (1943) 189–200.

[10] A.Q. Tool, Relation between inelastic deformability and thermal expansion of glass in its annealing range, J. Am. Ceram. Soc. 29 (1946) 240–253.

[11] P.W. Collyer, Study of time and temperature effects on glass in annealing range, J. Am. Ceram. Soc. 30 (1947) 338–344.

[12] H.N. Ritland, Density phenomena in the transformation range of a borosilicate crown glass, J. Am. Ceram. Soc. 37 (1954) 370–377.

[13] S. Spinner, A. Napolitano, Further studies in the annealing of a borosilicate glass, United States Bur. Stand. J. Res. Chem. A. 70 (1966) 147–152.

[14] E.D. Zanotto, J.C. Mauro, The glassy state of matter: Its definition and ultimate fate, J. Non. Cryst. Solids. 471 (2017) 490–495.

[15] J. Zarzycki, Les verres et l'éclat vitreux, Masson, 1982.

[16] J. Shelby, Introduction to glass science and technology, 2nd ed., Royal Society of Chemistry, Cambridge, 2005.

[17] I. Gutzow, J.W.P. Schmelzer, The vitreous state, 2nd ed., Springer-Verlag, Berlin,

2013.

[18] A.K. Varshneya, J.C. Mauro, Fundamentals of inorganic glasses, 3nd ed., Elsevier, Sheffield, 2019.

[19] B. Abou, D. Bonn, J. Meunier, Aging dynamics in a colloidal glass, Phys. Rev. E. 64 (2001) 21510.

[20] L. Cipelletti, L. Ramos, Slow dynamics in glasses, gels and foams, Curr. Opin. Colloid Interface Sci. 7 (2002) 228–234.

[21] J.C. Phillips, Stretched exponential relaxation in molecular and electronic glasses, Reports Prog. Phys. 59 (1996) 1133.

[22] J. Málek, R. Svoboda, P. Pustková, P. Čičmanec, Volume and enthalpy relaxation of a-Se in the glass transition region, J. Non. Cryst. Solids. 355 (2009) 264–272.

[23] G.F. Rodriguez, G.G. Kenning, R. Orbach, Full aging in spin glasses, Phys. Rev. Lett. 91 (2003) 37203.

[24] L. Cipelletti, L. Ramos, Slow dynamics in glassy soft matter, J. Phys. Condens. Matter. 17 (2005) R253.

[25] D. Orsi, L. Cristofolini, G. Baldi, A. Madsen, Heterogeneous and anisotropic dynamics of a 2D gel, Phys. Rev. Lett. 108 (2012) 105701.

[26] W. Kauzmann, The nature of the glassy state and the behavior of liquids at low temperatures, Chem. Rev. 43 (1948) 219–256.

[27] W.H. Zachariasen, The atomic arrangement in glass, J. Am. Chem. Soc. 54 (1932) 3841–3851.

[28] G.N. Greaves, S. Sen, Inorganic glasses, glass-forming liquids and amorphizing solids, Adv. Phys. 56 (2007) 1–166.

[29] G.N. Greaves, EXAFS and the structure of glass, J. Non. Cryst. Solids. 71 (1985) 203–217.

[30] W.D. Kingery, H.K. Bowen, D.R. Uhlmann, Introduction to ceramics, 2nd ed., John Wiley & Sons, New York, 1976.

[31] G. Engelhardt, D. Zeigan, H. Jancke, D. Hoebbel, W. Wieker, Zur Abhangigkeit der Struktur der Silikatanionen in wassrigen Natrium Silikatlosungen vom Na: Si Verhaltnis, Zeit. Anorg. Allg. Chemie. 418 (1975) 17–28.

[32] D. V Sampaio, A. Picinin, B.J.A. Moulton, J.P. Rino, P.S. Pizani, E.D. Zanotto, Raman scattering and molecular dynamics investigation of lead metasilicate glass

and supercooled liquid structures, J. Non. Cryst. Solids. 499 (2018) 300–308.

[33] D.B. Dingwell, S.L. Webb, Relaxation in silicate melts, Eur. J. Mineral. (1990) 427–449.

[34] P.K. Gupta, J.C. Mauro, The laboratory glass transition, J. Chem. Phys. 126 (2007) 224504.

[35] G. Biroli, J.P. Garrahan, Perspective: The glass transition, J. Chem. Phys. 138 (2013) 12A301.

[36] M. Reiner, The Deborah number, Phys. Today. 17 (1964) 62.

[37] C.T. Moynihan, A.J. Easteal, J. Wilder, J. Tucker, Dependence of the glass transition temperature on heating and cooling rate, J. Phys. Chem. 78 (1974) 2673–2677.

[38] C.A. Angell, Formation of glasses from liquids and biopolymers, Science. 267 (1995) 1924–1935.

[39] N.P. Bansal, R.H. Doremus, Handbook of glass properties, Academic Press, New York, 1986.

[40] A.Q. Tool, C.G. Eichlin, Variations caused in the heating curves of glass by heat treatment, J. Am. Ceram. Soc. 14 (1931) 276–308.

[41] C.T. Moynihan, A.J. Easteal, M. DeBolt, J. Tucker, Dependence of the fictive temperature of glass on cooling rate, J. Am. Ceram. Soc. 59 (1976) 12–16.

[42] K.A. Kirchner, D.R. Cassar, E.D. Zanotto, M. Ono, S.H. Kim, K. Doss, M.L. Bødker, M.M. Smedskjaer, S. Kohara, L. Tang, M. Bauchy, C.J. Wilkinson, Y. Yang, R.S. Welch, M. Mancini, J.C. Mauro, Beyond the average: Spatial and temporal fluctuations in oxide glass-forming systems, Chem. Rev. 123 (2023) 1774–1840.

[43] J. Huang, P.K. Gupta, Enthalpy relaxation in thin glass fibers, J. Non. Cryst. Solids. 151 (1992) 175–181.

[44] Y.Z. Yue, J.C. Christiansen, S.L. Jensen, Determination of the fictive temperature for a hyperquenched glass, Chem. Phys. Lett. 357 (2002) 20–24.

[45] G.P. Johari, D.P.B. Aji, Time-dependent paths, fictive temperatures and residual entropy of glass, Philos. Mag. 90 (2010) 4377–4392.

[46] J.E.K. Schawe, K.-U. Hess, The kinetics of the glass transition of silicate glass measured by fast scanning calorimetry, Thermochim. Acta. 677 (2019) 85–90.

[47] J. Pries, S. Wei, F. Hoff, P. Lucas, M. Wuttig, Control of effective cooling rate upon magnetron sputter deposition of glassy $Ge_{15}Te_{85}$, Scr. Mater. 178 (2020) 223–226.

[48] H.N. Ritland, Limitations of the fictive temperature concept, J. Am. Ceram. Soc. 39 (1956) 403–406.

[49] J.C. Mauro, R.J. Loucks, P.K. Gupta, Fictive temperature and the glassy state, J. Am. Ceram. Soc. 92 (2009) 75–86.

[50] Y. Yue, Revealing the nature of glass by the hyperquenching-annealing-calorimetry approach, J. Non-Crystalline Solids X. 14 (2022) 100099.

[51] X. Guo, M. Potuzak, J.C. Mauro, D.C. Allan, T.J. Kiczenski, Y. Yue, Unified approach for determining the enthalpic fictive temperature of glasses with arbitrary thermal history, J. Non. Cryst. Solids. 357 (2011) 3230–3236.

[52] Y. Yue, R. Von der Ohe, S.L. Jensen, Fictive temperature, cooling rate, and viscosity of glasses, J. Chem. Phys. 120 (2004) 8053–8059.

[53] T. Yanagishima, J. Russo, H. Tanaka, Common mechanism of thermodynamic and mechanical origin for ageing and crystallization of glasses, Nat. Commun. 8 (2017) 15954.

[54] Y. Hamada, T. Murota, M. Shimizu, Y. Shimotsuma, K. Miura, Volume relaxation of soda-lime silicate glasses below glass transition temperature, AIP Adv. 13 (2023) 25353.

[55] L. Ding, K. Doss, Y. Yang, K. Lee, M. Bockowski, S. Demouchy, M. Thieme, B. Ziebarth, Q. Wang, M.M. Smedskjaer, Volume relaxation in a borosilicate glass hot compressed by three different methods, J. Am. Ceram. Soc. 104 (2021) 816–823.

[56] L. Ding, S. Buhre, C. Kunisch, B. Kaus, Pressure dependence of density and structural relaxation of glass near the glass transition region, J. Am. Ceram. Soc. 101 (2018) 1149–1158.

[57] V.M. Fokin, A.S. Abyzov, N.S. Yuritsyn, J.W.P. Schmelzer, E.D. Zanotto, Effect of structural relaxation on crystal nucleation in glasses, Acta Mater. 203 (2021) 116472.

[58] B. Yuan, H. Chen, S. Sen, Aging-induced structural evolution of a $GeSe_2$ glass network: The role of homopolar bonds, J. Phys. Chem. B. 126 (2022) 946–952.

[59] Y.P. Koh, S.L. Simon, Enthalpy recovery of polystyrene: Does a long-term aging plateau exist?, Macromolecules. 46 (2013) 5815–5821.

[60] D. Cangialosi, V.M. Boucher, A. Alegría, J. Colmenero, Direct evidence of two equilibration mechanisms in glassy polymers, Phys. Rev. Lett. 111 (2013) 95701.

[61] S.J. Schmidt, A.M. Lammert, Physical aging of maltose glasses, J. Food Sci. 61 (1996) 870–875.

[62] G.W. Scherer, Use of the Adam-Gibbs equation in the analysis of structural relaxation, J. Am. Ceram. Soc. 67 (1984) 504–511.

[63] U. Fotheringham, A. Baltes, P. Fischer, P. Höhn, R. Jedamzik, C. Schenk, C. Stolz, G. Westenberger, Refractive index drop observed after precision molding of optical elements: a quantitative understanding based on the Tool–Narayanaswamy–Moynihan model, J. Am. Ceram. Soc. 91 (2008) 780–783.

[64] R.F. Lancelotti, D.R. Cassar, M. Nalin, O. Peitl, E.D. Zanotto, Is the structural relaxation of glasses controlled by equilibrium shear viscosity?, J. Am. Ceram. Soc. 104 (2021) 2066–2076.

[65] M. Koide, R. Sato, T. Komatsu, K. Matusita, Viscosity and relaxation of glasses below the glass transition temperature, Thermochim. Acta. 280–281 (1996) 401–415.

[66] A. Sipp, D.R. Neuville, P. Richet, Viscosity, configurational entropy and relaxation kinetics of borosilicate melts, J. Non. Cryst. Solids. 211 (1997) 281–293.

[67] J.C. Mauro, D.C. Allan, M. Potuzak, Nonequilibrium viscosity of glass, Phys. Rev. B. 80 (2009) 94204.

[68] F.S. Howell, R.A. Bose, P.B. Macedo, C.T. Moynihan, Electrical relaxation in a glass-forming molten salt, J. Phys. Chem. 78 (1974) 639–648.

[69] C.B. Bragatto, D.R. Cassar, O. Peitl, J.-L. Souquet, A.C.M. Rodrigues, Structural relaxation in $AgPO_3$ glass followed by in situ ionic conductivity measurements, J. Non. Cryst. Solids. 437 (2016) 43–47.

[70] T. Friesen, J. Haupt, W. Gissler, A. Barna, P.B. Barna, Hardness, stress relaxation and microstructure of Ti–B–N multilayer coatings, Vacuum. 43 (1992) 657–659.

[71] Z. Zhang, J. Xie, Influence of relaxation and crystallization on micro-hardness and deformation of bulk metallic glass, Mater. Sci. Eng. A. 407 (2005) 161–166.

[72] F. Duan, J. Pan, Y. Lin, Y. Li, Significant structural relaxation in a Mo-O binary amorphous alloy, J. Non. Cryst. Solids. 514 (2019) 10–14.

[73] B. Ruta, G. Baldi, Y. Chushkin, B. Rufflé, L. Cristofolini, A. Fontana, M. Zanatta, F. Nazzani, Revealing the fast atomic motion of network glasses, Nat. Commun. 5 (2014) 3939.

[74] L. Berthier, M.D. Ediger, How to "measure" a structural relaxation time that is too long to be measured?, J. Chem. Phys. 153 (2020) 44501.

[75] E.D. Zanotto, P.K. Gupta, Do cathedral glasses flow?—Additional remarks, Am. J. Phys. 67 (1999) 260–262.

[76] O. Gulbiten, J.C. Mauro, X. Guo, O.N. Boratav, Viscous flow of medieval cathedral glass, J. Am. Ceram. Soc. 101 (2018) 5–11.

[77] P. Lucas, E.A. King, Y. Gueguen, J. Sangleboeuf, V. Keryvin, R.G. Erdmann, G. Delaizir, C. Boussard-Pledel, B. Bureau, X. Zhang, Correlation between thermal and mechanical relaxation in chalcogenide glass fibers, J. Am. Ceram. Soc. 92 (2009) 1986–1992.

[78] A.K. Varshneya, Chemical strengthening of glass: lessons learned and yet to be learned, Int. J. Appl. Glas. Sci. 1 (2010) 131–142.

[79] Q. Zheng, J.C. Mauro, Variability in the relaxation behavior of glass: Impact of thermal history fluctuations and fragility, J. Chem. Phys. 146 (2017).

[80] C. Wilkinson, Numerical and atomistic models for predicting structural relaxation in glasses, Comput. Mater. Sci. 234 (2024) 112744.

[81] K.L. Ngai, Correlation between the secondary β-relaxation time at T_g with the Kohlrausch exponent of the primary α relaxation or the fragility of glass-forming materials, Phys. Rev. E. 57 (1998) 7346.

[82] R. Richert, Heterogeneous dynamics in liquids: fluctuations in space and time, J. Phys. Condens. Matter. 14 (2002) R703.

[83] Z. Zhen, X. Ge, Z. Li, M.M. Smedskjaer, W. Lu, F. Yang, J. Li, Q. Hu, Low-temperature β-relaxation promotes crystallization in oxide glasses, Scr. Mater. 250 (2024) 116179.

[84] Q. Wang, S.T. Zhang, Y. Yang, Y.D. Dong, C.T. Liu, J. Lu, Unusual fast secondary relaxation in metallic glass, Nat. Commun. 6 (2015) 1–6.

[85] Z. Wang, W.-H. Wang, Flow units as dynamic defects in metallic glassy materials,

Natl. Sci. Rev. 6 (2019) 304–323.

[86] R. Kohlrausch, Theorie des elektrischen Rückstandes in der Leidener Flasche, Ann. Phys. 167 (1854) 179–214.

[87] F. Kohlrausch, Ueber die elastische Nachwirkung bei der Torsion, Ann. Phys. 195 (1863) 337–368.

[88] G. Williams, D.C. Watts, Non-symmetrical dielectric relaxation behaviour arising from a simple empirical decay function, Trans. Faraday Soc. 66 (1970) 80–85.

[89] M. Potuzak, R.C. Welch, J.C. Mauro, Topological origin of stretched exponential relaxation in glass, J. Chem. Phys. 135 (2011) 214502.

[90] P. Debye, Polar molecules, the chemical catalog company, Inc., New York. 89 (1929).

[91] J.C. Phillips, Kohlrausch explained: The solution to a problem that is 150 years old, J. Stat. Phys. 77 (1994) 945–947.

[92] K.L. Ngai, Relaxation and diffusion in complex systems, Springer Science+Business Media, New York, 2011.

[93] C.T. Moynihan, P.B. Macedo, C.J. Montrose, C.J. Montrose, P.K. Gupta, M.A. DeBolt, J.F. Dill, B.E. Dom, P.W. Drake, A.J. Easteal, Structural relaxation in vitreous materials, Ann. N. Y. Acad. Sci. 279 (1976) 15–35.

[94] I.M. Hodge, Physical aging in polymer glasses, Science. 267 (1995) 1945–1947.

[95] E.A. King, S. Sen, W. Takeda, C. Boussard-Pledel, B. Bureau, J.-P. Guin, P. Lucas, Extended aging of Ge–Se glasses below the glass transition temperature, J. Chem. Phys. 154 (2021) 164502.

[96] C.A. Angell, K.L. Ngai, G.B. McKenna, P.F. McMillan, S.W. Martin, Relaxation in glassforming liquids and amorphous solids, J. Appl. Phys. 88 (2000) 3113–3157.

[97] C.A. Angell, Relaxation in liquids, polymers and plastic crystals—strong/fragile patterns and problems, J. Non. Cryst. Solids. 131 (1991) 13–31.

[98] L.-M. Wang, V. Velikov, C.A. Angell, Direct determination of kinetic fragility indices of glassforming liquids by differential scanning calorimetry: Kinetic versus thermodynamic fragilities, J. Chem. Phys. 117 (2002) 10184–10192.

[99] Z. Chen, Z. Li, Y. Zhang, R. Liu, Y. Tian, L.-M. Wang, Calorimetric determination of fragility in glass forming liquids: T_f vs. T_g-onset methods, Eur. Phys. J. E. 37 (2014) 1–7.

[100] Q. Zheng, J.C. Mauro, Y. Yue, Reconciling calorimetric and kinetic fragilities of glass-forming liquids, J. Non. Cryst. Solids. 456 (2017) 95–100.

[101] V. Mathot, M. Pyda, T. Pijpers, G. Vanden Poel, E. Van de Kerkhof, S. Van Herwaarden, F. Van Herwaarden, A. Leenaers, The Flash DSC 1, a power compensation twin-type, chip-based fast scanning calorimeter (FSC): First findings on polymers, Thermochim. Acta. 522 (2011) 36–45.

[102] R. Al-Mukadam, D. Di Genova, H. Bornhöft, J. Deubener, High rate calorimetry derived viscosity of oxide melts prone to crystallization, J. Non. Cryst. Solids. 536 (2020) 119992.

[103] J. Deubener, Compositional onset of homogeneous nucleation in (Li, Na) disilicate glasses, J. Non. Cryst. Solids. 274 (2000) 195–201.

[104] K. Nakamura, Y. Takahashi, M. Osada, R. Ihara, T. Fujiwara, Effect of annealing at maximum nucleation temperature on boson peak in lithium-disilicate glass, J. Ceram. Soc. Japan. 120 (2012) 256–258.

[105] F.C. Serbena, I. Mathias, C.E. Foerster, E.D. Zanotto, Crystallization toughening of a model glass-ceramic, Acta Mater. 86 (2015) 216–228.

[106] J.C. Mauro, Y. Yue, A.J. Ellison, P.K. Gupta, D.C. Allan, Viscosity of glass-forming liquids, Proc. Natl. Acad. Sci. 106 (2009) 19780–19784.

[107] J. Gottsmann, D. Giordano, D.B. Dingwell, Predicting shear viscosity during volcanic processes at the glass transition: a calorimetric calibration, Earth Planet. Sci. Lett. 198 (2002) 417–427.

[108] J. Bockris, J.D. Mackenzie, J.A. Kitchener, Viscous flow in silica and binary liquid silicates, Trans. Faraday Soc. 51 (1955) 1734–1748.

[109] L. Sasek, Viscosity of silicate glass melts, Silikaty. 21 (1977) 291–306.

[110] A.H.M. Serra, Transient and stationary nucleation in vitreous lithium disilicate, Master dissertation, Federal University of São Carlos, 2018.

[111] Y. Ouchi, E. Kato, Effects of alkaline earth metal oxides, nickel oxide, and cobalt oxide on the viscosity of lead metasilicate melts, J. Japan Inst. Met. 43 (1979) 625–633.

[112] D.R. Cassar, R.F. Lancelotti, R. Nuernberg, M.L.F. Nascimento, A.M. Rodrigues, L.T. Diz, E.D. Zanotto, Elemental and cooperative diffusion in a liquid, supercooled liquid and glass resolved, J. Chem. Phys. 147 (2017) 14501.

[113] R. Al-Mukadam, I.K. Götz, M. Stolpe, J. Deubener, Viscosity of metallic glass-forming liquids based on Zr by fast-scanning calorimetry, Acta Mater. 221 (2021) 117370.

[114] A. Scarani, A. Vona, D. Di Genova, R. Al-Mukadam, C. Romano, J. Deubener, Determination of cooling rates of glasses over four orders of magnitude, Contrib. to Mineral. Petrol. 177 (2022) 35.

[115] J. Jiusti, E.D. Zanotto, D.R. Cassar, M.R.B. Andreeta, Viscosity and liquidus-based predictor of glass-forming ability of oxide glasses, J. Am. Ceram. Soc. 103 (2020) 921–932.

[116] P. Boivin, J.C. Berthelay, Y. Blanc, A. Coulet, R. Castanet, Determination of temperature and enthalpy of melting of alkali disilicates by differential calorimetric analysis, J. Mater. Sci. 28 (1993) 1834–1838.

[117] T.S. Neiman, H. Yinnon, D.R. Uhlmann, Crystallization kinetics of lead metasilicate, J. Non. Cryst. Solids. 48 (1982) 393–403.

[118] S. Kohara, H. Ohno, M. Takata, T. Usuki, H. Morita, K. Suzuya, J. Akola, L. Pusztai, Lead silicate glasses: Binary network-former glasses with large amounts of free volume, Phys. Rev. B. 82 (2010) 134209.

[119] S. Sen, R.F. Lancelotti, I. Hung, Z. Gan, Characterization of the Pb coordination environment and its connectivity in lead silicate glasses: Results from 2D ^{207}Pb NMR Spectroscopy, J. Phys. Chem. B. 128 (2024) 2811–2820.

[120] Y. Ding, L. Song, Z. Wang, R. Yu, J. Wang, L. Hu, Y. Yue, E.D. Zanotto, Unveiling the time-temperature dependence of metastability of supercooled liquid using nano-calorimetry, Sci. China Physics, Mech. Astron. 67 (2024) 236113.

[121] R. Ota, T. Wakasugi, W. Kawamura, B. Tuchiya, J. Fukunaga, Glass formation and crystallization in Li_2O-Na_2O-K_2O-SiO_2, J. Non. Cryst. Solids. 188 (1995) 136–146.

[122] E. Asayama, H. Takebe, K. Morinaga, Critical cooling rates for the formation of glass for silicate melts, ISIJ Int. 33 (1993) 233–238.

[123] M.A. DeBolt, A.J. Easteal, P.B. Macedo, C.T. Moynihan, Analysis of structural relaxation in glass using rate heating data, J. Am. Ceram. Soc. 59 (1976) 16–21.

[124] L. Boesch, A. Napolitano, P.B. Macedo, Spectrum of volume relaxation times in B_2O_3, J. Am. Ceram. Soc. 53 (1970) 148–153.

[125] H. Sasabe, C.T. Moynihan, Structural relaxation in poly(vinyl acetate), J. Polym. Sci. Polym. Phys. Ed. 16 (1978) 1447–1457.

[126] S.M. Rekhson, A. V Bulaeva, O. V Mazurin, Changes in the linear dimensions and viscosity of window glass during stabilization, Inorg. Mater. 7 (1971) 622–623.

[127] S.L. Webb, Shear, volume, enthalpy and structural relaxation in silicate melts, Chem. Geol. 96 (1992) 449–457.

[128] I. Echeverría, P.L. Kolek, D.J. Plazek, S.L. Simon, Enthalpy recovery, creep and creep–recovery measurements during physical aging of amorphous selenium, J. Non. Cryst. Solids. 324 (2003) 242–255.

[129] D.D. Macdonald, Reflections on the history of electrochemical impedance spectroscopy, Electrochim. Acta. 51 (2006) 1376–1388.

[130] L.R. Rodrigues, A.S. Abyzov, V.M. Fokin, E.D. Zanotto, Effect of structural relaxation on crystal nucleation in a soda-lime-silica glass, J. Am. Ceram. Soc. 104 (2021) 3212–3223.

[131] K.N. Kumar, M. Kostrzewa, A. Ingram, B. Suresh, A.S.S. Reddy, Y. Gandhi, M. Piasecki, N. Veeraiah, Dielectric features, relaxation dynamics and ac conductivity studies on Ag^{+} mixed lead arsenate glass ceramics, J. Mater. Sci. Mater. Electron. 29 (2018) 1153–1172.

[132] B.M. Hauke, M. Mancini, J.C. Mauro, Impact of a temperature-dependent stretching exponent on glass relaxation, Int. J. Appl. Glas. Sci. 13 (2022) 1–9.

[133] R.C. Welch, J.R. Smith, M. Potuzak, X. Guo, B.F. Bowden, T.J. Kiczenski, D.C. Allan, E.A. King, A.J. Ellison, J.C. Mauro, Dynamics of glass relaxation at room temperature, Phys. Rev. Lett. 110 (2013) 265901.

[134] M. Hara, S. Suetoshi, Density change of glass in transformation range, 1955.

[135] H. Bradtmüller, A. Gaddam, H. Eckert, E.D. Zanotto, Structural rearrangements during sub-T_g relaxation and nucleation in lithium disilicate glass revealed by a solid-state NMR and MD strategy, Acta Mater. 240 (2022) 118318.

[136] P. Falus, M.A. Borthwick, S. Narayanan, A.R. Sandy, S.G.J. Mochrie, Crossover from stretched to compressed exponential relaxations in a polymer-based sponge phase, Phys. Rev. Lett. 97 (2006) 66102.

[137] B. Ruta, Y. Chushkin, G. Monaco, L. Cipelletti, E. Pineda, P. Bruna, V.M. Giordano, M. Gonzalez-Silveira, Atomic-scale relaxation dynamics and aging in a

metallic glass probed by x-ray photon correlation spectroscopy, Phys. Rev. Lett. 109 (2012) 165701.

[138] E.W. Hansen, X. Gong, Q. Chen, Compressed exponential response function arising from a continuous distribution of Gaussian decays–distribution characteristics, Macromol. Chem. Phys. 214 (2013) 844–852.

[139] Z.W. Wu, W. Kob, W.-H. Wang, L. Xu, Stretched and compressed exponentials in the relaxation dynamics of a metallic glass-forming melt, Nat. Commun. 9 (2018) 5334.

[140] M. Guerette, M.R. Ackerson, J. Thomas, E.B. Watson, L. Huang, Thermally induced amorphous to amorphous transition in hot-compressed silica glass, J. Chem. Phys. 148 (2018) 194501.

[141] Q. Li, X. Peng, G.B. McKenna, Physical aging and compressed exponential behaviors in a model soft colloidal system, Soft Matter. 15 (2019) 2336–2347.

[142] D. Diaz Vela, D.S. Simmons, The microscopic origins of stretched exponential relaxation in two model glass-forming liquids as probed by simulations in the isoconfigurational ensemble, J. Chem. Phys. 153 (2020) 234503.

[143] K. Mithra, S.S. Jena, Surfactant head group and concentration influence on structure and dynamics of gellan gum hydrogels: Crossover from stretched to compressed exponential, J. Polym. Sci. 59 (2021) 1972–1985.

[144] K. Trachenko, A. Zaccone, Slow stretched-exponential and fast compressed-exponential relaxation from local event dynamics, J. Phys. Condens. Matter. 33 (2021) 315101.

[145] T.D. Jaeger, D.S. Simmons, Temperature dependence of aging dynamics in highly non-equilibrium model polymer glasses, J. Chem. Phys. 156 (2022) 114504.

[146] D. Cangialosi, V.M. Boucher, A. Alegría, J. Colmenero, Physical aging in polymers and polymer nanocomposites: recent results and open questions, Soft Matter. 9 (2013) 8619–8630.

[147] G.B. McKenna, C.A. Angell, The phenomenology and models of the kinetics of volume and enthalpy in the glass transition range, J. Non. Cryst. Solids. 131–133 (1991) 528–536.

[148] R. Svoboda, J. Málek, Description of enthalpy relaxation dynamics in terms of TNM model, J. Non. Cryst. Solids. 378 (2013) 186–195.

[149] V. Di Lisio, V.-M. Stavropoulou, D. Cangialosi, Physical aging in molecular glasses beyond the α relaxation, J. Chem. Phys. 159 (2023) 064505.

[150] A. Toda, Isothermal enthalpy relaxation of amorphous polystyrene studied using Temperature-Modulated Fast Scanning Calorimetry, Thermochim. Acta. 721 (2023) 179433.

[151] R.F. Lancelotti, T.R. da Cunha, M.A.C. Kurtovic, P.S. Pizani, S. Sen, E.D. Zanotto, Physical aging of lithium disilicate glass, J. Non. Cryst. Solids. 622 (2023) 122661.

[152] I.M. Hodge, A.R. Berens, Effects of annealing and prior history on enthalpy relaxation in glassy polymers. 2. Mathematical modeling, Macromolecules. 15 (1982) 762–770.

[153] C.T. Moynihan, S.-K. Lee, M. Tatsumisago, T. Minami, Estimation of activation energies for structural relaxation and viscous flow from DTA and DSC experiments, Thermochim. Acta. 280–281 (1996) 153–162.

[154] P. Pan, B. Zhu, Y. Inoue, Enthalpy relaxation and embrittlement of poly(L-lactide) during physical aging, Macromolecules. 40 (2007) 9664–9671.

[155] C. Herrero, C. Scalliet, M.D. Ediger, L. Berthier, Two-step devitrification of ultrastable glasses, Proc. Natl. Acad. Sci. 120 (2023) e2220824120.

[156] K.L. Kearns, M.D. Ediger, H. Huth, C. Schick, One micrometer length scale controls kinetic stability of low-energy glasses, J. Phys. Chem. Lett. 1 (2010) 388–392.

[157] A. Vila-Costa, J. Ràfols-Ribé, M. González-Silveira, A.F. Lopeandia, L. Abad-Muñoz, J. Rodríguez-Viejo, Nucleation and growth of the supercooled liquid phase control glass transition in bulk ultrastable glasses, Phys. Rev. Lett. 124 (2020) 76002.

[158] A. Vila-Costa, M. Gonzalez-Silveira, C. Rodríguez-Tinoco, M. Rodríguez-López, J. Rodriguez-Viejo, Emergence of equilibrated liquid regions within the glass, Nat. Phys. 19 (2023) 114–119.

[159] J. William, R. Mehl, Reaction kinetics in processes of nucleation and growth, Trans. Am. Inst. Min. Metall. Eng. 135 (1939) 416–442.

[160] M. Avrami, Kinetics of phase change. I General theory, J. Chem. Phys. 7 (1939) 1103–1112.

[161] J.M. O'Reilly, Review of structure and mobility in amorphous polymers, Crit. Rev. Solid State Mater. Sci. 13 (1987) 259–277.

[162] M.E. Brandriss, J.F. Stebbins, Effects of temperature on the structures of silicate liquids: ^{29}Si NMR results, Geochim. Cosmochim. Acta. 52 (1988) 2659–2669.

[163] X. Li, W. Song, K. Yang, N.M.A. Krishnan, B. Wang, M.M. Smedskjaer, J.C. Mauro, G. Sant, M. Balonis, M. Bauchy, Cooling rate effects in sodium silicate glasses: Bridging the gap between molecular dynamics simulations and experiments, J. Chem. Phys. 147 (2017) 74501.

[164] W. Song, X. Li, B. Wang, N.M. Anoop Krishnan, S. Goyal, M.M. Smedskjaer, J.C. Mauro, C.G. Hoover, M. Bauchy, Atomic picture of structural relaxation in silicate glasses, Appl. Phys. Lett. 114 (2019) 233703.

[165] J.F. Stebbins, S.E. Ellsworth, Temperature effects on structure and dynamics in borate and borosilicate liquids: high-resolution and high-temperature NMR results, J. Am. Ceram. Soc. 79 (1996) 2247–2256.

[166] S. Sen, Z. Xu, J.F. Stebbins, Temperature dependent structural changes in borate, borosilicate and boroaluminate liquids: high-resolution ^{11}B, ^{29}Si and ^{27}Al NMR studies, J. Non. Cryst. Solids. 226 (1998) 29–40.

[167] S. Sen, Temperature induced structural changes and transport mechanisms in borate, borosilicate and boroaluminate liquids: high-resolution and high-temperature NMR results, J. Non. Cryst. Solids. 253 (1999) 84–94.

[168] S. Sen, T. Topping, P. Yu, R.E. Youngman, Atomic-scale understanding of structural relaxation in simple and complex borosilicate glasses, Phys. Rev. B. 75 (2007) 94203.

[169] S.S. Uzun, S. Sen, ^{11}B MAS NMR spectroscopic study of structural relaxation, aging, and memory effect at the atomic scale in a borosilicate glass, J. Phys. Chem. B. 111 (2007) 9758–9761.

[170] T.G. Edwards, S. Sen, Structure and relaxation in germanium selenide glasses and supercooled liquids: a Raman spectroscopic study, J. Phys. Chem. B. 115 (2011) 4307–4314.

[171] S. Jurca, H. Chen, S. Sen, Structural, shear and volume relaxation in a commercial float glass during aging, J. Non. Cryst. Solids. 589 (2022) 121650.

[172] V.M. Fokin, A.M. Kalinina, V.N. Filipovich, Nucleation in silicate glasses and

effect of preliminary heat treatment on it, J. Cryst. Growth. 52 (1981) 115–121.

[173] M. Wojdyr, Fityk: a general-purpose peak fitting program, J. Appl. Crystallogr. 43 (2010) 1126–1128.

[174] D. Massiot, F. Fayon, M. Capron, I. King, S. Le Calvé, B. Alonso, J. Durand, B. Bujoli, Z. Gan, G. Hoatson, Modelling one-and two-dimensional solid-state NMR spectra, Magn. Reson. Chem. 40 (2002) 70–76.

[175] P. Claudy, S. Jabrane, J.M. Létoffé, Annealing of a glycerol glass: Enthalpy, fictive temperature and glass transition temperature change with annealing parameters, Thermochim. Acta. 293 (1997) 1–11.

[176] S.L. Simon, J.-Y. Park, G.B. McKenna, Enthalpy recovery of a glass-forming liquid constrained in a nanoporous matrix: Negative pressure effects, Eur. Phys. J. E. 8 (2002) 209–216.

[177] D.W. Matson, S.K. Sharma, J.A. Philpotts, The structure of high-silica alkali-silicate glasses. A Raman spectroscopic investigation, J. Non. Cryst. Solids. 58 (1983) 323–352.

[178] P.F. McMillan, G.H. Wolf, B.T. Poe, Vibrational spectroscopy of silicate liquids and glasses, Chem. Geol. 96 (1992) 351–366.

[179] B.O. Mysen, D. Virgo, F.A. Seifert, The structure of silicate melts: implications for chemical and physical properties of natural magma, Rev. Geophys. 20 (1982) 353–383.

[180] B.O. Mysen, J.D. Frantz, Silicate melts at magmatic temperatures: in-situ structure determination to 1651 °C and effect of temperature and bulk composition on the mixing behavior of structural units, Contrib. to Mineral. Petrol. 117 (1994) 1–14.

[181] T. Maehara, T. Yano, S. Shibata, M. Yamane, Structure and phase transformation of alkali silicate melts analysed by Raman spectroscopy, Philos. Mag. 84 (2004) 3085–3099.

[182] D.R. Neuville, Viscosity, structure and mixing in (Ca, Na) silicate melts, Chem. Geol. 229 (2006) 28–41.

[183] C. O'Shaughnessy, G.S. Henderson, H.W. Nesbitt, G.M. Bancroft, D.R. Neuville, The influence of modifier cations on the Raman stretching modes of Qn species in alkali silicate glasses, J. Am. Ceram. Soc. 103 (2020) 3991–4001.

[184] C. Calahoo, J.W. Zwanziger, I.S. Butler, Mechanical–structural investigation of

ion-exchanged lithium silicate glass using micro-Raman spectroscopy, J. Phys. Chem. C. 120 (2016) 7213–7232.

[185] B.G. Parkinson, D. Holland, M.E. Smith, C. Larson, J. Doerr, M. Affatigato, S.A. Feller, A.P. Howes, C.R. Scales, Quantitative measurement of Q^3 species in silicate and borosilicate glasses using Raman spectroscopy, J. Non. Cryst. Solids. 354 (2008) 1936–1942.

[186] O.N. Koroleva, The structure of lithium silicate melts revealed by high-temperature Raman spectroscopy, Spectrosc. Lett. 50 (2017) 257–264.

[187] H. Maekawa, T. Maekawa, K. Kawamura, T. Yokokawa, The structural groups of alkali silicate glasses determined from ^{29}Si MAS-NMR, J. Non. Cryst. Solids. 127 (1991) 53–64.

[188] Y. Iqbal, W.E. Lee, D. Holland, P.F. James, Metastable phase formation in the early stage crystallisation of lithium disilicate glass, J. Non. Cryst. Solids. 224 (1998) 1–16.

[189] S. Buchner, A.S. Pereira, J.C. de Lima, N.M. Balzaretti, Effect of annealing close to T_g on the short-range order of lithium disilicate glass, J. Non. Cryst. Solids. 560 (2021) 120729.

[190] E.D. Zanotto, J.E. Tsuchida, J.F. Schneider, H. Eckert, Thirty-year quest for structure–nucleation relationships in oxide glasses, Int. Mater. Rev. 60 (2015) 376–391.

[191] F. Fayon, C. Bessada, D. Massiot, I. Farnan, J.P. Coutures, ^{29}Si and ^{207}Pb NMR study of local order in lead silicate glasses, J. Non. Cryst. Solids. 232 (1998) 403–408.

[192] I. Ben Kacem, L. Gautron, D. Coillot, D.R. Neuville, Structure and properties of lead silicate glasses and melts, Chem. Geol. 461 (2017) 104–114.

[193] C.A. Worrell, T. Henshall, Vibrational spectroscopic studies of some lead silicate glasses, J. Non. Cryst. Solids. 29 (1978) 283–299.

[194] R.B. Pena, D. V Sampaio, R.F. Lancelotti, T.R. Cunha, E.D. Zanotto, P.S. Pizani, In-situ Raman spectroscopy unveils metastable crystallization in lead metasilicate glass, J. Non. Cryst. Solids. 546 (2020) 120254.

[195] R.B. Pena, V. Laurent, T. Deschamps, E. Romeo, A. Picinin, C. Martinet, P.S. Pizani, High-pressure plastic deformation of lead metasilicate glass accessed by

Raman spectroscopy: Insights into the Qn distribution, J. Non. Cryst. Solids. 567 (2021) 120930.

[196] S. Feller, G. Lodden, A. Riley, T. Edwards, J. Croskrey, A. Schue, D. Liss, D. Stentz, S. Blair, M. Kelley, A multispectroscopic structural study of lead silicate glasses over an extended range of compositions, J. Non. Cryst. Solids. 356 (2010) 304–313.

[197] F. Liebau, Untersuchungen an schichtsilikaten des formeltyps $A_m(Si_2O_5)_n$. I. Die kristallstruktur der zimmertemperaturform des $Li_2Si_2O_5$, Acta Crystallogr. 14 (1961) 389–395.

[198] C.M. Schramm, B. De Jong, V.E. Parziale, ^{29}Si Magic Angle Spinning NMR study on local silicon environments in amorphous and crystalline lithium silicates, J. Am. Chem. Soc. 106 (1984) 4396–4402.

[199] M.L. Boucher, D.R. Peacor, The crystal structure of alamosite, $PbSiO_3$, Zeitschrift Für Krist. Mater. 126 (1968) 98–111.

[200] C. Bessada, D. Massiot, J. Coutures, A. Douy, J.-P. Coutures, F. Taulelle, ^{29}Si MAS-NMR in lead silicates, J. Non. Cryst. Solids. 168 (1994) 76–85.

[201] T. Suzuki, Y. Hamada, M. Shimizu, S. Urata, Y. Shimotsuma, K. Miura, Atomistic mechanism of structural and volume relaxation below glass transition temperature in a soda-lime silicate glass revealed by Raman spectroscopy and its DFT calculations, J. Chem. Phys. 160 (2024).

[202] T. Yeo, B. Yuan, J. Lovi, J.-W. Cho, S. Sen, Resolving the mixed-alkali effect on the viscoelastic behavior of supercooled liquids, Acta Mater. 242 (2023) 118447.

[203] K.J. Rao, Structural chemistry of glasses, Elsevier Science & Technology Books, Amsterdam, The Netherlands, 2002.

[204] R.B. Nuernberg, Numerical comparison of usual Arrhenius-type equations for modeling ionic transport in solids, Ionics (Kiel). 26 (2020) 2405–2412.

[205] J.B. Goodenough, Fast ionic conduction in solid, Proc. R. Soc. London. A. Math. Phys. Sci. 393 (1984) 215–234.

[206] D.P. Almond, A.R. West, The activation entropy for transport in ionic conductors, Solid State Ionics. 23 (1987) 27–35.

[207] J.-L. Souquet, M.L.F. Nascimento, A.C.M. Rodrigues, Charge carrier concentration and mobility in alkali silicates, J. Chem. Phys. 132 (2010).

[208] J. Pries, C. Stenz, S. Wei, M. Wuttig, P. Lucas, Structural relaxation of amorphous phase change materials at room temperature, J. Appl. Phys. 135 (2024) 135101.

[209] J. Málek, Structural relaxation rate and aging in amorphous solids, J. Phys. Chem. C. 127 (2023) 6080–6087.

[210] S. Jin, G.B. McKenna, Anomalous structural recovery in the near glass transition range in a polymer glass: Data revisited in light of temperature variability in vacuum oven-based experiments, Polym. Eng. Sci. 62 (2022) 1124–1136.

[211] D. Cangialosi, A. Alegría, J. Colmenero, Comment on "Anomalous structural recovery in the near glass transition range in a polymer glass: Data revisited in light of temperature variability in vacuum oven-based experiments," Polym. Eng. Sci. 62 (2022) 2716–2721.

[212] T.W. Dobson, J.F. Wager, J.A. Van Vechten, Entropy of migration for atomic hopping, Phys. Rev. B. 40 (1989) 2962.

[213] M.A. Kraft, S.P. Culver, M. Calderon, F. Böcher, T. Krauskopf, A. Senyshyn, C. Dietrich, A. Zevalkink, J. Janek, W.G. Zeier, Influence of lattice polarizability on the ionic conductivity in the lithium superionic argyrodites Li_6PS_5X (X= Cl, Br, I), J. Am. Chem. Soc. 139 (2017) 10909–10918.

[214] X. Li, H. Liu, C. Zhao, J.T. Kim, J. Fu, X. Hao, W. Li, R. Li, N. Chen, D. Cao, Hopping rate and migration entropy as the origin of superionic conduction within solid-state electrolytes, J. Am. Chem. Soc. 145 (2023) 11701–11709.

[215] A.K. Jonscher, Dielectric relaxation in solids, J. Phys. D. Appl. Phys. 32 (1999) R57.

[216] M.A.T. Marple, B.G. Aitken, S. Kim, S. Sen, Observation of a phonon softening effect on Li ion conduction in mixed-anion chalcogenide glasses, Chem. Mater. 30 (2018) 5896–5903.